UNIVERSITY OF OKLAHOMA

GRADUATE COLLEGE

EQUILIBRIUM AND TRANSPORT PROPERTIES OF SYSTEMS CONTAINING GRAPHENE SHEETS (-OIL NANOCOMPOSITES AND MEMBRANES) FROM MOLECULAR DYNAMICS SIMULATIONS

A DISSERTATION

SUBMITTED TO THE GRADUATE FACULTY

in partial fulfillment of the requirements for the

Degree of

DOCTOR OF PHILOSOPHY

By

DEEPTHI KONATHAM
Norman, Oklahoma
2014

EQUILIBRIUM AND TRANSPORT PROPERTIES OF SYSTEMS CONTAINING GRAPHENE SHEETS (-OIL NANOCOMPOSITES AND MEMBRANES) FROM MOLECULAR DYNAMICS SIMULATIONS

A DISSERTATION APPROVED FOR THE
SCHOOL OF CHEMICAL, BIOLOGICAL AND MATERIALS ENGINEERING

BY

_____
Dr. Brian P. Grady, Chair

_____
Dr. Alberto Striolo, Co-chair

_____
Dr. Kieran Mullen

_____
Dr. Dimitrios V. Papavassiliou

_____
Dr. Liangliang Huang

_____
Dr. Takumi Hawa

To my parents

Rukmini Konatham and Janardhan Reddy Konatham

Acknowledgements

The completion of this work would have not been possible without the generous allocations of computing time provided by the OU Supercomputing Center for Education and Research (OSCER) in Norman, Oklahoma and the National Energy Research Scientific Computing Center (NERSC) in Berkeley, California.

This research work would not have been feasible without the financial support provided by Petroleum Research Fund (administered by the American Chemical Society), by the DuPont Corporation, by the U.S. Department of Energy (DOE)-funded Center for Applications of Single-Walled Nanotubes, by Department of Defense (DOD)-EPSCOR, and by DOE.

Table of Contents

List of Tables

List of Figures

Abstract

Graphene sheets belong to an interesting class of materials. Their exceptional properties, including high thermal and electrical conductivity, mechanical strength etc., could play an important role in multiple applications, suggesting the possible use of graphene sheets in, e.g., electronic devices, nanocomposites, energy storage, and membranes for water desalination, to name just a few. Understanding the properties of graphene is essential to secure progress in all these areas. Molecular dynamics simulations were performed to provide molecular level insights of the equilibrium and transport properties of several systems containing graphene sheets.

In the first part of the thesis graphene-oil nanocomposites are considered. Results show that it is possible to obtain stable dispersions of graphene sheets in oils such as n-hexane, n-octane and n-dodecane by appropriately functionalizing the edges of the graphene sheets with short branched alkanes. Excluded-volume effects, generated by the branched architecture of the functional groups grafted on the graphene sheets, are responsible for the stabilization of small graphene sheets in the organic systems considered here. Using non-equilibrium molecular dynamics, the Kapitza resistance at the graphene-octane and graphene-graphene interfaces was calculated. Our results demonstrate that it is possible to reduce the Kapitza resistance at the graphene sheet-octane interface by using the functionalized graphene sheets, but the functional groups must show vibrational modes compatible with those of the organic matrix. A higher value of Kapitza resistance for graphene sheets in vacuum compared to that in octane was found because the graphene-graphene interface has larger Kapitza resistance than

the graphene-octane interface, which is consistent with observations for carbon nanotube – carbon nanotube contacts. More importantly, the Kapitza resistance for the graphene-graphene contact can be 30% lower than values reported for the carbon nanotube – carbon nanotube contact. Equilibrium and non-equilibrium molecular dynamics simulations to assess the effective interactions between dispersed graphene sheets, the self-assembly of graphene, and the heat transfer through the graphene-octane nanocomposite. Evidence is provided for the formation of nematic phases when the graphene sheets volume fraction increases within octane. The atomic-level results are input for a coarse-grained Monte Carlo simulation that predicts anisotropic thermal conductivity for graphene-based composites when the graphene sheets show nematic phases. Overall, these results suggest that it might be possible to produce nanocomposites containing graphene sheets. Such materials could show exceptional mechanical and thermal-transport properties (due to the inclusion of graphene sheets), while maintaining the lightweight typical of polymeric materials.

In the second part of the thesis umbrella sampling simulations were employed to study the transport of water molecules and ions through the membranes incorporating bare and functionalized graphene pores. By calculating the potential of mean force for ion and water translocation through the bare graphene pores, we show that ions face a large energy barrier and will not pass through the narrower pore studied (Ø ~ 7.5 Å) but can pass through the wider pores (Ø ~ 10.5 and 14.5). Water, however, faces no such impediment and passes through all the pores studied with little energy barrier. When charged groups are grafted to the pore rim, the results show that the charges can help to

prevent the passage of ions. Comparison of results for graphene pore to that of carbon nanotube pore reveals that COO^- groups are more effective when grafted to the rim of GS pore in preventing Cl^- ions from passing through the membrane compared to that of carbon nanotube pore. The results presented could be useful for the design of water desalination membranes.

1. Introduction

Most part of the material presented below is taken directly from the journal articles that I co-authored.

Graphene is an allotrope of carbon comprised of one atom thick layer of sp^2 bonded carbon atoms.[1-5] arranged in a regular hexagonal pattern.[5] The carbon-carbon bond length in graphene is about 1.42 Å.[6] Graphene forms the basic building block of various carbon allotropes including graphite, charcoal, carbon nanotubes and fullerenes as shown in Figure 1-1. Graphene sheets (GS) stack to form graphite with an interlayer spacing of 3.35 Å. In this introductory chapter I summarize briefly the discovery, production, properties, and possible applications of graphene. I then summarize some of the current limitations that hinder the deployment of such applications. Particular attention is given to those limitations that are addressed with our research (i.e., stabilization of GS in organic oils, thermal boundary resistance at the GS-octane and GS-GS interfaces, thermal conductivity of GS-oil nanocomposites, and possible use of GS as desalination membranes).

Graphene was discovered in 2004 by physicists at the University of Manchester and the Institute for Microelectronics Technology, Chernogolovka, Russia.[1] In this discovery, Novoselov et al.[1] isolated individual graphene planes from graphite by using adhesive tape. They then transferred these individual GS onto silicon wafer. This process is called the Scotch tape technique. Being able to isolate individual GS allowed many

scientists to measure the properties of the GS, which led to an explosion of interest in graphene, and granted Geim and Novoselov the Nobel Prize in Physics in 2010.

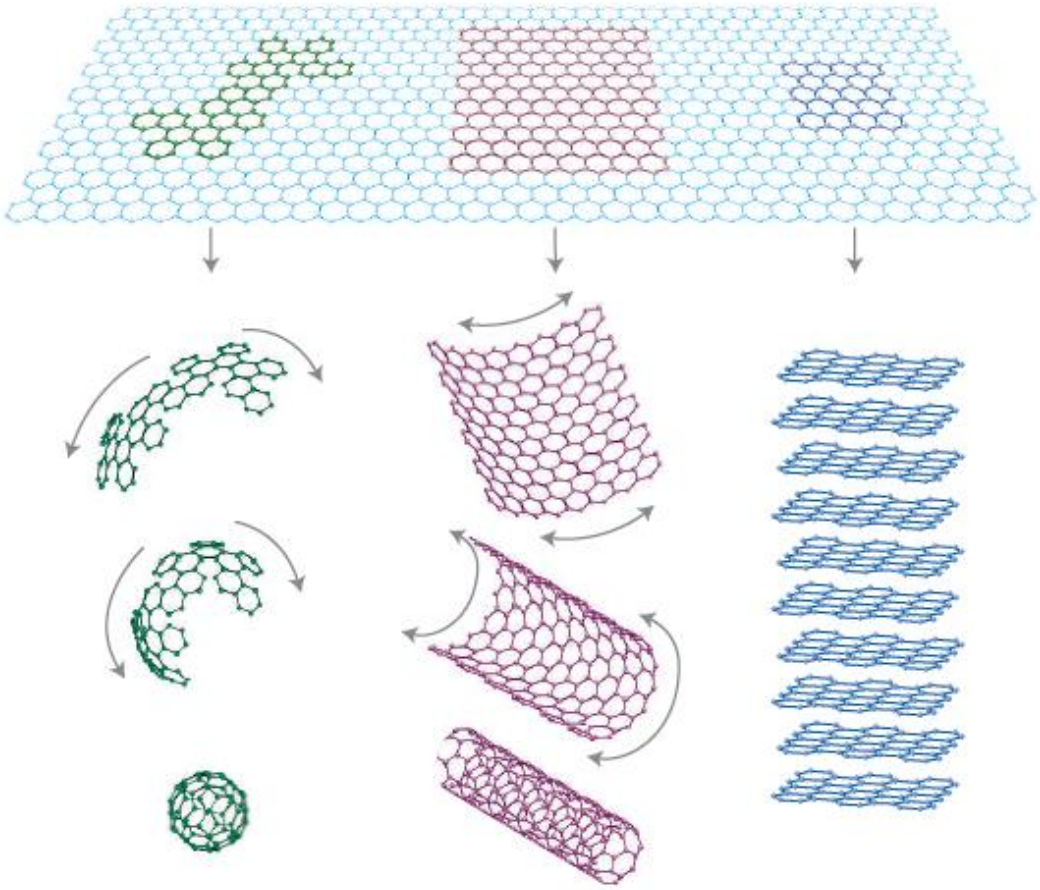

Figure 1-1. Schematic representation showing that graphene forms the basic building block of various carbon allotropes. Figure adapted from "The Rise of Graphene", by Geim, A.K and Novoselov, K.S., *Nature Materials* **2007** (6) 183-191.

There are a number of methods devised for the production of GS like exfoliation,[1, 7-9] epitaxial growth,[7] chemical vapor deposition (CVD),[7, 10-18] pyrolysis,[19-20] chemical synthesis,[21-29] arc discharge,[22, 29-34] carbon nanotube (CNT) slicing,[35-36] solvothermal,[10, 22, 37-39] electrically-assisted synthesis,[40-42] etc., each with advantages and dis-advantages. For example, mechanical exfoliation of graphite yields GS with high electron mobility

and lowest number of defects, but it has the disadvantage of low GS production. On the other hand graphite oxide reduction[25] yields high production rates of GS, but has the disadvantage of being a slow process and producing GS with low bulk density. High quality defect free graphene can be produced via sonication, functionalization, electrochemical exfoliation, super acid dissolution of graphite, alkylation of graphene derivatives, thermal exfoliation, and chemical reduction of graphene oxide.[27, 43] A review article by Potts et al.[44] discusses the utilization of exfoliation, functionalization and reduction methods for synthesizing nanocomposites. Other techniques that use a bottom up approach such as epitaxial growth on metal substrates using CVD,[11, 45-51] organic synthesis,[24, 50, 52-53] arc discharge,[30, 54] chemical conversion,[24, 28-29, 54] carbon monoxide (CO) reduction,[55] and CNT slicing[36, 56-59] have also been tried to synthesize graphene. Overall the production method depends on the final application of GS.

Ab initio DFT calculations[60] indicate that GS are stable up to 1500 K. They show Young's modulus of 1.0±0.1 TPa and intrinsic strength of 130±10 GPa.[61] Balandin *et al*.[62] measured the intrinsic thermal conductivity of individual GS, ~ $5.1\pm0.7\times10^{3}$W/mK, in agreement with the simulations reported by Hu *et al*.[63] Other measurements for thermal conductivity of GS have been reported, for example by Cai et al.[64] and Faugeras et al.[65] who observed that the thermal conductivity of supported GS is smaller than suspended GS. Due to their excellent properties such as high thermal and electrical conductivity, high mechanical and fracture strength, high surface area, high aspect ratio, etc., GS have been recognized as interesting candidates for applications such as the fabrication of, *e.g*., integrated circuits,[66-67] ultra-high-frequency transistors,[68,69] transparent conducting electrodes,[70-73] solar cells, quantum dots,[74-75]

optical modulators,[76] thermal interface materials,[77] ultra-capacitors,[78] sensors,[79] electromechanical resonators,[80] biomedical devices,[81] and GS-based nanocomposites. Among recent propositions is the 'graphene paper',[82] with tensile modulus of up to 35 GPa and electrical conductivity of ~ 7200 S/m. The applications that we are interested in are the use of GS as fillers in nanocomposites and as membranes for water desalination. These applications are discussed in detail in Sections 1.1 and 1.2. Since these two applications are not interrelated, the thesis is divided into two parts. The first part of the thesis discusses about GS-based nanocomposites in Chapters 2, 3, 4 and 5. Our progress in modeling GS membranes for desalination applications is discussed in Chapter 6.

1.1 Graphene-based Nanocomposites

Structured composites attract enormous attention for several reasons, including the promise to enhance the properties of the parent polymers (mechanical properties, permeability, thermal and electrical conductivity, etc.),[83-88] while maintaining the typical polymer light weight. The composites superior mechanical properties have been exploited, e.g., by Honda Jet, whose fuselage is a carbon composite, and by Boeing's 787 Dreamliner, in which composites promise 20% fuel savings compared to other planes of similar size. Carbon-based nanocomposites (materials with fillers with at least one dimension less than 100 nm) promise multi-functional properties, *e.g.*, electrical and thermal conductivities in addition to enhanced mechanical strength.[89-97] For example, carbon nanotubes (CNT), because of their exceptional intrinsic thermal transport properties[98-99] coupled to their percolation thresholds even below 1% by

volume, stimulated a wealth of enthusiasm.[100] Unfortunately, experimental measurements showed only modest increases in the composite thermal conductivity with respect to the thermal conductivity of the pure matrix material.[100-101] Both theoretical[102] and experimental[103] investigations agree that the worse-than-expected composites performance is due to poor coupling between the CNT fillers and the polymer matrix. More specifically, molecular simulations showed that when heat flows from the CNT to the surrounding polymer matrix '*the heat energy first flows from the high frequency modes to the low frequency transverse modes*', and then transfers to the surrounding matrix.[102] This latter step is controlled by the poor coupling between the vibrational modes in the CNT and the surrounding matrix.[104] The resistance to heat flow at the interface, the thermal boundary resistance (also known as Kapitza resistance),[105] is associated with differences in the phonon spectra, and weak contacts, between filler and matrix.[102, 106] Thus the interfacial resistance strongly depends on the presence of low frequency vibration modes in the CNTs and decreases as the length of the CNT increases. These results suggest that when the CNTs become more flexible (eg. longer and larger), the Kapitza resistance decreases. GS might be promising candidates to reduce Kapitza resistance.

GS and graphene ribbons[4, 107-108] are attracting enormous research attention because of their exceptional properties such as quantum Hall[109,110,111] and ambipolar electric field effects,[1] plus extraordinary mechanical stiffness and fracture strength.[5, 45, 68, 112] They are also relatively inexpensive to manufacture.[1-3, 113-114] GS could be used as fillers to enhance the mechanical and thermal transport properties of polymer composites. To

optimize the properties of the composites, it is necessary to produce large quantities of individual GS and to control the dispersion of nanoparticles within the polymer.

To address the first challenge, several techniques have been recently developed, including mechanical exfoliation,[87] the reduction of graphite oxide layers previously obtained by thermal expansion[89] with subsequent stabilization by amphiphilic polymers,[114] and chemical treatment of expandable graphite.[115] The latter process yields 'nanoribbons', elongated structures with width below 10 nm. A review article[116] discusses a number of synthetic routes available for the production of GS. Chemical routes yield GS of as few as 42 carbon atoms,[24] and also graphene 'nanodots' of 130-170 carbon atoms.[117,118] Cai et al. recently reported a bottom-up method, based on the surface-assisted coupling of molecular precursors, that reliably yields graphene nanoribbons of less than 10 nm in width.[75] Larger and less uniform GS can be obtained by exfoliation.[1, 119] Schniepp *et al.*[108] proposed a thermal exfoliation process, Stankovitch *et al.*[120] proposed a functionalization-reduction process of graphene oxide sheets, and Shen *et al.*[121] produced GS platelets by first exfoliating oxidized graphite, and subsequently reducing it *in situ*. Similar processes have been used by Fang et al.[122] who, in addition, took advantage of the oxygenated groups present in partially reduced graphene oxide sheets to graft short polystyrene chains onto graphene planes and edges.

GS are found as crumpled sheets ~1μm in diameter. According to *ab initio* calculations, the wrinkles in GS are due to the presence of defects (*e.g.*, rings of 5, or 7, carbon atoms), epoxy, hydroxyl, and other oxygenated groups.[108, 123] The carbon atoms at the GS edges are carbene-like, with the triplet ground state being the most common, or carbyne-like, with the singlet ground state being the most common.[124] GS also contain

some epoxy, carboxyl and hydroxyl groups on their surface and edges[82] enabling reactions with other functional groups.[125-127] Thus it is conceivable[128,129-130] to functionalize the GS edges with a number of chemical groups, and to incorporate GS in a variety of polymers.[108,120]

GS can be dispersed within polymers by sonicating expanded graphite in tetrahydrofuran (THF), shear mixing the sheets within a polymeric solution [*i.e.*, of poly(methyl methacrylate), PMMA], followed by THF removal.[97] Using this procedure, Ramanathan *et al.*[97] obtained GS-PMMA nanocomposites with electrical conductivity far superior than that of graphite-PMMA composites at similar filler loadings, and with enhanced storage modulus. In another study, Ramanathan *et al.*[131] obtained significant glass transition temperature (Tg) increases for poly(acrylonitrile) and PMMA using a solution mixing process upon modest loadings of functionalized GS. Wakabayashi *et al.*,[88] employed solid-state shear pulverization to disperse GS within polypropylene. The resultant nanocomposite showed improved mechanical properties (measured in terms of the Young's modulus and yield strength). Yu et al. also reported good GS dispersions in an epoxy.[132]

Several alternative approaches have been attempted to improve the stability of dispersions containing GS. The fact that GS contain epoxy, carboxyl and hydroxyl groups on their surface and edges[82] may enable chemical alteration routes.[125-126] This possibility was demonstrated by Li *et al.*,[82] who produced stable GS aqueous dispersions taking advantage of electrostatic stabilization. Along the same lines, the synthetic production route proposed by Yang *et al.*[24] yields GS whose edges can be functionalized by, *e.g.*, alkane chains. This is the stabilization route pursued in this

thesis. Alternatively, GS dispersions can be stabilized by polymeric additives. For example, stable aqueous dispersions of GS were prepared using a water-soluble pyrene derivative as a stabilizer,[133] and electrically conductive graphene-polymer nanocomposites were prepared by mixing exfoliated functionalized graphite oxide sheets with polystyrene, acrylonitrile-butadiene-styrene and styrene-butadiene copolymers.[120]

We are interested in composites in which GS are dispersed within organic oils. Our goal is to control the thermal transport properties of composites by manipulating the assembly of GS. Simulation studies by Striolo et al.[134-135] have shown that it is possible to control the aggregation of colloidal nanoparticles by tuning the effective pair interactions. By exploiting short side chains of various chemical functionalities it is possible to obtain short colloidal nanowires, spherulites, or uniform dispersions. By making use of these basic principles, it might be possible to functionalize GS with chemical functionalities.

According to *ab initio* calculations, the GS wrinkles are due to the presence of defects (e.g., rings of 5, or 7, carbon atoms), epoxy, hydroxyl, and other oxygenated groups.[108, 123] The carbon atoms at the GS edges are carbene-like, with the triplet ground state being the most common, or carbyne-like, with the singlet ground state being the most common.[124] Thus it is possible[129-130] to functionalize the GS edges with a number of chemical groups. Such functionalized materials could be incorporated in a variety of polymers, including polystyrene[120] and PMMA.[108]

Because single GS are less rigid than CNTs, the Kapitza resistance in GS-oil composites should be significantly lower than that in CNT-oil ones. The goal of this thesis is to verify this hypothesis by conducting equilibrium and non- equilibrium molecular dynamics simulations. Furthermore, because it is possible to decorate GS with chemical functionalities compatible with polymer matrixes, it will be possible to efficiently disperse GS within organic materials. If both our hypotheses hold true then GS-based nanocomposites will have tremendous thermal properties for a fraction of the cost of CNT-based nanocomposites.[136]

We conducted molecular dynamics (MD) simulations to assess the Kapitza resistance in systems composed by GS and oils. We employed non-equilibrium molecular dynamics (NEMD) simulations to study how heat flows from GS to the surrounding organic matrix. It is necessary to describe with atomistic precision both GS and the matrix, thus we conducted extensive equilibrium MD simulations[137] to determine the structure of GS in oils and the packing of oils near GS. In Chapter 2, we report equilibrium MD simulations for pristine and functionalized graphene nanosheets dispersed in liquid organic linear alkanes (oils). The simulations are conducted at room conditions in the NPT and NVT ensembles. The parameters of interest are GS size, size of functional groups, and the oils molecular weight. Due to computing limitations, we considered GS containing 54, 96, and 216 carbon atoms. The organic oils considered are n-hexane, n-octane and n-dodecane and the functionalities considered are linear and branched alkanes. These simulations will allow us to understand how the oil molecules pack at the oil-GS interface. The packing depends on the molecular weight of oils as well as on the size of GS. We identified those oils that pack better (e.g., higher densities) close to

the GS interface because we expect that higher interfacial densities will present lower resistances to heat flow. The simulations will also help us identify if it is possible to obtain stable dispersions of GS in organic oils by functionalizing the GS with alkane chains; and the minimum number of functional groups (alkane chains) necessary for a particular GS size to obtain stable dispersions of GS in organic oils.

NEMD simulations are then performed on the GS-oil systems identified during the equilibrium simulations (those with higher densities at the GS-oil interface, and systems with stable dispersions of GS in oils). Two protocols are available. In the first the system is initially equilibrated within the NPT ensemble at room conditions. Then only the GS is heated to 500 K (by rescaling the atomic velocities) and NVE simulations are conducted to monitor the GS temperature decay. By fitting the temperature decay with an exponential function it is possible to estimate the Kapitza resistance.[102] In the second approach the GS particle is continuously heated and the same amount of heat is simultaneously subtracted from the boundaries of the simulation box. This protocol yields temperature profiles across the simulation box from which it is possible to extract estimates for the Kapitza resistance.[102, 138] Due to the irregular structure of GS in oil, we used the first protocol. In Chapter 3 we assess the Kapitza resistance in GS – oil nanocomposites and compare it to results available for CNT and GS – based composites. The successful completion of these simulations will allow us to understand the molecular mechanism of heat flow from GS to oil, which is necessary to design the molecular components for a thermally conductive oil-GS composite material. These simulations will help us determine if the alkane chains grafted to the GS increase or decrease the Kapitza resistance at GS-oil interface compared to pristine GS.

Because when dispersed in a matrix GS tend to agglomerate and because GS agglomeration increases with GS volume fraction, it is important to estimate the Kapitza resistance at the GS-GS interface. Both experiments and simulations have investigated the Kapitza resistance between CNT contacts and found that the resistance at the CNT-CNT interface[139-144] is larger compared to that of the CNT-matrix interface when the matrix is octane,[102-103] epoxy,[145] an aqueous suspension,[146] etc.[147] If, as was observed for CNTs, the thermal boundary resistance at GS-GS junctions is larger than that at GS-matrix interfaces, it might be beneficial to minimize GS-GS contacts in designing thermally conductive composites. In Chapter 4 we assessed the Kapitza resistance at the GS – GS interface in octane and in vacuum and compared it to results available for CNT – CNT interface.

We not only studied how heat flows from one GS to the matrix and one GS to another GS, but also how heat flows from one GS to the matrix, and then back to another GS. These simulations will help us to understand if there is a preferential organization of GS within the polymer matrix that maximizes heat transfer within nanocomposite materials. Because one GS could be described as a discoid particle, it should be possible to control the morphology of GS-based nanocomposites. In other words, by varying the GS loading, and possibly by controlling the manufacture procedure (e.g., via the application of shear stresses) it could be possible to promote the formation of nematic vs. isotropic phases. The overall performance of the resultant material will then depend significantly on the GS relative arrangement at the microscopic scale.[148] Exploiting the high thermal conductivity of individual GS and the possible appearance of nematic phases might lead to nanocomposites with anisotropic heat-transfer characteristics (high heat transfer in

the direction parallel to the GS planes, low in that perpendicular). To explore this possibility, we conducted equilibrium MD simulations to provide evidence for the appearance of nematic phases at sufficient GS volume fraction, and then calculated the thermal conductivity of the resulting GS-oil nanocomposite using NEMD simulations. We also estimated the macroscopic thermal conductivity in GS-oil nanocomposites using Monte Carlo simulations. The simulation methodologies and the results obtained are discussed in Chapter 5.

1.2 Graphene-based Desalination Membranes

Water scarcity for agricultural use and human consumption is one of the major resource crises[149] worldwide. Although 71% of the earth's surface is covered with water in the oceans, seas, and ice at the poles,[150] only 3% of earth's water is fresh and suitable for human consumption. Given the abundance of salty water from seas and oceans, there is a need for purifying such water using economic and environmentally friendly processes.

Seawater desalination has long been practiced; ion concentration in seawater is ~ 0.6 M.[151] The most widely used commercial desalination techniques are reverse osmosis (RO),[152] electro dialysis,[153] and nanofiltration.[154] Although RO, which uses high pressure to force water (but not salt ions) through a porous membrane, is believed to have the greatest practical potential, all desalination techniques are energy and capital intensive. Nanoporous membranes, which promise to be more efficient than existing membranes, could yield savings in the energy consumption during RO operations. Recent experimental[155-156] and simulation studies[157-159] have shown fast transport of water through carbon nanotube (CNT) membranes, especially at the critical pore

diameter (Ø) of ~ 7 Å, when water passes through the pore but ions do not.[160] Such fast water flow is attributed to the frictionless and smooth inner walls of the CNT.[159] Nasrabadi et al.[161] demonstrated that charged CNTs can be used as nano-electrodes to separate Na^+ and Cl^- ions from NaCl solution. In addition, the ends of CNT pores can be functionalized with various chemical groups that could provide gating properties.[162-164]

The design of RO membranes can be improved utilizing the results obtained from molecular dynamics (MD) simulations. For example, both Hughes et al.[162] and Corry et al.[163] showed that charged functional groups can help block the ions, but at the cost of reduced water diffusion (mostly because of steric effects). Tofighy et al.[165] showed that oxidized CNT membranes can be very effective for water desalination. They also reported that increasing the feed concentration, temperature and flow rate, or decreasing the pressure, can enhance the performance of oxidized CNT membranes. Suk et al.[166] compared the transport of water through a GS and a CNT membrane. For smaller pores, they found that CNT membranes provide a higher flow rate of water than GS membranes. For larger pores, the flow rate of water is higher through GS membranes, due to the reduced energy barrier at the entrance of the GS pore. The authors also discussed how water-water hydrogen bonds affect the translocation process across the membrane. Sint et al. predicted that functionalized GS nanopores could serve as ionic sieves of high selectivity and transparency.[167] Cohen-Tanugi and Grossman[168] found that both the size and chemical functionalization of GS pores play an important role in blocking the salt ions while allowing the water flow through the GS membranes. The observed water flux in both membranes (they considered pristine and OH-functionalized pores) was predicted to be 2-3 times faster than the current state-of-the-

art desalination technology at equal pressure drop. Should these predictions be verified experimentally, GS membranes, likely cheaper than CNT ones, could provide significant advantages in RO applications.

The properties of GS such as high aspect ratio,[169] high mechanical stiffness,[61] and small thickness[170] make them attractive for manufacturing membranes, as water flux scales inversely with membrane thickness.[171] Pores have been fabricated on GS by controlled electron-beam exposure in a transmission electron microscope.[172] The resultant porous GS have been used in DNA translocation[173-174] and biosensing.[175] Other techniques, including diblock copolymer templating,[176] helium ion beam drilling,[177] and chemical etching,[178] have also been used to generate pores on GS. O'Hern et al.[179] transferred a single layer graphene onto a porous polycarbonate substrate, obtaining membranes in which pores of 1-15 nm diameter were observed. Various research groups have synthesized GS functionalized with carboxylate,[180] hydroxyl,[180] and amine-terminated polystyrene.[181] Mishra et al.[182] synthesized GS membranes by first exfoliating graphitic oxide and then functionalizing it with carboxylic (-COOH), carbonyl (-CO), and hydroxyl (-OH) groups. These functionalized GS have been used for simultaneous removal of high concentrations of arsenic and sodium from seawater. Sun et al.[183] investigated the penetration of sodium salts, heavy-metal salts, organic contaminants, and a mixture of their aqueous solutions through graphene oxide (GO) membranes. The results show that sodium salts pass more quickly through the GO membranes than the heavy-metal salts. Copper salts and organic contaminants like rhodamide B are completely blocked because of their strong interactions with the GO membranes.

To further the design of effective GS-based membranes for water desalination, we quantify the effect of functionalizing pores with COO^-, NH_3^+ and OH groups on the pores ability of rejecting NaCl. The potential of mean force (PMF) along the vertical distance from the pore center into bulk aqueous solutions is calculated for both water and Na^+ and Cl^- ions. The pores considered have diameter 14.5, 10.5, and 7.5 Å. The results are presented in Chapter 6 and indicate that effective ion exclusion can only be achieved using non-functionalized (pristine) pores of diameter ~ 7.5 Å, while the ions can easily penetrate pristine pores of diameter ~ 10.5 and 14.5 Å. Carboxyl functional groups can enhance ion exclusion for all pores considered, but the effect becomes less pronounced as both the ion concentration and the pore diameter increase. When compared to a carbon nanotube (CNT) of similar pore diameter, our results suggest that GS pores functionalized with COO^- groups are more effective in excluding Cl^- ions from passing through the membrane. Our results suggest that narrow graphene pores functionalized with hydroxyl groups remain effective at excluding Cl^- ions even at moderate solution ionic strength. The results presented could be useful for the design of water desalination membranes.

Chapter 7 has a discussion on the recent trends in graphene related to my research; in Chapter 8 we summarize our main conclusions and highlight some questions that require further research; in Chapter 9 (Appendix) we provide the details of the umbrella sampling technique used in Chapter 6 and provide some additional details regarding the selection of simulation timestep and how we optimized the number of processors used to run the simulations; and in Chapter 10 we provide a list of all the references used in this thesis.

2. Molecular Design of Stable Graphene Nano-Sheets Dispersions

The material presented below was published in 2008 in volume 8, issue 12, and page 4630 of the ACS journal Nano Letters.

2.1 Introduction

GS are receiving enormous scientific attention because of extraordinary thermal, electronic and mechanical properties. These intrinsic properties will lead to innovative nano-composite materials that could be used to produce novel transistors and thermally-conductive polymeric materials. Such applications are currently hindered by the difficulty of producing large quantities of individual GS and by the propensity of these nanoparticles to agglomerate when dispersed in aqueous and/or organic matrixes.

Our group is interested in dispersing GS in aqueous and/or organic systems by taking advantage of steric stabilization. The availability of reactive groups on the GS edges will be exploited to graft chemical functionalities on the GS, as demonstrated by Yang *et al*.[24] Based on theoretical results obtained for spherical colloids,[134, 184] we expect that by employing functionalities such as polymer brushes to the GS edges we will induce effective GS-GS repulsions that will stabilize GS-containing dispersions. However, some fundamental questions need to be addressed, including '*what type of functionalities provides the desired stabilization*?' And '*what is the minimum number of such functionalities for a given graphene sheet*?' To address these questions we employ molecular dynamics simulation techniques. Simulations will prove advantageous in the search for GS stabilization methods, as well for understanding the effect that

functionalizing GS will have on the intrinsic properties of pristine GS. The advantage of theoretical contributions stems from the fact that no chemical synthesis is required for assessing various stabilization routes (although experimental verification will be necessary for practical applications), thus various possibilities can be studied and pros and cons carefully evaluated. As a first example, Barnard *et al.*,[60] using *ab initio* techniques, showed that small GS do not transform into carbon nanotubes even at elevated temperatures, although they undergo extensive vibrational motion.[60] Another advantage inherent to simulation studies is that the detailed analysis of the simulation results allows us to understand the molecular mechanisms responsible for the GS aggregation, as well as those that can be exploited to stabilize GS dispersions. One drawback is that, because of computational power limitations, only small systems can be simulated at the all-atom level. The simulation results reported in this Letter were obtained for GS of 54 and 96 carbon atoms each. Thus the work presented is applicable to GS obtained by the synthetic route proposed by Yang *et al.*[24] Despite the existing limitation on the GS size that can be simulated, the fundamental lessons that we learn from our model system can be appropriately extended to larger GS, for example using coarse-grained models that could be implemented based on the results presented here.[185] Our molecular dynamics simulations are performed on systems that contain low-molecular-weight oils (n-hexane, n-octane, and n-dodecane). These oils are frequently used in the industry and therefore studying the properties of GS-oil systems may lead to the design of enhanced lubricants for extreme applications (e.g., heat-conductive lubricants). All the simulations were conducted at room conditions. The densities of

liquid n-hexane, n-octane and n-dodecane at 300K are 0.649 gm/cm^3, 0.6964 gm/cm^3, and 0.7493 gm/cm^3, respectively.

The simulations are conducted at the limit of low GS concentration within the organic oils. Under these conditions, by calculating the radial distribution functions between the GS centers of mass (center-to-center RDFs in what follows), it is possible to obtain effective pair potentials of mean force (W), from which a number of thermodynamic properties can be calculated.[186] It is also possible to exploit this information to develop coarse-grained potentials that will allow us to simulate larger systems at higher GS concentrations.[185] Examples of similar applications are detailed in our previous publications.[187-192]

To provide good compatibility between the GS fillers and the low-molecular-weight oils, the GS functionalities are either linear or branched alkanes. We found that: (1) it is possible to maintain individually dispersed GS within low-molecular-weight oils by functionalizing the GS edges; (2) branched functionalities are far more effective than linear ones for GS stabilization; (3) the effectiveness of the stabilization is a consequence of the excluded volume of the branched functional groups; and (4) the functionalities affect, albeit slightly, the packing of oil molecules around the GS. In the remainder of this Chapter we discuss our main results.

2.1 Simulation Details

To conduct our simulations we employed the package LAMMPS.[193-194] All results were obtained using equilibrium molecular dynamics (MD) simulations within the NVT and NPT ensembles. In the NVT ensemble the number of particles (N), the simulation box

volume (V), and the temperature (T) are maintained constant. In the NPT ensemble the system volume is allowed to fluctuate to maintain the pressure (P) constant. Periodic boundary conditions were applied in all the three dimensions. The size of the simulation box was approximately 90×90×90 Å in all the systems considered. In all cases the time step was of 1 fs.

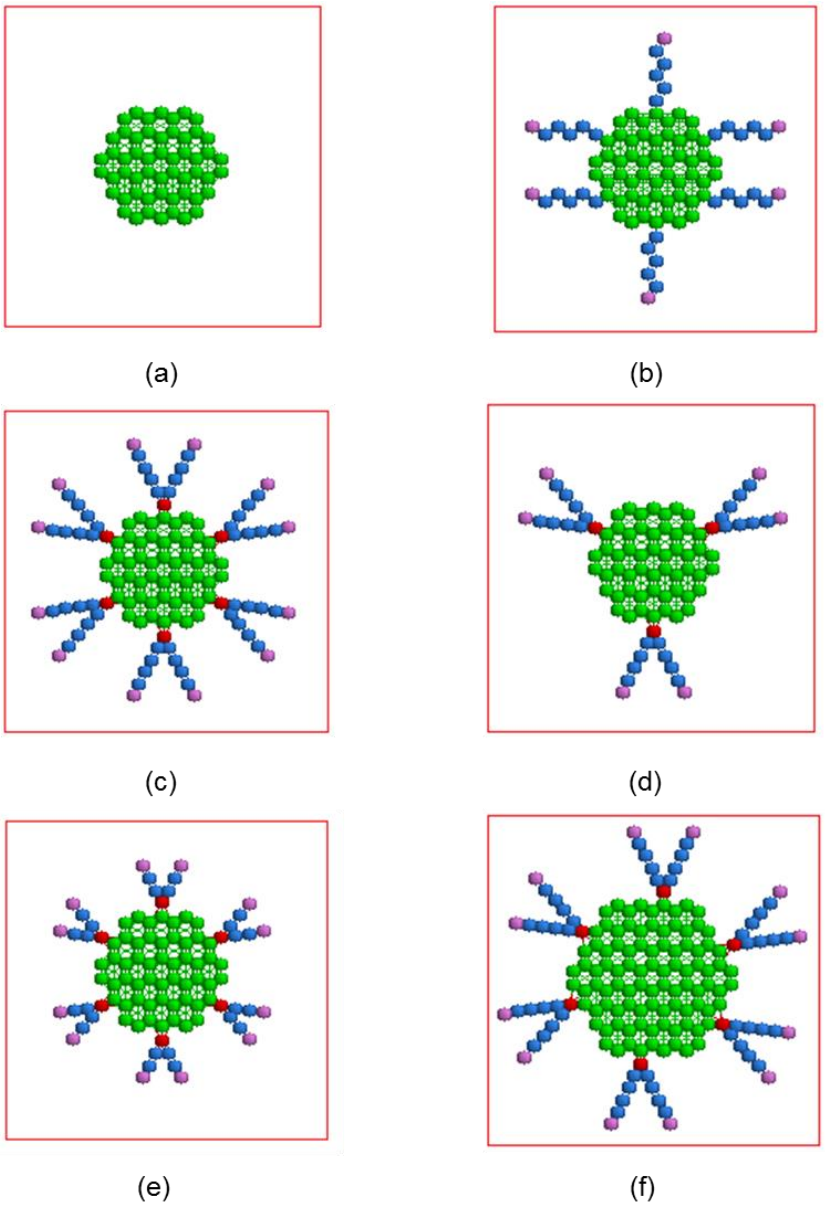

Figure 2-1 Schematic representation of the pristine graphene sheets (GS) considered in this work, composed of 54 carbon atoms (panel a), as well as of the functionalized GS. The functional groups are always alkanes, grafted to GS edge atoms. Five functionalized GS types are considered: those obtained by grafting 6 alkanes of 6 carbon atoms each to one GS (panel b); those obtained by grafting 6 branched alkanes of 11carbon atoms each (panel c); those obtained by grafting 3 branched alkanes of 11 carbon atoms each (panel d); those obtained by grafting 6 branched alkanes of 7carbon atoms each (panel e); and those obtained by grafting 6 branched alkanes of 11 carbon atoms each to GS of 96 carbon atoms (panel f) . Green spheres represent carbon atoms in GS; red, blue, and purple spheres represent CH, CH_2, and CH_3 groups in the alkane functionalities, respectively.

Each GS was composed of 54 carbon atoms. The Tersoff force field[195-197] was employed to describe the interactions among these atoms. In the Tersoff force field, the potential energy is modeled as a sum of pair like interactions, where, however, the coefficient of the attractive term in the pair like potential depends on the local environment, yielding an effective many-body potential. Interactions between carbon atoms belonging to different GS were described using Lennard-Jones potentials. To describe alkanes we implemented a united atom approach and the parameters were taken from the NERD force field.[198-199] The alkanes considered were n-octane, n-hexane and n-dodecane. Within the united-atom description, an n-alkane molecule is described as a flexible linear chain of methylene (CH_2) pseudo atoms terminating at both ends with methyl (CH_3) pseudo atoms. In the NERD force field, the non-bonded potential between interaction sites, which are separated by more than three bonds or belong to different molecules, is described by the Lennard-Jones 12-6 potential. The interactions between GS and alkanes were described by the 12-6 Lennard-Jones (LJ) potential. The parameters were obtained by Lorentz-Berthelot rules[137] from those of the pure compounds.

Parameters and more details necessary to implement both Tersoff and NERD force fields are given in Table 2.1.

In each simulation box the number of linear alkane (organic oil) molecules was 2576 and that of GS was 5. In the initial configuration all these molecules were disposed in a lattice within the simulation box. To prevent excessive forces, the MD simulations, carried out in the NVT ensemble, where initially conducted at very low temperatures

(50K). The system was then heated from 50K to 300K at the heating rate of 100K every 600ps of simulation. The system was then equilibrated in the NPT ensemble at 300K and 1 bar to stabilize the system volume. Once the simulation box volume fluctuated around a constant value, simulations were conducted in the NVT ensemble at 300 K. During the production phase, which lasted up to 120 ns, the system configurations were stored every 100 ps and used for subsequent analysis. The system densities during the production phase were comparable to the experimental densities of the pure liquid organic oils at 300K.

Table 2-1 Potential Energy functions.

NERD force field for alkanes

Bond stretching potential

$$V(r)/k_B = \frac{K_r}{2}\left(r - b_{eq}\right)^2$$

K_r=96 500 K/A^2 b_{eq}=1.54A

Bond bending potential

$$V(\theta)/k_B = \frac{K_\theta}{2}\left(\theta - \theta_{eq}\right)^2$$

K_θ=62 500 K/rad^2 θ_{eq}=114.0^o

Torsional potential

$$V(\phi)/k_B = V_o + V_1(1 + cos\phi) + V_2(1 - cos2\phi) + V_3(1 + cos3\phi)$$

V_o=0 V_1=355.04K

V_2=-68.19K V_3=701.32K

Nonbonded interactions potential

r_{ij}, ε_{ij}, and σ_{ij} denote the distance between the interaction sites, Lennard-Jones well depth and size parameter respectively, for the pairs of atoms *i* and *j*.

$$u(r_{ij}) = 4\varepsilon_{ij}\left[\left(\frac{\sigma_{ij}}{r_{ij}}\right)^{12} - \left(\frac{\sigma_{ij}}{r_{ij}}\right)^{6}\right]$$

TB force field for graphene sheets

The potential energy *E*, as a function of the atomic coordinates, is calculated as

$$E = \sum_i E_i = \frac{1}{2}\sum_{i\neq j} V_{ij} ,$$

$$V_{ij} = f_C(r_{ij})\left[f_R(r_{ij}) + b_{ij} f_A(r_{ij})\right];$$

$$f_R(r_{ij}) = A_{ij}\exp(-\lambda_{ij} r_{ij}) , f_A(r_{ij}) = -B_{ij}\exp\left(-\mu_{ij} r_{ij}\right);$$

$$f_C(r_{ij}) = \begin{cases} 1, & r_{ij} < R_{ij} \\ \frac{1}{2} + \frac{1}{2}\cos[\pi(r_{ij} - R_{ij})/(S_{ij} - R_{ij})], & R_{ij} < r_{ij} < S_{ij}, \\ 0, & r_{ij} > S_{ij}; \end{cases}$$

$$b_{ij} = \chi_{ij}\left(1 + \beta_i^{n_i}\zeta_{ij}^{n_i}\right)^{-1/2n_i}, \qquad \zeta_{ij} = \sum_{k\neq i,j} f_C(r_{ik})\,\omega_{ik} g(\theta_{ijk}),$$

$$g(\theta_{ijk}) = 1 + c_i^2/d_i^2 - c_i^2/\left[d_i^2 + (h_i - \cos\theta_{ijk})^2\right];$$

$$\lambda_{ij} = (\lambda_i + \lambda_j)/2, \quad \mu_{ij} = (\mu_i + \mu_i)/2, \quad A_{ij} = (A_i A_j)^{1/2},$$

$$B_{ij} = (B_i B_j)^{1/2}, \quad R_{ij} = (R_i R_j)^{1/2}, \quad S_{ij} = (S_i S_j)^{1/2}.$$

Indexes *i*, *j*, and *k* label the atoms of the system, r_{ij} is the length of the *ij* bond, and θ_{ijk} is the bond angle between bonds *ij* and *ik*. Singly subscripted parameters, such as λ_i and n_i, depend only on the type of atom (in our case, carbon).

TB parameters for Carbon

A (eV)	1.3936×10^{3}
B (eV)	3.467×10^{2}
λ (Å $^{-1}$)	3.4879
μ (Å $^{-1}$)	2.2119
β	1.5724×10^{-7}
n	7.2751×10^{-1}
c	3.8049×10^{4}
d	4.384×10^{0}
h	-5.7058×10^{-1}
R (Å)	1.95
S (Å)	0.15

Lennard Jones intermolecular potential energy parameters

Pseudo atom	σ (Å)	ε/k_B (K)
CH_3	3.91	104.0
CH_2	3.93	45.8
CH	3.85	39.7
C	3.91	17.0

2.2 Results and Discussion

2.2.1 Mean Square Displacement

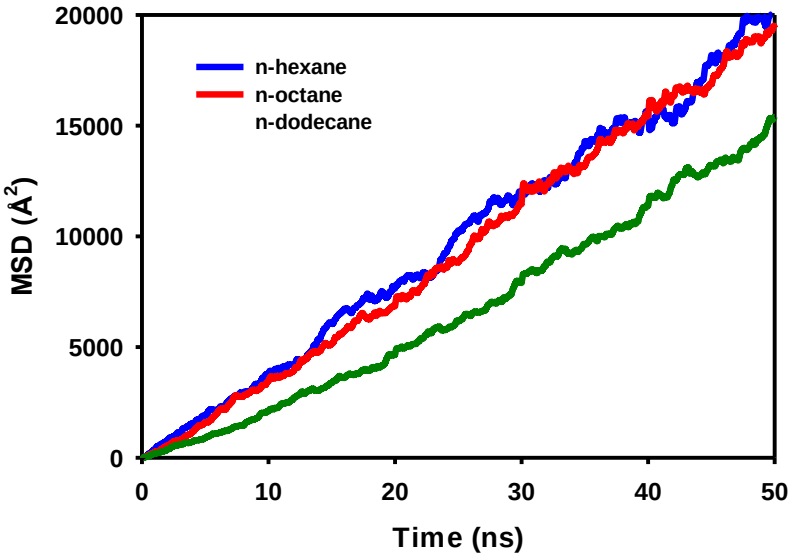

Figure 2-2 Mean square displacement (MSD) as a function of time obtained for GS of 54 carbon atoms functionalized with six branched alkanes (see Fig 2.1c) in n-hexane (blue line), n-octane (red line), and n-dodecane (green line). All simulations were conducted at 300K.

We considered pristine GS (Fig. 2.1a), as well as functionalized GS (Fig 2.1b, 2.1c, 2.1d, 2.1e, 2.1f). In one case 6 linear hexanes were grafted to edge GS atoms as shown in Fig 2.1b. Alternatively, the GS were functionalized with 6 (Fig 2.1c), or 3 branched alkanes with 11 carbon atoms each (Fig 2.1d). Five such GS were immersed, together with 2576 alkane molecules, in cubic simulation boxes of lateral dimension ~9.0 nm. After equilibration (details can be found in the Appendix), the simulations were conducted for up to 120 ns for each system considered. To verify that the simulations were sufficiently long we evaluated the mean square displacement (MSD) of the GS center of mass as a function of time. The results are shown in Fig 2.2 for functionalized

GS of 54 carbon atoms in n-hexane, n-octane, and n-dodecane at 300K. From the slope of the MSD at long time it is possible to extract the self-diffusion coefficient using the Einstein relation. Our calculations yield diffusion coefficients of $6.87 \cdot 10^{-5}$ cm^2/s, $6.47 \cdot 10^{-5}$ cm^2/s, and $5.13 \cdot 10^{-5}$ cm^2/s for functionalized GS in n-hexane, n-octane, and n-dodecane, respectively. Further, from the results in Fig 2.2 we can assess how far each GS travels during the 120 ns of a typical simulation run (i.e., a distance equivalent to approximately 2 simulation box sizes). Although longer simulations are always desirable, this result guarantees that our simulations sampled properly equilibrated configurations.

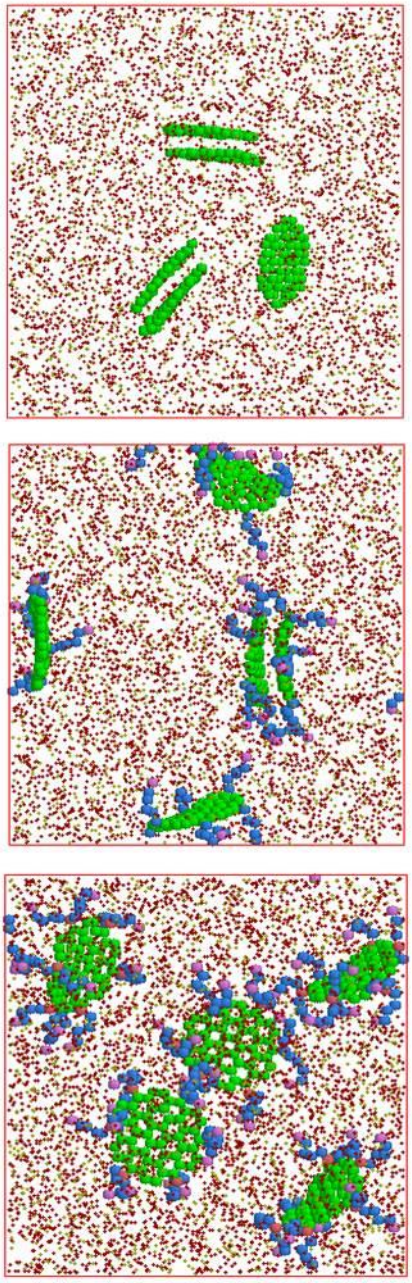

Figure 2-3 Representative simulation snapshots for GS of 54 carbon atoms in n-octane at 300K. GS are shown with the color code of Fig 2.1. Red and yellow spheres represent CH_2 and CH_3 groups of n-octane, respectively. Visual inspection suggests that pristine GS aggregate yielding 'pancake stacks' (top), as well as GS functionalized with linear chains of six carbon atoms (center). When the GS are functionalized with 6 branched alkanes of 11 carbon atoms each they remain well dispersed in n-octane after 120 ns of simulation (bottom).

2.2.2 Graphene – Graphene Radial Distribution Function

When pristine GS of 54 carbon atoms (Fig 2.1a) were simulated, they aggregated after a few nanoseconds yielding 'pancake stacks' in n-octane at 300 K. A representative simulation snapshot is shown in Fig 2.3 (top panel). The distance between the GS in the stacks is ~0.4 nm. When the GS were functionalized with 6 linear alkanes of 6 carbon atoms each (Fig 2.1b) they still agglomerated in n-octane as shown in Fig 2.3 (center panel), but when six branched alkanes of 11 carbon atoms were grafted to the edges of GS (Fig 2.1c) the GS did not agglomerate after 120 ns of simulation (Fig 2.3, bottom panel). Thus our simulations demonstrate that by functionalizing the GS edges it is possible to induce sufficient entropic repulsion between GS in oils to guarantee the stability of the dispersions, provided that branched functionalities are employed. The mechanism by which stabilization occurs will be discussed later.

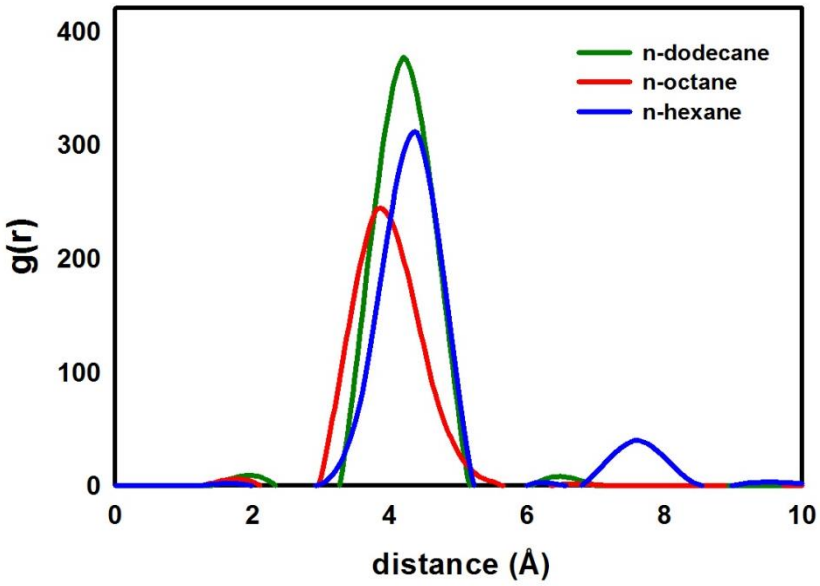

Figure 2-4 Center to center radial distribution functions (RDFs) computed between 5 pristine GS of 54 carbon atoms (see Fig 2.1a) in oils. Results were obtained in n-hexane (blue line), in n-octane (red line), and in n-dodecane (green line). All simulations were conducted at 300K.

To understand the effect of solvent on the self-aggregation of GS, simulations were carried out for GS in n-hexane, n-octane and n-dodecane. To characterize the systems simulated we computed the radial distribution functions (RDFs) between the GS center of mass (center-to-center RDFs). Typical results obtained for pristine GS of 54 carbon atoms are shown in Fig 2.4. Pristine GS agglomerate in the three oils at 300K. The RDFs (Fig 2.4) correspond to the data obtained during 5 ns after the GS agglomerate. The intense peak at short separation and the vanishing RDF at large separation are representative of the strong association between GS. During the simulations the 5 GS formed two agglomerates of 2 GS each in n-dodecane and n-octane, while they formed one agglomerate of 3 GS and one of 2 GS in n-hexane. The agglomerate of 3 GS is responsible for the second intense peak at ~7.5 Å found in the RDF computed in n-hexane. None of the aggregated GS redispersed in the oil during our simulations, which,

in this case, lasted 15 ns. If the simulations were conducted for longer times, all the 5 GS would have likely formed one big pancake-stack aggregate in all three solvents considered.

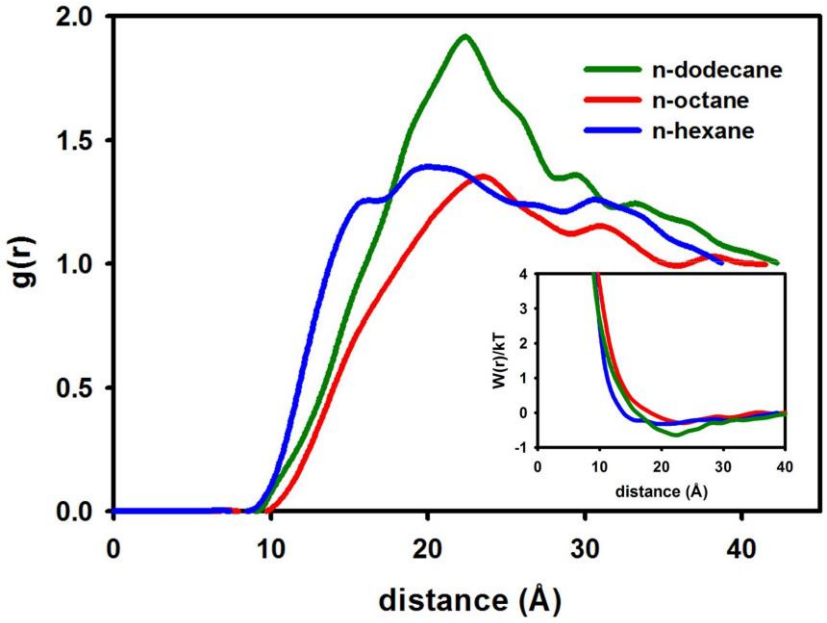

Figure 2-5 Center-to-center radial distribution functions (RDFs) and pair potentials of mean force W (inset) computed for 5 GS of 54 carbon atoms functionalized with 6 branched alkanes of 11 carbon atoms each (see Fig 2.1c). Results were obtained in n-hexane (blue lines), n-octane (red lines), and n-dodecane (green lines). All simulations were conducted at 300K.

The center-to-center RDFs computed for five GS of 54 carbon atoms functionalized with 6 branched alkanes of 11 carbon atoms each dispersed in n-hexane, n-octane and n-dodecane at 300K are shown in Fig 2.5. From the RDFs we obtained effective pair potentials of mean force, which are shown as inset in Fig 2.5. When the RDF is larger than unity the corresponding effective pair potential W is attractive (negative), while when the RDF is less than unity W is repulsive (positive). The RDFs in Fig 2.5 do not show any intense peaks, but instead grow gradually from zero at close separations,

becomes larger than unity at distances between ~1.4 nm to ~ 3.5 nm, depending on the solvent, and then decrease smoothly to unity at larger separations. These features are typically observed between spherical colloids covered by brushes in solution, in which case the brushes provide entropic repulsion at close separations and mid-range attraction that can arise because of depletion forces, or because of other long-range interactions. The fact that RDFs obtained for functionalized GS in oils are similar to those obtained between colloidal brushes may sound surprising because the 'brushes' are grafted only at the GS edges rather than uniformly on the entire nanoparticles. Indeed, non-uniform brush coverage may result in anisotropic attraction between nanoparticles.[135, 200] Quantification of the simulation results is required to clarify these observations.

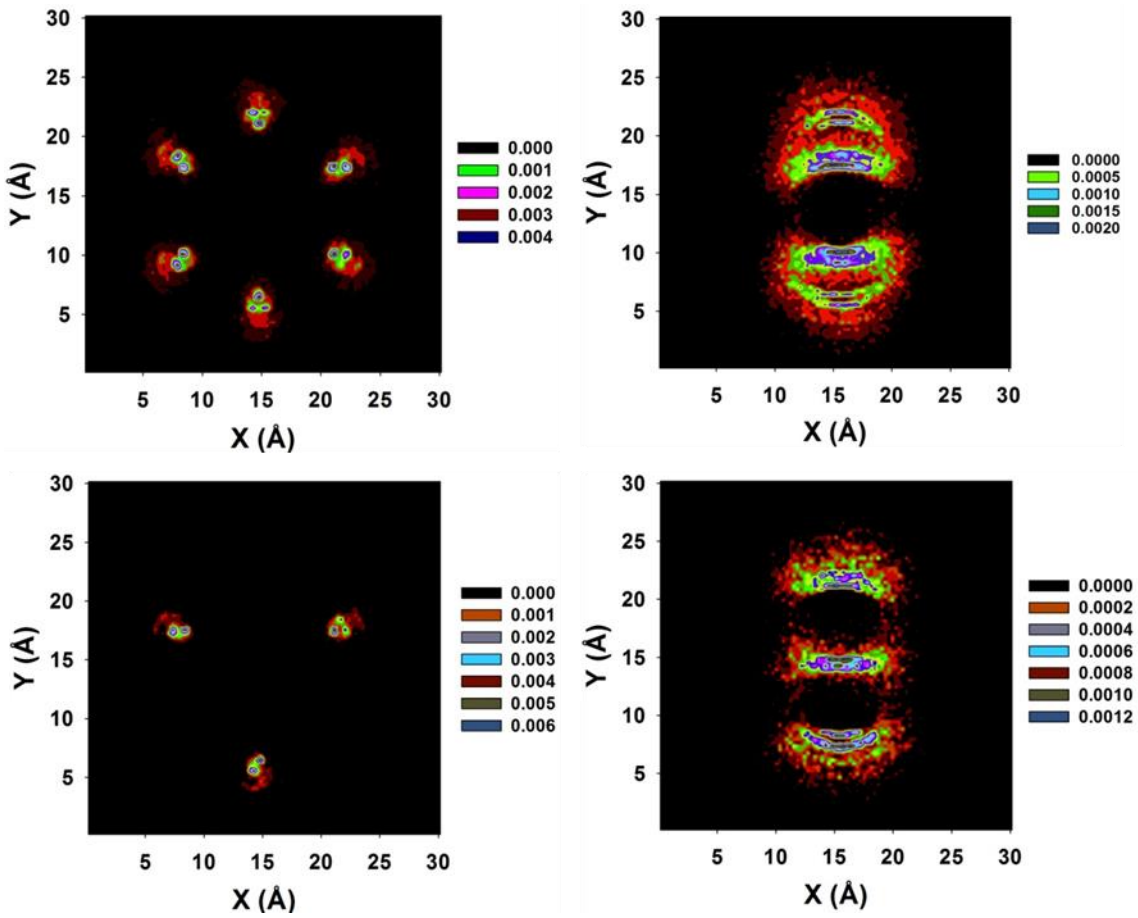

Figure 2-6 Top left: contour plot for the GS of 54 carbon atoms functionalized with 6 branched alkanes of 11 carbon atoms each, top view.
Top right: contour plot for the GS functionalized with 6 branched alkanes, side view.
Bottom left: contour plot for the GS functionalized with 3 branched alkanes, top view.
Bottom right: contour plot for the GS functionalized with 3 branched alkanes, side view.

2.2.3 Contour Density Profiles

To rationalize the molecular mechanism responsible for the stabilization of the GS functionalized with branched alkanes we conducted additional simulation studies in which only one functionalized GS was present within a simulation box containing the alkanes of interest (n-hexane, n-octane, and n-dodecane). The simulations were conducted at 300K and room pressure within the NPT ensemble, and after equilibration

the lateral dimension of the cubic simulation box was ~ 6.5 nm. Then NVT simulations were conducted at 300K for the only purpose of studying the preferential configuration of the functional groups. The results are qualitatively independent on the solvent. We report in Fig 2.6, top panels, the top and side views of the density profiles of the functional groups composed by branched alkanes of 11 carbon atoms grafted to one GS of 54 carbon atoms. The results from the top view (top left panel) clearly indicate the localization of the grafting points for the six branched functional groups. More important are the results shown on the side view (top right panel), which indicate how the functionalities protrude towards both sides of the GS, and effectively render the flat GS a discoid nanoparticle whose width depends on the length of one branch in the functional groups. The symmetric extension of the excluded volume is due to the branched architecture of the functional groups (each linear functional groups of Fig 2.1b preferentially extends towards only one side of the GS). Because of the symmetric excluded volume, it is not possible for the GS considered in Fig 2.5 to aggregate yielding 'pancakes stacks' structures, and consequently the GS dispersions are stable. This mechanism is expected to work even for wider GS, provided that a sufficient number of functionalities is employed, and that the GS diameter is not too large compared to the length of the functional groups. In fact there are two competing interactions that determine the stabilization/aggregation of the GS dispersed in oils. Functionality-functionality excluded-volume effects yield an effective repulsion of entropic origin, while excluded-volume effects due to the discoid GS shape, augmented by GS-GS Van der Waals attractions, yield strong GS-GS attraction.

Since functionalizing the GS with 6 branched alkanes served the purpose of dispersing the GS in oil, simulations were conducted to determine the minimum number of branched alkanes required for obtaining stable dispersions. When 3 branched alkanes were grafted to each GS (Fig 2.1d), the GS aggregated in n-hexane (after 31 ns of simulation) and in n-octane (after 50.7 ns of simulation). In n-dodecane the GS remained dispersed even after 120 ns of simulation. This result was unexpected because longer-ranged depletion attractions are predicted when longer linear solvent molecules are present,[201] but it may simply be due to the fact that the mobility of the functionalized GS is lower in n-dodecane than it is in the other solvents considered here, as shown in Fig 2.1. Thus longer simulations will likely show aggregation of GS functionalized with 3 branched alkanes in n-dodecane. We conclude that 6 branched functionalities are necessary to prevent GS agglomeration in all the three oils considered. To understand why 3 branched functional groups are not effective in stabilizing the GS we again consider the contour plots shown in Fig 2.6. In the bottom panel we report top and side view of the density profiles of the functional groups in one GS of 54 carbon atoms functionalized with 3 branched alkanes. Qualitatively, the density profile for each functional group is very similar to that discussed in the case of GS functionalized with 6 branched alkanes. However, one difference exists when the whole nanoparticle is considered, and it is clearly responsible for GS aggregation. When two GS functionalized with 3 branched alkanes approach each other in a face-to-face relative orientation it is possible to obtain the pancakes stack configuration without encountering significant excluded-volume repulsions by simply rotating one GS by 30° with respect to the other. This rotation allows sufficient room for each functional group

not to experience entropic penalties upon the GS association and therefore the GS-GS attraction prevails leading to the GS association.

In the simulations discussed so far each of the branched alkanes used to functionalize the GS consisted of 11 carbon atoms. Additional simulations were conducted to determine the minimum length of the functional groups required to prevent GS agglomeration. Simulations were conducted for GS functionalized with 6 branched alkanes of 7 carbon atoms each dispersed in n-hexane at 300K. Our results show that even the shorter functional groups are successful in preventing GS agglomeration for up to 120 ns of simulation time. The center-to-center RDF's computed for five GS functionalized with 6 branched alkanes with either 7 or 11 carbon atoms each dispersed in n-hexane at 300K are shown in Fig 2.7. Within statistical uncertainty, we observe that the two data sets are essentially equivalent.

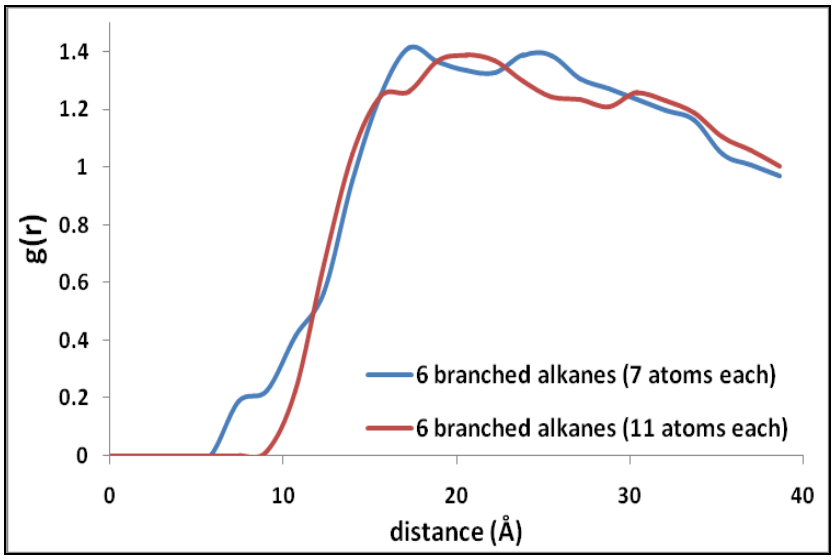

Figure 2-7 Center-to-center RDF between GS of 54 carbon atoms functionalized with 6 branched alkanes. The functional groups contain either 7 (blue line) or 11 carbon atoms each (red line). Simulations are conducted in n-hexane at 300K.

Having established that six branched alkanes are effective in stabilizing GS of 54 carbon atoms in n-hexane, n-octane, and n-dodecane, and having illustrated the mechanism responsible for stabilization, we conducted additional simulations to assess whether the same strategy is successful even for GS of 96 carbon atoms. Equilibrium MD simulations were conducted for these nanoparticles dispersed in n-octane at 300K. The results for the center-to-center RDF are shown in Fig 2.8, where they are compared to those obtained for the GS of 54 carbon atoms. Both nanoparticles are functionalized with 6 branched alkanes of 11 carbon atoms. The results for RDFs and PMFs (inset) indicate that both GS are stable in n-octane at 300K. However, some differences are evident. In particular, the effective mid-range GS-GS attraction becomes slightly stronger when larger GS are considered, and also the RDF becomes larger than zero at center-to-center distances lower than those at which the RDF between GS of 54 carbon atoms does. Both of these results are due to the fact that the GS of 96 carbon atoms attract each other more strongly than those of 54 carbon atoms do. This attraction is expected because of GS-GS excluded volume effects, which become more pronounced as the GS size increases. However, the GS-GS repulsion due to the presence of the functional groups prevents the GS aggregation into pancake staks.

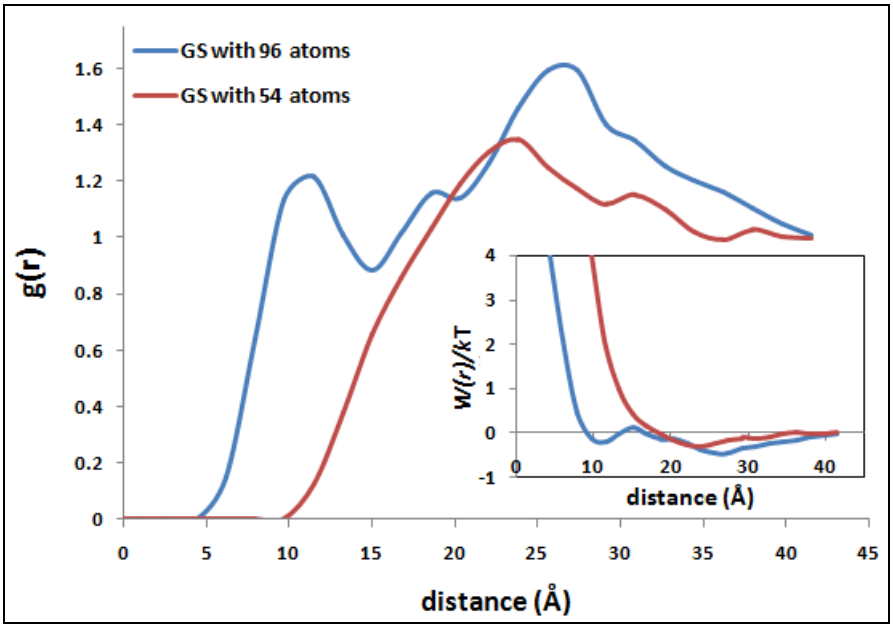

Figure 2-8 Center-to-center RDF between GS with 96 atoms (blue line) and GS with 54 atoms (red line) functionalized by 6 branched alkanes in n-octane at 300K. All the branched alkanes used as functional groups contain 11 carbon atoms.

From the simulation results discussed above, we concluded that functionalizing the GS with 6 branched alkanes successfully prevents GS aggregation in the three solvents considered. The RDFs shown in Figs 2.5, 2.7, and 2.8 are averaged over all possible orientations, but for practical applications it may be interesting to understand how the GS approach each other within the dispersions. Thus radial distribution functions were computed between selected carbon atoms within the GS. We considered edge atoms, as well as those atoms that belong to a hexagonal ring at the center of the GS. The corresponding RDFs, indicated as edge-edge, ring-ring, and ring-edge, are shown in Fig 2.9 for GS of 54 carbon atoms dispersed in n-hexane, n-octane and n-dodecane. In the case of GS dispersed in n-hexane (blue lines) and n-octane (red lines), there are no strong peaks and the RDFs increase smoothly from zero at small distances to unity at

large ones. In the case of GS dispersed in n-dodecane (green lines), a peak is observed at 24 Å in all the RDFs, in agreement with the results obtained for the orientationally averaged RDFs shown in Fig 2.5.

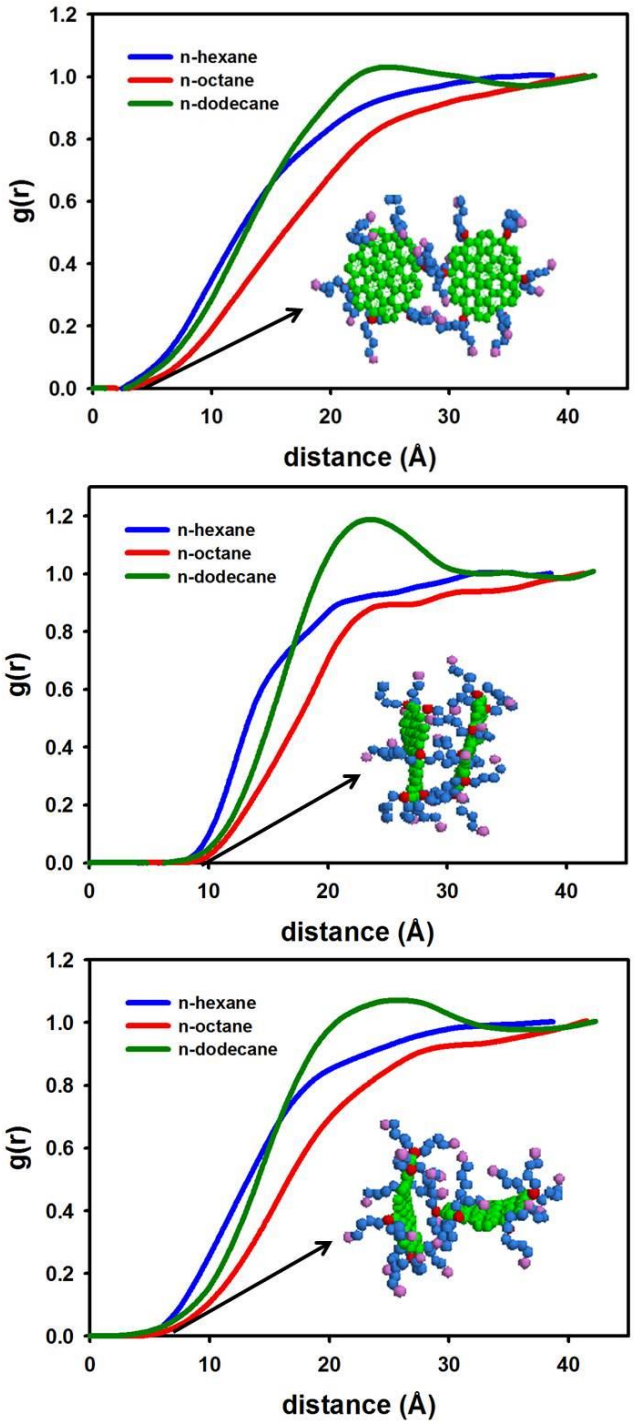

Figure 2-9 Edge-edge (top), ring-ring (center), and ring-edge (bottom) RDFs calculated for GS of 54 carbon atoms functionalized with 6 branched alkanes of 11 carbon atoms each dispersed in n-hexane (blue line), n-octane (red line) and n-dodecane (green line). The insets are representative snapshots observed at the minimum distance at which the RDFs are nonzero. All simulations were conducted at 300K.

The snapshots shown as inset in Fig 2.9 are representative of the configurations observed at the minimum distance d at which the corresponding RDFs are larger than zero. The edge-edge RDFs (top panel) is nonzero at d ~ 4Å. Correspondingly, two approaching GS are parallel and belong, approximately, to the same plane, as shown by the snapshot. The ring-ring RDFs (center panel) is nonzero at d ~ 10Å, at which separation the interacting GS are parallel, but belong to different planes. It is clear, from visual inspection of simulation snapshots and from the contour plots shown in Fig 2.6, how the branched functionalities provide the effective GS-GS repulsion when two GS adopt this configuration. Linear functionalities are not effective, and therefore the GS agglomerate as discussed in Fig 2.2. The ring-edge RDFs (bottom panel) are nonzero at d ~ 6Å, in correspondence of which separation one GS is perpendicular to the second one, as shown in the inset.

2.2.4 Graphene – Octane Radial Distribution Function

So far we demonstrated how it is possible to prepare stable dispersions of small GS in n-hexane, n-octane and n-dodecane. For many applications (e.g., to produce thermally-conductive lubricants), it is of interest to understand how the organic oils couple with the GS fillers. To evaluate this property, we calculated RDFs between the carbon atoms at the GS edges as well as those within the central GS ring, and methyl or methylene groups of the oils. The results are shown in Fig 2.10 where we consider GS of 54 carbon atoms functionalized with 6 branched alkanes of 11 carbon atoms each in n-hexane (blue lines), n-octane (red lines), and n-dodecane (green lines) at 300K.

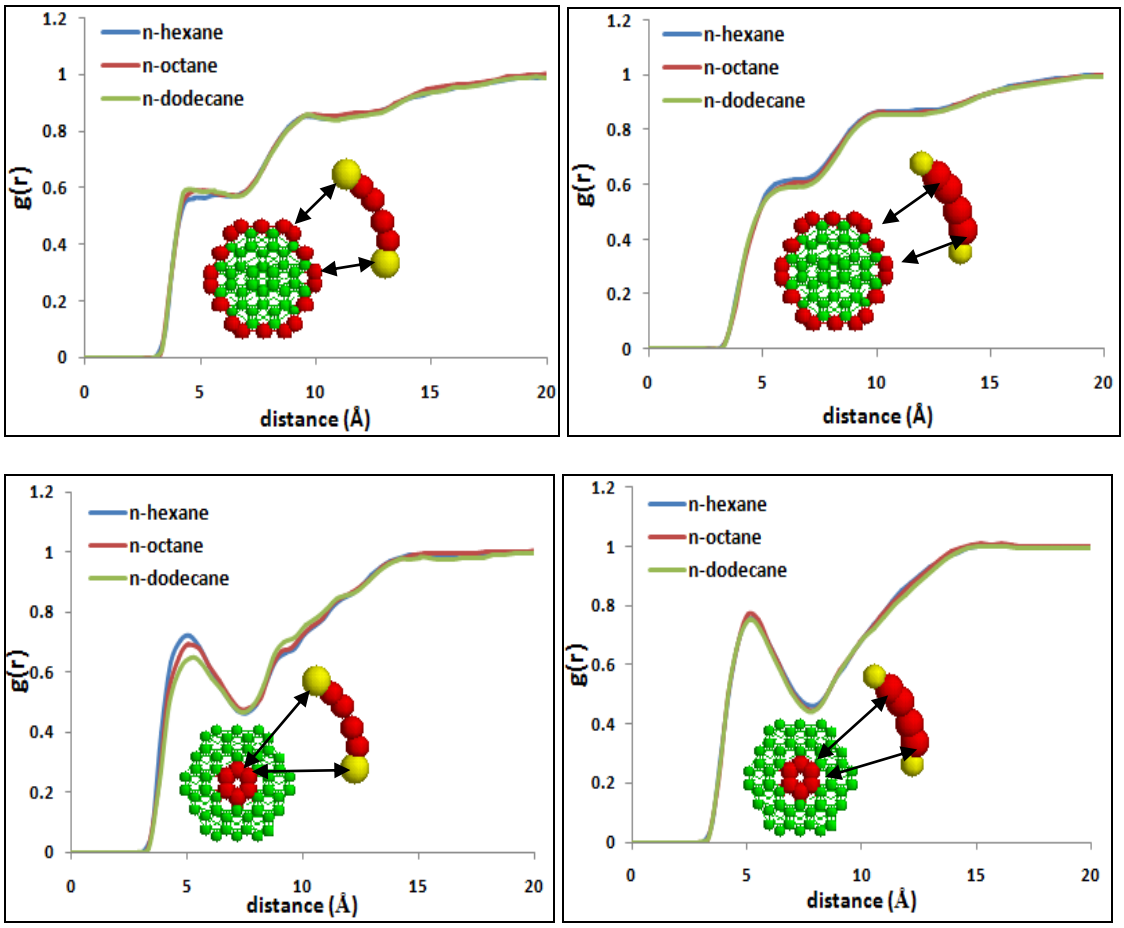

Figure 2-10 Radial distribution functions computed between the edge carbon atoms (top) and central ring carbon atoms (bottom) of GS of 54 carbon atoms functionalized with 6 branched alkanes of 11 carbon atoms each (see Fig 2.1c) and methyl (left panel) or methylene (right panel) groups of n-hexane (blue lines), n-octane (red lines) and n-dodecane (green lines). The insets are schematics that highlight the atoms considered for each RDF calculation. All simulations were conducted at 300K.

The results in Fig 2.10 suggest that, limited to the linear solvents considered here, oil packing on the GS does not depend on the oil molecular weight. The position of the first peak (~ 5Å) is due to excluded-volume effects and corresponds to ~1/2 the sum of carbon atoms and methyl or methylene groups' diameters. In all cases the first peak intensity is less than unity, suggesting that, because of excluded-volume effects, the solvent molecules are not preferentially at contact with the GS. We found it interesting

that both the CH_3 and the CH_2 groups of the oils are more likely to be in contact with the central GS carbon ring than with the GS edge atoms. These data suggest that the oil molecules are more likely to lay flat on the GS, because of entropic reasons. It is possible that the functional groups at the GS edges affect this preferential orientation.

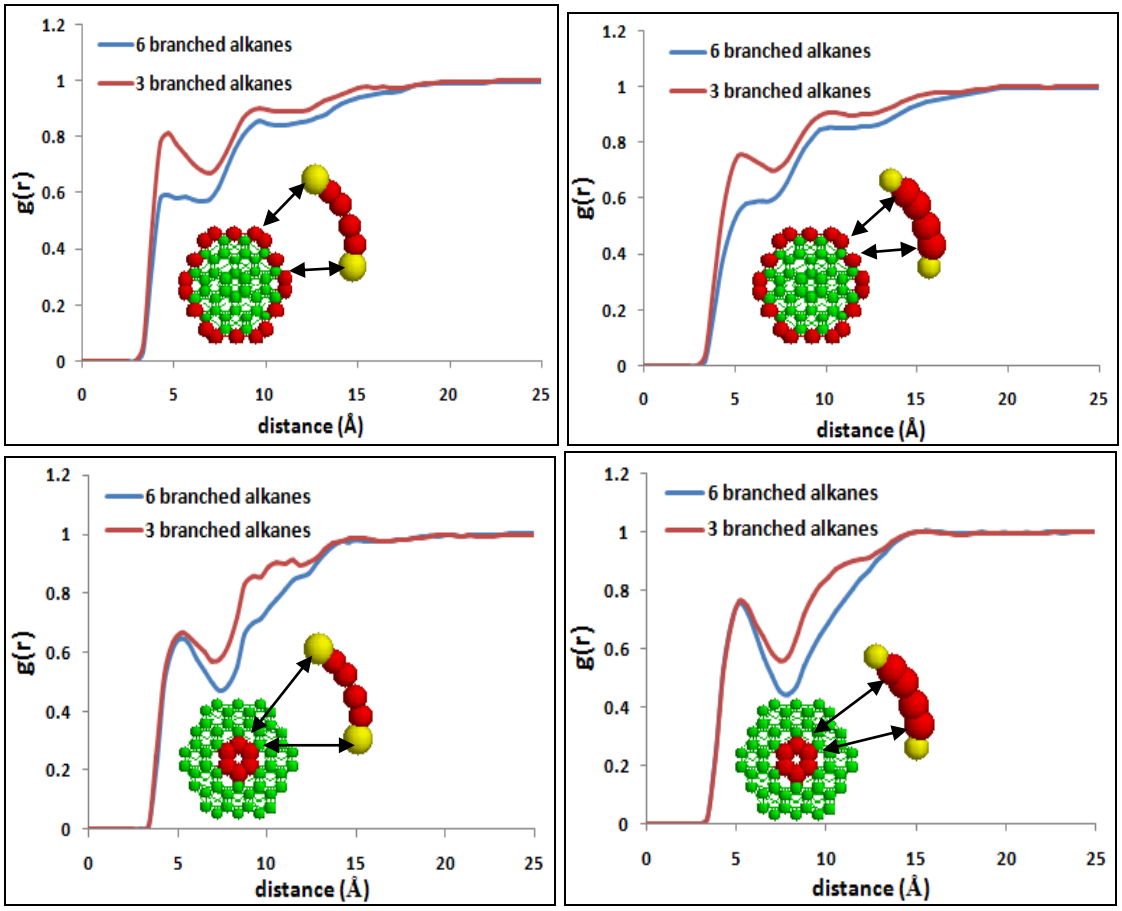

Figure 2-11 Radial distribution functions computed between the edge carbon atoms (top) and central ring carbon atoms (bottom) of five GS of 54 carbon atoms functionalized with six branched alkanes of 11 carbon atoms each (blue lines) and three branched alkanes (red lines) each and methyl (left) or methylene (right) groups of n-dodecane. The insets are schematics that highlight the atoms considered for each RDF calculation. All simulations were conducted at 300K.

To test this possibility, in Fig 2.11 we report oil-GS RDFs for GS of 54 carbon atoms functionalized with either six or three branched alkanes of 11 carbon atoms each in n-

dodecane at 300K. The results suggest that, although oil packing around the functionalized GS is similar in the two cases (i.e., the peaks positions do not depend on the number of functional groups grafted to the GS), the RDFs at close separation are always more intense when the GS are functionalized with fewer branched alkanes. Clearly, increasing the number of functional groups on the GS edges decreases the likelihood of oil packing. Thus when enhanced coupling between the organic matrix and the GS fillers is required (*e.g.*, to produce thermally-conductive composites), it is important to minimize the number of functional groups per graphene sheet.

2.3 Conclusions

In conclusion, in this Chapter we reported equilibrium molecular dynamics simulations for pristine and functionalized graphene nanosheets of either 54 or 96 carbon atoms each dispersed in liquid n-hexane, n-octane, and n-dodecane at 300K. We demonstrated that by functionalizing six equally spaced edge carbon atoms in each graphene sheet with branched alkanes it is possible to prevent the graphene sheets agglomeration. Careful analysis of the simulation results demonstrates that the stabilization is provided by excluded-volume effects. Linear functional groups grafted to the GS edges are not effective because the excluded-volume that they generate is not symmetric with respect to the plane identified by one GS. In addition, we characterized the preferential orientation of approaching graphene sheets in the three organic solvents. We also studied the packing of the organic oils on the graphene sheets by computing appropriate site-site radial distribution functions. The results suggest that the organic oils tend to lay flat on the graphene sheets. Consequently, the branched functionalities that are effective

in preventing the graphene sheets aggregation also repel, to some extent, the organic oils. Our results imply that in those applications that require strong coupling between the organic matrix and the graphene sheets used as fillers (e.g., thermally-conductive lubricants) it is desirable to minimize the number of branched functional groups used per graphene sheet, unless the functional groups themselves aid the coupling between the GS and the surrounding matrix, as was observed, for example, in the case of carbon nanotubes in n-octane.[102]

3. Thermal Boundary Resistance at the Graphene – Oil Interface

The material presented below was published in 2009 in volume 95, issue 16, and page 163105 of the AIP journal Applied Physics Letters.

3.1 Introduction

Producing nanocomposite materials that take advantage of the mechanical properties of an organic matrix (*e.g.*, a polymer) and the exceptional heat-transfer properties of nanoparticles (*e.g.*, carbon nanotubes or graphene sheets (GS)) has been elusive so far because of the large resistance that heat encounters upon transferring from the nanoparticle to the organic matrix (*i.e.*, the Kapitza resistance). For example, carbon nanotubes (CNT), because of their exceptional intrinsic thermal transport properties[98-99] coupled to their percolation thresholds even below 1% by volume, stimulated a wealth of enthusiasm.[100] Unfortunately, experimental measurements showed only modest increases in the composite thermal conductivity with respect to the thermal conductivity of the pure matrix material.[100-101] This is because of the poor coupling between the vibrational modes in the CNT and the surrounding matrix.[104] The resistance to heat flow at the interface, the Kapitza resistance,[105] is associated with differences in the phonon spectra, and weak contacts, between filler and matrix.[102, 106]

The latest carbon-based nanomaterials that are attracting wide interest are GS.[4,5] For the purposes of manufacturing composites with high thermal-transport properties it is important to point out that recent experimental results show GS thermal conductivities 50% in excess of those reported for CNT.[62,202] Hu *et al.*,[63] conducting all-atom

molecular dynamics simulations, predicted thermal conductivity for graphene nanoribbons comparable to that found experimentally, and showed that it strongly depends on the structure of the GS edges, as well as on the presence of defects. Although these results are very encouraging for the manufacture of GS – based composites, it is necessary that the Kapitza resistance does not compromise the macroscopic composite properties. The scope of this Chapter is to assess the Kapitza resistance in GS – oil nanocomposites and to compare it to results available for CNT – based composites. Our all atom molecular dynamics simulation results show that pristine GS have lower Kapitza resistance compared to CNT, but that the Kapitza resistance increases as the GS size increases. More importantly, we prove that by functionalizing the GS with short branched alkanes the Kapitza resistance decreases significantly because the vibrational modes of the functional groups couple with those of the surrounding oils.

3.2 Simulation Details

The implemented simulation protocol is described by Shenogin *et al.*,[102] and details about the force fields employed can be found in our earlier report.[203] In short, we place one GS at the center of a cubic simulation box filled with liquid octane. We conduct MD simulations to equilibrate the system 300K. At this point we instantaneously increase the GS temperature to 500K. As the simulation progresses at constant system energy the GS temperature decreases and the oil temperature increases. We monitor the difference in temperature between the GS and the surrounding oil over time. Fitting the observed decay in the temperature difference with an exponential function

($\Delta T(t) = \Delta T(t=0) \cdot e^{-t/\tau}$) we extract the time constant τ, which is related to the Kapitza resistance K via:[102]

$$K = \frac{A \cdot \tau}{C} \tag{3.1}$$

In Equation (3.1) A is the interfacial area across which heat transfers from the GS to the surrounding liquid octane and C is the GS heat capacity.

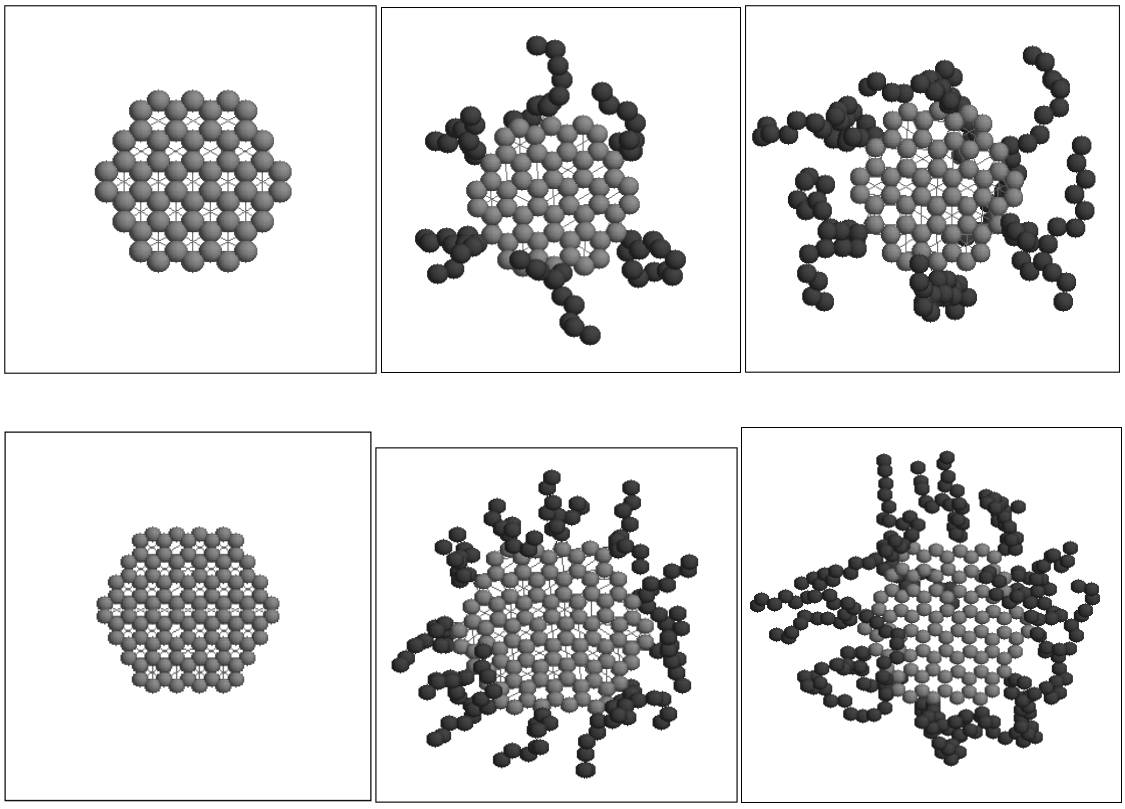

Figure 3-1 Schematic for one pristine GS of 54 atoms (left), one GS of 54 atoms functionalized with 6 short branched alkanes (middle), and one GS of 54 atoms functionalized with 6 long branched alkanes (right).

Several GS were considered, some of which are shown in Fig 3.1. From left to right these are one 'pristine' (*i.e.*, not functionalized) GS, one GS functionalized with 'short' functional groups, and one GS functionalized with 'long' functional groups. Short and

long functional groups are alkanes with 11 and 21 carbon atoms, respectively. In Fig. 3.2 we show on the left one representative simulation snapshot for the system containing one pristine GS (with 54 carbon atoms) and 240 octane molecules, and on the right one representative simulation snapshot for one functionalized GS in octane. The GS shape is approximately hexagonal to mimic experimental systems.[24] The number of functional groups is the minimum required to stabilize the GS-oil dispersions based on our previous simulations.[203] As in our previous work,[203] the functional groups are equally spaced along the GS edges.

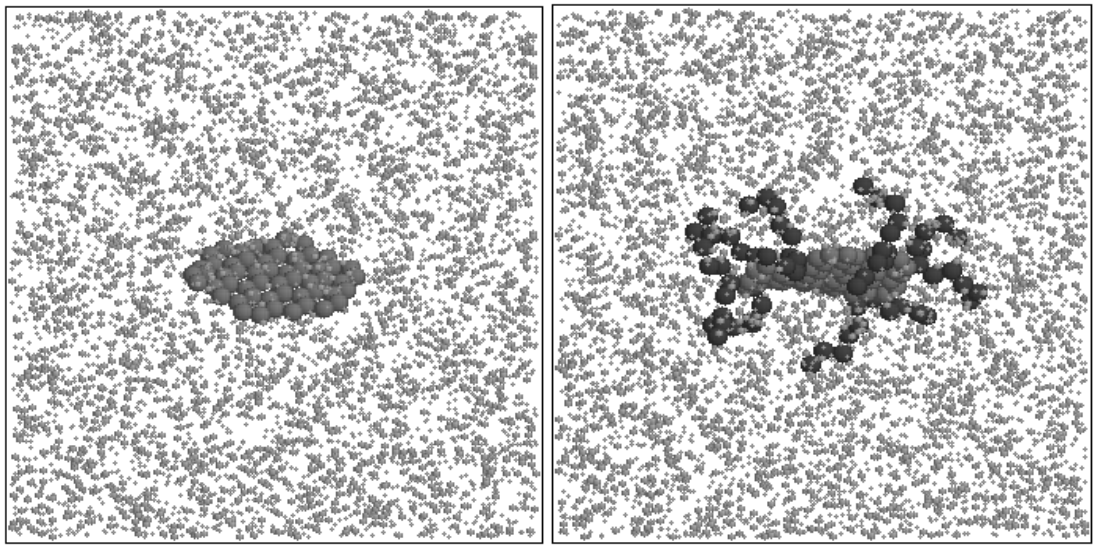

Figure 3-2 Representative simulation snapshot of GS of 54 atoms dispersed in octane when it is pristine (left) and functionalized with 6 short branched alkanes (right).

To conduct our simulations we employed the package LAMMPS.[193-194] All results were obtained using equilibrium molecular dynamics (MD) simulations within the NVT and NPT ensembles and non-equilibrium molecular dynamics (NEMD) simulations in the NVE ensemble. In the NVT ensemble the number of particles (N), the simulation box volume (V), and the temperature (T) are maintained constant. In the NPT ensemble the

system volume is allowed to fluctuate to maintain the pressure (P) constant. In the NVE ensemble, the simulation box volume (V), and the energy of the system (E) are maintained constant. Periodic boundary conditions were applied in all the three dimensions. The size of the simulation box was approximately 45×45×45 Å in all the systems considered. In all cases the time step was of 0.05 fs.

Each GS was composed of either 54, 96 or 216 carbon atoms. The Tersoff force field[195-197] was employed to describe the interactions among these atoms. In the Tersoff force field, the potential energy is modeled as a sum of pair like interactions, where, however, the coefficient of the attractive term in the pair like potential depends on the local environment, yielding an effective many-body potential. Interactions between carbon atoms belonging to different GS were described using Lennard-Jones potentials. To describe octane we implemented the all atom approach and the parameters were taken from the OPLS-AA force field.[204] In the OPLS-AA force field, the non-bonded potential between interaction sites, which are separated by more than three bonds or belong to different molecules, is described by the Lennard-Jones 12-6 potential. The interactions between GS and octane were described by the 12-6 Lennard-Jones (LJ) potential. The parameters were obtained by Lorentz-Berthelot rules[137] from those of the pure compounds. In case of functionalized GS, the short branched alkane consisted of 11 atoms and long branched alkane consisted of 21 atoms.

In each simulation box the number of octane molecules ranged from 240 to 900 depending on the size of the GS and that of GS was 1. In the initial configuration all these molecules were disposed in a lattice within the simulation box. To prevent excessive forces, the MD simulations, carried out in the NVT ensemble, where initially

conducted at very low temperatures (50K). The system was then heated from 50K to 300K at the heating rate of 100K every 300ps of simulation. The system was then equilibrated in the NPT ensemble at 300K and 1 bar to stabilize the system volume. Once the simulation box volume fluctuated around a constant value, simulations were conducted in the NVE ensemble at 300 K. Then the configurations were collected every 50 ps, and the temperature of the GS was instantaneously increased to 500K. Then the simulations were conducted in the NVE ensemble for 100 ps for each system.

The heat capacity of the nanoparticle was calculated using the formula

$$C = \frac{< u^2 > - < u >^2}{K_B T^2}$$

Where u is the total energy of the system, K_B is the Boltzmann constant, and T is the temperature of the system.

The nanoparticle was simulated in the NVT ensemble at 500K for 20 ns and the total energy was used to calculate the heat capacity.

In order to calculate the fourier transform of the velocity autocorrelation function, we simulated the system of GS and octane in the NVT ensemble. From the velocities of carbon atoms in the GS and octane, we calculated the velocity autocorrelation function which was then used to calculate the fourier transform.

3.3 Results and Discussion

3.3.1 Comparison of Kapitza Resistance between Graphene Sheets and Carbon Nanotubes

The first comparison necessary for the production of GS – based composites with high thermal transport properties consists in evaluating the Kapitza resistance for pristine GS vs. that for CNT. In Fig. 3.3 we compare the decay in temperature difference between one nanoparticle and the surrounding octane as a function of time when the nanoparticle is one (5,5) single walled CNT, or one pristine GS with 54 or 216 carbon atoms. We point out that the temperature decay obtained for the (5,5) CNT is equivalent to that reported by Shenogin *et al.*[102] Visual observation reveals that the difference in temperature between the nanoparticle and the surrounding oil decays faster for the GS than for the CNT. Using Eq. (1), we found that the Kapitza resistance is the smallest for the GS with 54 carbon atoms, and the largest (by a factor of ~4) for the CNT. However, the results, reported in Table 3.1, show that the Kapitza resistance for GS increases as the size of the GS increases. This result, clearly not encouraging for practical applications, is due to the fact that as the GS size decreases, the GS becomes more and more similar to the oil molecules, and therefore the thermal vibration modes of the small GS become compatible with those of the solvent.

Table 3-1 Simulated Kapitza resistances K for the systems considered in this work. FG stands for functional groups. We also report the average decay constant τ (see Eq. (1)) and other simulation details such as the dimension of the cubic simulation box and the number of octane molecules considered for each system.

Nanoparticle	Simulation box size ($Å^3$)	Octane molecules	τ (ps)	K ($\times 10^{-8}$ Km^2W^{-1})
CNT 560	40×40×60	346	60.7±7.6	4.2±0.6
GS 54	40×40×40	240	30.3±7.8	1.3±0.3
GS 54 (6 short FG)	40×40×40	240	10.0±4.0	0.42±0.16
GS 54 (6 long FG)	40×40×40	240	8.8±3.6	0.37±0.15
GS 96	55×55×55	600	29.3±7.5	3.17±0.72
GS 96 (12 short FG)	55×55×55	600	14.1±3.9	1.54±0.38
GS 96 (12 long FG)	55×55×55	600	14.0±3.3	1.5±0.3
GS 216	65×65×65	900	30.6±8.2	4.0±1.0
GS 216 (18 short FG)	65×65×65	900	15.6±4.1	2.0±0.5
GS 216 (18 long FG)	65×65×65	900	15.5±3.4	2.0±0.4

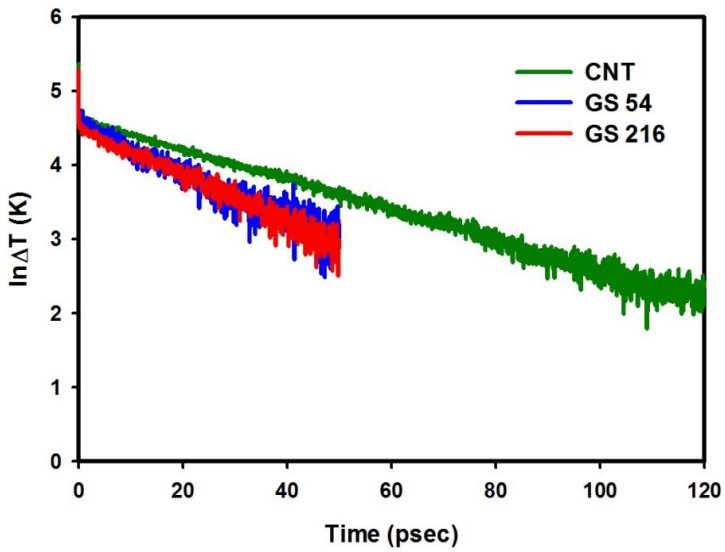

Figure 3-3 Difference in temperature (ΔT) between one nanoparticle and the surrounding liquid octane as a function of time. Results are shown for three independent systems, in which the nanoparticle is either one (5,5) single walled CNT (green line), or one pristine GS with 54 (blue line) or 216 carbon atoms (red line).

3.3.2 Temperature Profile

In Fig. 3.4, we compare the decay in temperature difference between GS and liquid octane when the GS are either pristine or functionalized with branched alkanes. We only consider branched alkanes because our previous results indicate that these are the most effective in stabilizing GS dispersions in oils.[203] Visual observation reveals that heat transfers more easily across the GS-oil interface when the functional groups are present than when they are not. The Kapitza resistance, see Table 3.1, indeed decreases by a factor of ~3 in the presence of the functional groups. Unexpectedly, the length of the functional groups does not seem to affect the Kapitza resistance. Similar results have been obtained for GS of different sizes, suggesting that the observed behavior is general for the nanocomposites considered herein. Qualitatively, our results suggest that the vibrational modes of the nanoparticle couple well with those of the solvent once the

GS are functionalized. When the GS is functionalized with branched alkanes, the heat transfers parallel to the plane identified by the GS, i.e., the GS temperature drop is due to the functionalities attached on the edges. As soon as the GS thermal energy reaches the functional groups, it dissipates into the surrounding oil. Since the branched functionalities are of the same chemical nature as the surrounding oil, the length of the functional groups does not affect the results.

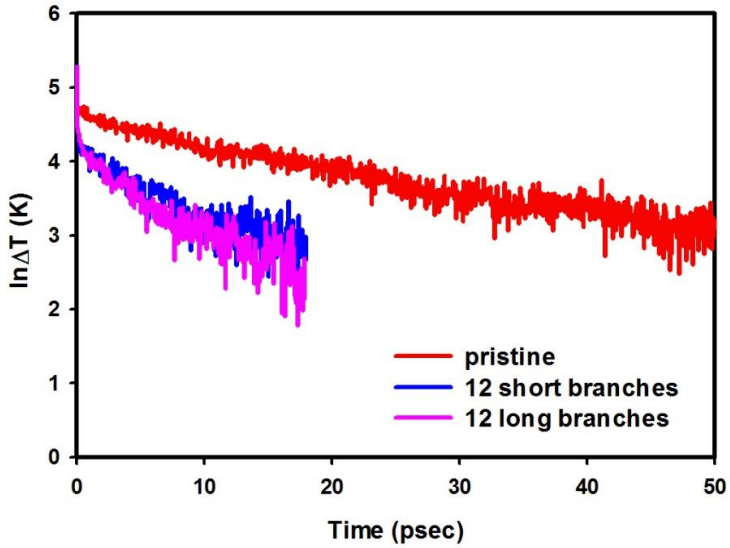

Figure 3-4 Difference in temperature (ΔT) between one nanoparticle and the surrounding liquid octane as a function of time. Results are shown for three independent systems, in which the nanoparticle is either one pristine GS of 96 atoms (pristine, red), one GS of 96 atoms functionalized with 12 short branched alkanes (12 short branches, blue), or one GS of 96 atoms functionalized with 12 long branched alkanes (12 long branches, purple).

3.3.3 Fourier Transform

To assess the likelihood of the latter interpretation, we computed the Fourier transform of the velocity autocorrelation function for carbon atoms in the octane solvent, for the carbon atoms in CNT, and those in pristine and functionalized GS. The results are shown in Fig 3.5. When we compare the data obtained for CNT and octane (top panel),

it is clear that the phonon spectra do not overlap, which is the reason for the poor thermal coupling between CNT and organic materials.[102-103] When we compare the data for pristine GS and octane (middle panel), our results are qualitatively similar to those obtained for CNT-oil systems. Namely, the phonon spectra of the two materials do not couple. However, when we compare the results obtained for functionalized GS to those obtained for octane (bottom panel) our data reveal that the phonon spectra overlap quite nicely on a few frequencies. In the figure we highlight the corresponding overlap frequencies with arrows. These overlaps are responsible for the decreased Kapitza resistance predicted by our simulations in the case of functionalized GS dispersed in octane compared to all the other systems tested. For completeness, it should be pointed out that even in the case of CNT – oil dispersions it has been predicted that by functionalizing the CNT reduces the Kapitza resistance.[147] However, when CNT are functionalized they tend to lose their exceptional intrinsic properties. On the contrary, by functionalizing the GS on their edges it is unlikely that the exceptional intrinsic thermal conductive properties reported are going to be significantly affected, at least for sufficiently large GS. The recent simulation results reported by Hu *et al*.[63] could be used to design GS with functional groups grafted in the most convenient sites to improve macroscopic heat-transfer properties.

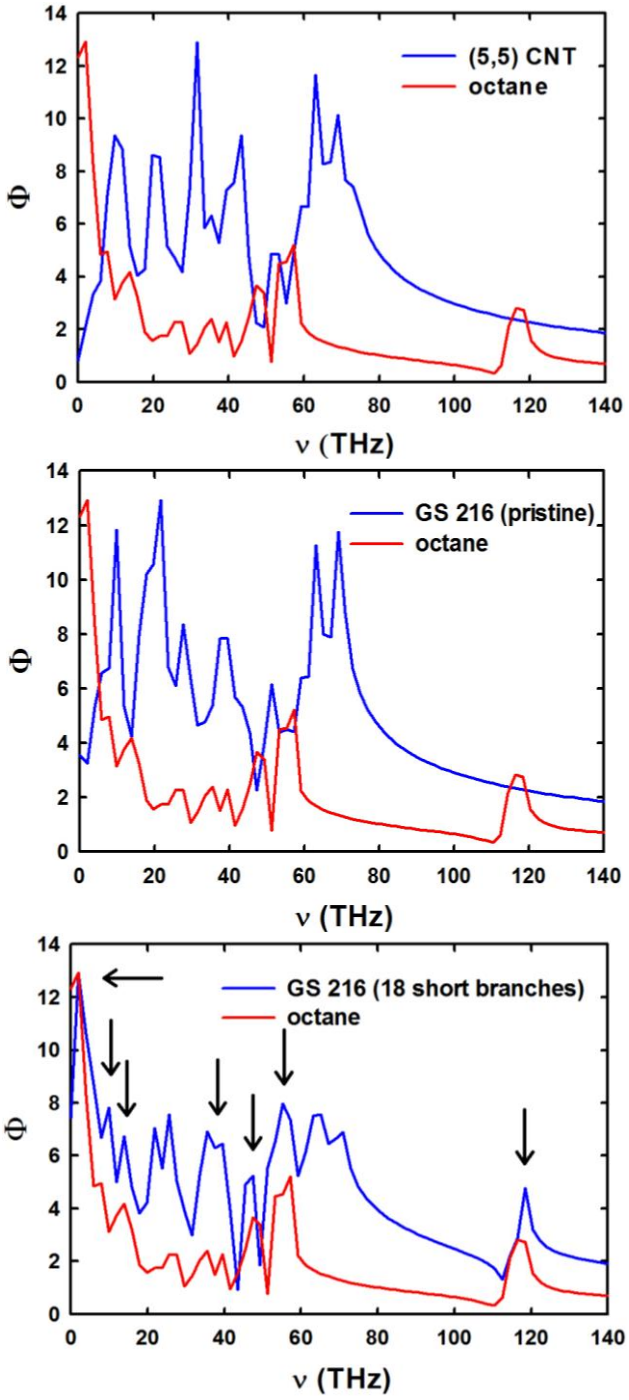

Figure 3-5 Fourier transform of the velocity autocorrelation function for carbon atoms in octane (red in all panels) and three representative nanoparticles. Nanoparticles considered are (5,5) single walled carbon nanotubes (blue, top panel), pristine GS of 216 atoms (blue, middle panel), and GS of 216 atoms functionalized with 18 short branched alkanes (blue, bottom panel). The arrows in the bottom panel highlight those GS vibrational frequencies that overlap with those of octane, lowering the Kapitza resistance.

3.4 Comparison to Other Interfaces

It is of interest to compare the values for the Kapitza resistance at GS-octane interface to those reported in the literature for other GS-matrix interfaces. Table 3.2 summarizes the Kapitza resistance (K) values obtained at various GS-matrix interfaces. It is of particular interest to compare our values of Kapitza resistance to those obtained by Shangchao et al.[205], who calculated the thermal boundary conductance at the GS-octane and functionalized GS (alkyl pyrene linkers)-octane interfaces using the Muller-Plathe method.[206] The inverse of the thermal boundary conductance i.e., the Kapitza resistance was calculated to compare to our calculated Kapitza resistance values at the GS-octane interface. Unlike the method we used to calculate the Kapitza resistance (equilibrating the system of GS and octane at 300K, then heating the GS to 500K and using the temperature decay of the GS to calculate the Kapitza resistance), Shangchao et al.[205] equilibrated the system of GS and octane at 300K, then heated the octane to 500K and used the temperature decay of the octane to calculate the thermal boundary conductance. The results indicate that the Kapitza resistance at the GS-octane interface obtained by Shangchao et al,[205] 1.09×10^{-8} Km^2W^{-1} is slightly lower than our calculated value, $1.3 – 4.0 \times 10^{-8}$ Km^2W^{-1}. Shangchao et al.[207] also calculated the Kapitza resistance between GS functionalized with alkyl pyrene linkers and octane. This value ($0.83 – 1.09 \times 10^{-8}$ Km^2W^{-1}) compares well with that of our value of Kapitza resistance between GS functionalized with branched alkanes and octane ($0.37 – 2.00 \times 10^{-8}$ Km^2W^{-1}). Also, our values of Kapitza resistance at the GS-octane interface are in good agreement with those calculated at GS-polyethylene,[208] GS-phenolic resin,[209] GS-paraffin wax,[210] and GS-epoxy[211] interfaces. Wang et al. predicted the thermal boundary

conductance at the GS-polyethylene interface by functionalizing the surface of the GS with two linear hydrocarbon chains (C_nH_{2n+1}, n=15). They observed that as the number of hydrocarbon chains grafted to the GS was increased from 0 to 9, the thermal boundary conductance increased from 76.5 MW/m^{2}K to 250 MW/m^{2}K. They attribute this increase to the enhanced coupling between GS and polyethylene when the GS is functionalized with hydrocarbon chains, which is consistent with what we observed when the GS is functionalized with alkane chains. The calculated Kapitza resistance value (inverse of the thermal boundary conductance), 0.40 – 1.00 × 10^{-8} Km^{2}W^{-1} compares well with that we obtained at alkane chain functionalized GS-octane interface, 0.37 – 2.00 × 10^{-8} Km^{2}W^{-1}.

Table 3-2 Comparison of Kapitza resistance (K) between various interfaces. FGS stands for functionalized GS.

Interface	**K (× 10^{-8} Km^{2}W^{-1})**	**Authors**
GS – octane	1.3 – 4.0 (heating GS)	Our work
GS – octane	1.09 (heating matrix)	Shangchao et al.[205]
FGS – octane (branched alkanes)	0.37 – 2.00 (heating GS)	Our work
FGS – octane (alkyl pyrene linkers)	0.83 – 1.09 (heating matrix)	Shangchao et al.[205]
GS – polyethylene	1.30 (heating matrix)	Wang et al.[212]
FGS – polyethylene (hydrocarbon chains)	0.40 – 1.00 (heating matrix)	Wang et al.[212]
GS – phenolic resin	5.0 (heating GS) 1.25 (heating matrix)	Hu et al.[213]
GS – paraffin wax	1.40 – 1.63	Luo et al.[214]
GS – epoxy	3.12 – 10.00 (heating GS)	Mortazavi et al.[215]

3.5 Conclusions

Concluding, our simulations predict that the heat transfer between small GS and octane is not affected by large Kapitza resistances. However, limited to the GS considered herein, the resistance increases as the GS size increases, and approaches the values reported for (5,5) CNT-octane systems when GS of 216 atoms are considered. More interestingly, we found that functionalizing the GS edges with branched alkanes not only stabilizes GS dispersions in oils,[203] but also reduces the Kapitza resistance in general by a factor of 3, which renders these nanoparticles optimal candidates for the production of composite materials with enhanced thermal transport properties. Our results indicate that for these materials to be effective it is necessary that the vibrational modes of the functionalized GS couple with those of the organic matrix. This observation is useful for designing appropriate functional groups to improve the macroscopic heat transfer properties.[216] Furthermore, because functionalized GS resemble discoid molecules, it is likely that nematic phases appear as the GS concentration increases in nanocomposites.[217,218] Thus, by combining the exceptional heat transfer properties of individual GS, the reduced Kapitza resistance predicted by the present work, and the appearance of nematic phases, it will be possible to produce nanocomposite materials with anisotropic heat transfer properties.

4 Thermal Boundary Resistance at the Graphene-Graphene Interface Estimated by Molecular Dynamics Simulations

The material presented below was published in 2012 in volume 527, issue 6, and page 47 of the Elsevier journal Chemical Physics Letters.

4.1 Introduction

The enormous amount of research attention toward GS has raised expectations for new microscale and nanoscale applications. In Chapter 2, we have shown a mechanism to obtain stable dispersions of GS in oils by functionalizing the GS edges with branched alkanes. For practical thermal management applications, it is of great importance to completely characterize the thermal properties of systems containing GS. Balandin *et al*.[62] measured the intrinsic thermal conductivity of individual GS, ~ $5.1\pm0.7\times10^{3}$W/mK, in agreement with the simulations reported by Hu *et al*.[63] Other measurements for thermal conductivity of GS have been reported, for example by Cai et al.[64] and Faugeras et al.[65] who observed that the thermal conductivity of supported GS is smaller than suspended GS. To ensure effective heat transfer, future GS-based systems will require good thermal transfer between GS and polymeric matrix materials. Both experiments and simulations have investigated the Kapitza resistance between CNT contacts and found that the resistance at the CNT-CNT interface[139-144] is larger compared to that of the CNT-matrix interface when the matrix is octane,[102-103] epoxy,[145] an aqueous suspension,[146] etc.[147] For GS-based nanocomposites, Chen *et al*[219] demonstrated through experiments that the Kapitza resistance at GS-SiO_2 interface is 0.5 - 1.2 × 10^{-8} Km^2W^{-1}. From our earlier simulations of small GS in octane (Chapter

3),[220] we suggested that by functionalizing the GS edges it might be possible to reduce the Kapitza resistance because of the coupling of the vibrational modes of the functional groups with those of the organic matrix. Because when dispersed in a matrix GS tend to agglomerate, and because GS agglomeration increases with GS volume fraction, it is important to estimate the Kapitza resistance at the GS-GS interface. If, as was observed for CNTs, the thermal boundary resistance at GS-GS junctions is larger than that at GS-matrix interfaces, it might be beneficial to minimize GS-GS contacts in designing thermally conductive composites. Clarifying this possibility is the scope of this Chapter.

4.2 Simulation Method

To conduct our all-atom molecular dynamics (MD) simulations we employed the simulation package LAMMPS.[193-194] The method implemented has been described in details in section 3.1 and it is based on non-equilibrium MD. We employed the protocol proposed by Shenogin et al.[102] We place the GS at the center of a cubic simulation box, either filled with liquid n-octane or empty. For GS in octane, the system is initially equilibrated within NVT and NPT ensembles. The system of GS in vacuum is equilibrated in the NVT ensemble. All results are then obtained using non-equilibrium MD within the NVE ensemble and 0.05 fs timestep. Periodic boundary conditions are applied in all three directions. The parameters to describe force fields and interactions between different groups/atoms are reported in Table 1.1. Each GS considered here contains 432 carbon atoms and 865 octane molecules are simulated as solvent.

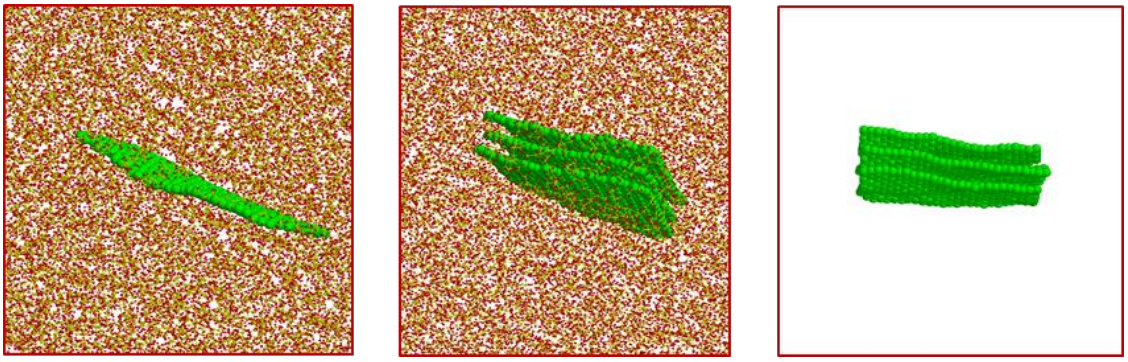

Figure 4-1 Representative simulation snapshots for the systems containing one GS in octane (left), three GS in octane (middle), three GS in vacuum (right).

We performed simulations of three GS in octane and in vacuum to calculate the Kapitza resistance at the GS-GS interface. At equilibrium the inter-layer distance between the GS was found to be 3.6 Å, larger than that observed in graphite. To compare the GS-GS Kapitza resistance to that of the GS-octane interface, we conducted simulations of one GS in octane. In Fig. 4.1 we show representative simulation snapshots for the systems containing one GS in octane (left), three GS in octane (middle), and three GS in vacuum (right). The initial configuration for the system with three GS in vacuum was prepared with an inter-layer distance of 10 Å. The temperature was increased slowly from 50 K to 300K in steps of 50K every 200 ps to avoid the appearance of defects or the breakage of GS. We then conducted MD simulations for approximately 2 ns to equilibrate the system at 300K. When three GS are considered (middle and right panels in Fig. 4.1), after equilibration we suddenly increased the central GS (CGS) temperature to 500K by rescaling the atomic velocities. The central GS was maintained at 500K for 0.5 ns while the rest of the system was not allowed to move. The system (CGS at 500K, surroundings at 300K) was then allowed to relax at constant energy without any heat sources, heat sinks, or thermostats (NVE ensemble). In the case of one GS in octane (left panel of Fig. 4.1), the GS is heated to 500K, kept at that temperature for 0.5 ns, and

then allowed to relax in the NVE ensemble. The results reported here are the averages of 50 independent simulations for each case.

During the NVE simulations the CGS/GS temperature decreases and the temperature of the surrounding GS (SGS), as well as that of octane, increase. We monitor the difference in temperature between the CGS/GS and the SGS/octane over time. The difference in temperature typically follows an exponential decay. Following prior works, we extract the time constant τ by fitting the observed decay with an exponential function ($\Delta T(t) = \Delta T(t=0) \cdot e^{-t/\tau}$). In a lumped capacitance model, the time constant is related to the Kapitza resistance R_k via:

$$R_k = \frac{A_T . \tau}{C_T} \tag{4.1}$$

In Eq. (4.1), A_T is the interfacial area across which heat transfers from the CGS/GS to the SGS/octane and C_T is the GS heat capacity, calculated via independent simulations for one GS in vacuum (~ 1.65×10^{-20} J/K at 500K).

Note that by applying Eq. (4.1) we reduce the simulated system to a two-body problem in which the heat transfer from the hot GS to the surrounding is assumed to be homogenous. The fact that the temperature difference between the hot GS and the surrounding follows an exponential decay qualitatively corroborates the validity of the model assumptions. However, Eq. (4.1) is expected to hold when the temperature of the surrounding system does not increase significantly during the NVE portion of the simulation. Although this might not be the case when three GS are simulated in vacuum, an estimate of the ratio between heat transfer resistances inside of and at the

surface of the system, i.e., the Biot number, provides a criterion for determining the applicability of lumped capacitance models. For those macroscopic systems in which the internal resistance to heat transfer is negligible, it has been determined that the error inherent in a lumped-parameter mathematical formulation is less than 5% when the Biot number is lower than 0.1.[221] Maruyama et al.[141] applied the Biot number criterion and calculated the Kapitza resistance at the CNT-CNT interface with the lumped capacitance model. Implementing the formulation proposed by Maruyama et al.,[141] the Biot number can be estimated at the GS-GS and at the GS-octane interface for the systems of interest here. Employing experimental data for the thermal conductivities of octane[222] and graphene[63] at 300 K, a characteristic length of 1.7 Å (half the LJ thickness of one grapheme sheet), and the inverse of the Kapitza resistances obtained herein, the two Biot numbers are estimated to be ~ 1×10^{-6} and 0.024, in both cases confirming that the lumped capacitance model still remains applicable.

4.3 Results and Discussion

4.3.1 Temperature Profile

In Fig 4.2, we compare the decay in temperature between one GS and the surrounding octane (blue line), between the CGS and the two SGS in octane (red line), between the CGS and the two SGS in vacuum (green line). Visual inspection reveals that the temperature difference decays faster for one GS in octane than for all other systems.

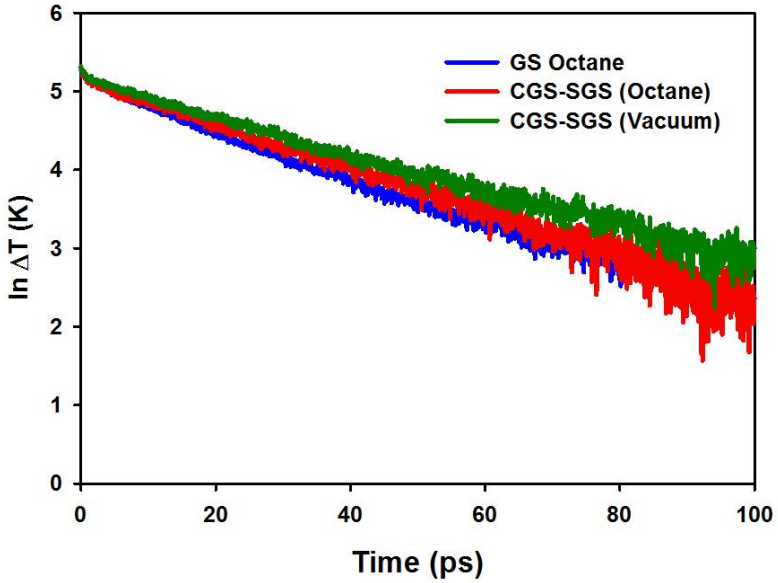

Figure 4-2 Logarithmic temperature difference between the heated graphene sheet and the surrounding system. The systems considered are one GS in octane (blue line), three GS in octane (red line) and three GS in vacuum (green line).

4.3.2 Kapitza Resistance

The values of τ and R_k for the different systems are summarized in Table 4.1. For the GS in octane the difference in temperature is between the GS and the surrounding alkanes. In the other two cases the difference is between the central GS (CGS) and the surrounding GS (SGS).

The Kapitza resistance calculated for the GS-GS interface is larger than that for the GS-octane interface, despite the fact that average GS-GS distances are lower than average GS-octane distances. This is because the separation distance between the CGS and SGS increases from 3.6 Å to 4.1 Å during the relaxation process, which indicates that there is an expansion of CGS due to heating. In the case of one GS in octane, the separation distance between GS and octane remained constant at 5.0 Å during the relaxation

process. So the observed expansion of CGS in the case of three GS in vacuum which is absent in the case of one GS in octane resulted in a higher value of Kapitza resistance observed at GS-GS interface compared to that at GS-octane interface. This result is consistent with that observed in the case of CNTs, i.e., the Kapitza resistance at the CNT-CNT interface is larger than that of CNT-octane interface. In the case of one GS in octane we found that functionalizing the GS could lead to lower Kapitza resistances,[220] but practical methods to reduce GS-GS, or CNT-CNT resistances remain elusive. We also find that the calculated GS-GS Kapitza resistance is higher than that of bulk graphite along the cross plane direction. This is consistent with prior observations, according to which the Kapitza resistance decreases as the number of layers in a graphene stack increases, reaching a value close to that characteristic of bulk graphite when the number of layers is 38 or greater.[223] It is possible that as the number of GS increases, the distance between them decreases, enabling more efficient thermal transport.

Table 4-1 Simulated Kapitza resistances for the systems considered in this work.

Nanoparticle	**τ (ps)**	R_k **(× 10^{-8} Km^2W^{-1})**
GS-octane	30.0±4.2	5.5±0.2
CGS-SGS (octane)	35.3±7.3	6.5±0.6
CGS-SGS (vacuum)	41.8±7.6	7.7±0.9

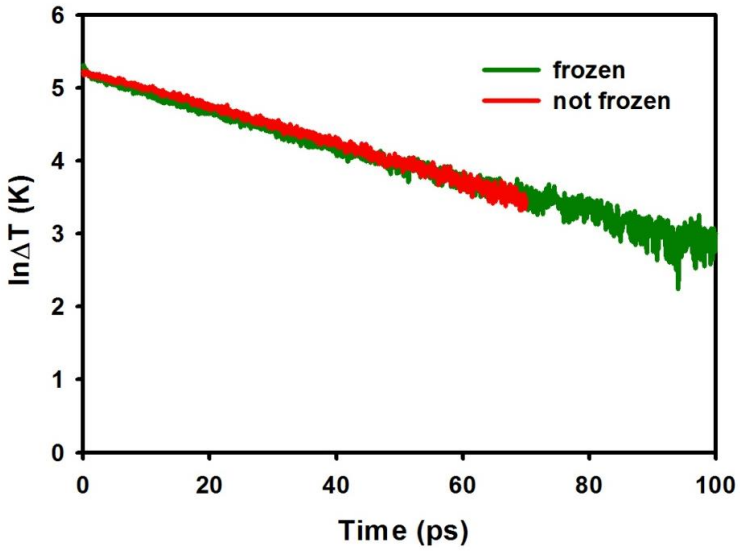

Figure 4-3 Logarithmic temperature difference between the central GS (CGS) and the surrounding GS (SGS) when the CGS was heated to 500K when SGS is frozen during thermal equilibration (green line) and not frozen (red line). In both cases the three GS are in vacuum.

As it is possible that freezing part of the system during equilibration might affect heat transfer between GS, additional simulations were conducted where three GS are simulated in vacuum. After equilibrating the GS at 300K, the CGS temperature was increased to 500K while the SGS was maintained at 300K during equilibration for 0.5 ns. The decay time constant obtained as a result of 30 additional simulations (42 ps) was found to be similar to that obtained when CGS was maintained at 500K while SGS was frozen during equilibration for 0.5 ns (43 ps) (The CGS-SGS temperature difference for the two cases during the NVE simulation phase is shown in Fig 4.3). As a result, the estimated Kapitza resistances are comparable. This provides evidence that there was no significant effect of freezing part of the system during equilibration on the heat transfer between GS.

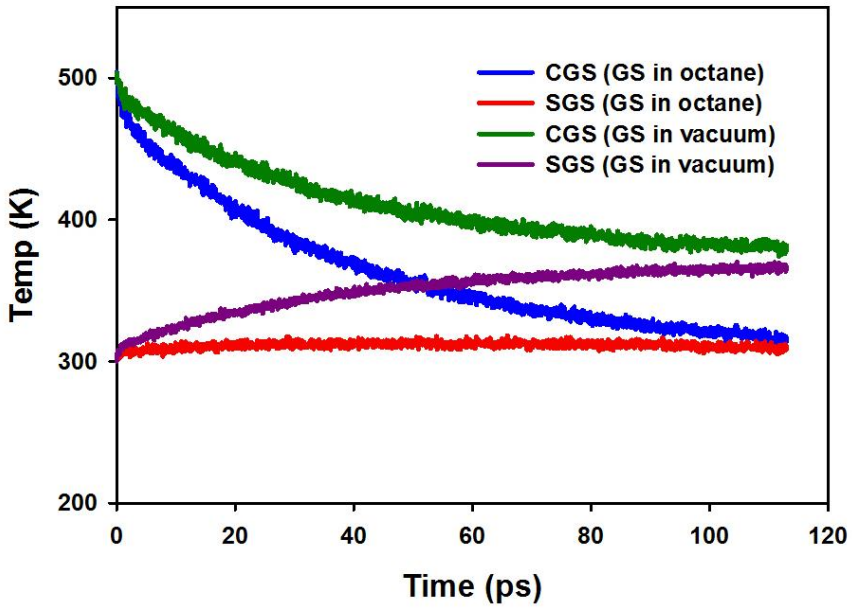

Figure 4-4 Temperature of CGS and SGS when three GS are in octane (blue and red lines) and when three GS are in vacuum (green and pink lines). CGS – central graphene sheet, SGS – surrounding graphene sheets.

We observe that the GS-GS Kapitza resistance is slightly larger when the GS are in vacuum compared to when the GS are in octane. When the GS are in octane, the two SGS can transfer heat to the surrounding octane. This phenomenon is evident from the temperature profile in Fig 4.4, where we plot the temperature of CGS and SGS over time. The temperature decay of the heated GS, the central one (CGS) is faster when the three GS are in octane (blue line) than when they are in vacuum (green line). The SGS temperature remains almost constant at ~305K when the three GS are in octane (red line) while it increases to 350K when the three GS are in vacuum (pink line). In the case of three GS in octane, both CGS-SGS and SGS-octane Kapitza resistances are present. However, no significant temperature difference is observed between SGS and octane during the NVE phase (both remain at ~ 300-305K), corroborating the validity of the lumped capacitance model of Eq. (4.1). Since the SGS-octane interface has a lower

Kapitza resistance than the CGS-SGS interface, heat dissipates quickly from the SGS to the surrounding octane.

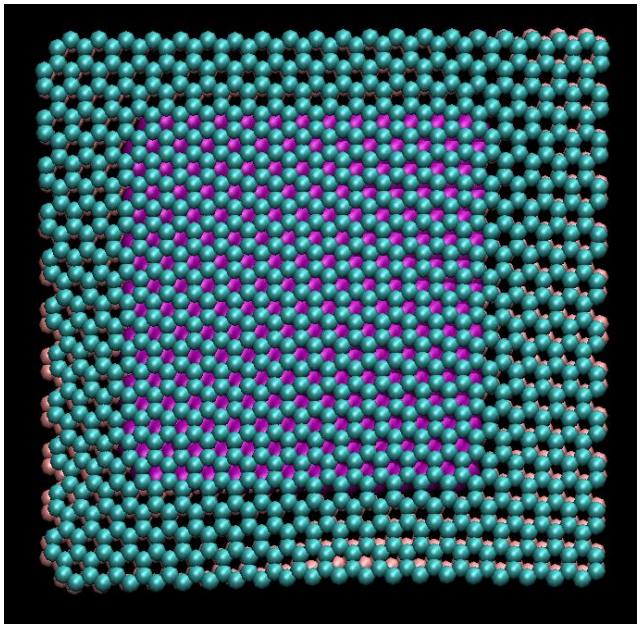

Figure 4-5 Representative simulation snapshot of three GS considered where SGS (cyan and orange spheres) size was increased to a size sufficient to prevent direct contacts between CGS (purple spheres) and octane. Octane is not shown for clarity.

As it is possible that heat transfers from the hot CGS to the surrounding octane via the graphene edges, rendering the heat-transfer problem more complex than assumed in Eq. (4.1), additional simulations were conducted in which the SGS size was increased in an amount sufficient to prevent direct contacts between CGS and octane. In these additional simulations the two SGS were rectangular of dimensions ~4.8 X 5.0 nm, while the CGS, also rectangular, had dimensions 2.8 X 3.0 nm. Representative simulation snapshot of the three GS is shown in Fig. 4.5. The increased size of the SGS prevented octane from being in direct contact with the heated CGS. The decay time

constant obtained as average of 25 additional simulations (37.0 ps) was found to be similar to that obtained when both SGS and CGS were of the same size (35.3 ps). As a consequence, the estimated Kapitza resistances are comparable (6.7×10^{-8} Km^2W^{-1} when the size of SGS was increased vs. 6.5×10^{-8} Km^2W^{-1} shown in Table 4.1). This precludes the possibility that heat transfers in a significant amount from the CGS directly to the surrounding octane via the GS edges. It is possible that small differences in the estimated values for the Kapitza resistances (6.7×10^{-8} vs. 6.5×10^{-8} Km^2W^{-1}) are due to differences in packing between the GS when the size of the SGS is increased compared to that of CGS.

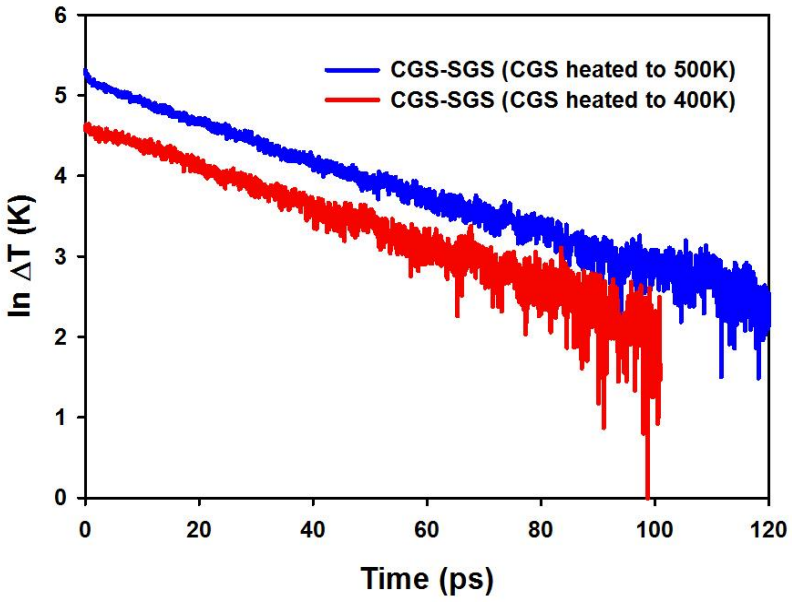

Figure 4-6 Logarithmic temperature difference between the central GS (CGS) and the surrounding GS (SGS) when the CGS was heated to 500K (blue line) or 400K (red line). In both cases the three GS are in vacuum.

To test the validity of the lumped capacitance model when three GS are in vacuum, additional simulations were conducted in which the CGS was heated from 300 to 400K,

instead of 500K. The CGS-SGS temperature difference for the two cases during the NVE simulation phase is shown in Fig. 4.6. Although the decay time constant is lower when CGS is heated to 400K ($\tau \sim 36.4$ ps) than when it is heated to 500 K ($\tau \sim 41.8$ ps), the calculated Kapitza resistances are similar (8.0×10^{-8} Km^2W^{-1} when CGS is heated to 400K vs. 7.9×10^{-8} Km^2W^{-1}) because the GS heat capacity is slightly lower at 400K ($\sim 1.37 \times 10^{-20}$ J/K) than at 500K ($\sim 1.65 \times 10^{-20}$ J/K).

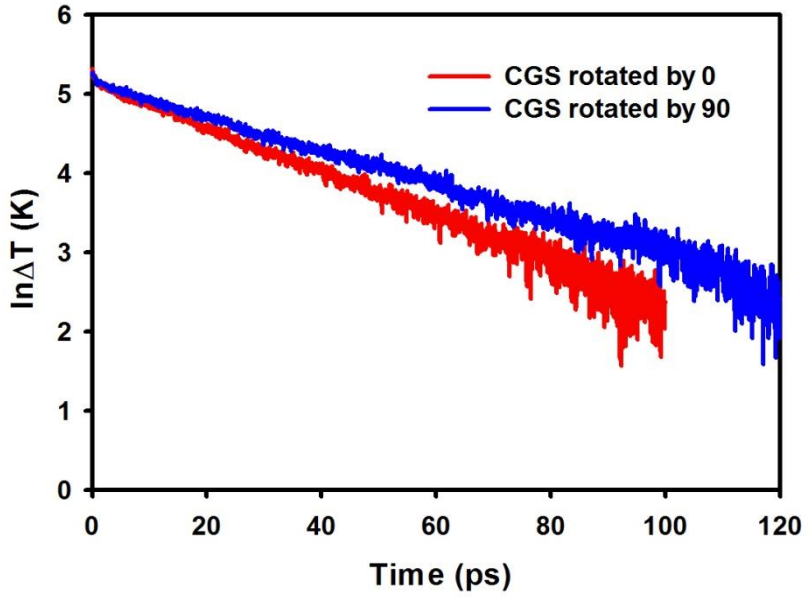

Figure 4-7 Logarithmic temperature difference between CGS and SGS in octane when the CGS is rotated by 0º with respect to SGS (red line) and CGS is rotated by 90º with respect to SGS (blue line).

We conducted additional simulations of three GS in vacuum and in octane where the CGS is rotated 90° with respect to the SGS, maintaining constant the interfacial area across which heat transfer occurs, A_T in Eq. (4.1). The CGS-SGS temperature difference for the two cases during the NVE simulation phase is shown in Fig 4.7. We observed that the Kapitza resistance is ~15% higher when the CGS is rotated 90° with respect to the SGS compared to when the GS are oriented parallel to each other. To

speculate on the increased Kapitza resistance, we calculated the separation distance between the GS in both the cases. During the initial steps of relaxation, we observed that the CGS-SGS distance increased by 0.7 Å when the CGS is rotated 90° with respect to the SGS and 0.5 Å when the GS are oriented parallel to each other. Although the heat transfer area is the same in both the cases, the CGS expands more due to heating when it is oriented 90° with respect to the SGS which lead to the increased Kapitza resistance in this case.

In summary, our calculations suggest that the GS-GS contact has larger Kapitza resistance than GS-matrix contacts when the matrix is octane,[220] which is in agreement with what has been observed for CNTs.

4.3.3 Comparison to Carbon Nanotubes

It is of interest to compare the values for the Kapitza resistance at GS-GS contacts to those reported in the literature for CNT-CNT. Zhong et al.,[143] who calculated the Kapitza resistance at CNT-CNT contacts by fitting the transient temperature profiles obtained by molecular dynamics to a finite different solution of the one-dimensional heat equation, reported a value of 8-11 × 10^{-8} Km^2W^{-1} for CNT-CNT Kapitza resistance. The nanotubes considered were (10,10), with diameter ~1.356 nm. Maruyama et al.[141] used the simulation protocol implemented in the present work, applied to a bundle of 7 (5,5) CNTs equilibrated at 300K in vacuum. The nanotube diameter was of ~ 0.693 nm. The central CNT was suddenly heated to 400K for 10 ps, after which the system was allowed to relax in the NVE ensemble. The CNT-CNT Kapitza resistance was found to be 24.8 × 10^{-8} Km^2W^{-1}. Bui et al.,[140] by fitting Monte

Carlo simulation results to experimental data, estimated the CNT-CNT Kapitza resistance to be ~12.15 × 10^{-8} Km^2W^{-1}. Our estimations for the GS-GS Kapitza resistance are ~30% lower than the minimum ones reported in the literature for CNT-CNT contacts, and ~70% lower than those estimated for CNT-CNT contacts employing methods similar to those employed herein. It is however expected that as the CNT diameter increases the Kapitza resistance observed at CNT-CNT contacts will become comparable to that observed at GS-GS interfaces.

4.4 Conclusions

In summary, using classical MD simulations we have studied the Kapitza resistance between GS in vacuum and in octane. We estimate that the GS-GS Kapitza resistance is ~ 6.5×10^{-8} Km^2W^{-1} when three GS are in octane and ~ 7.7×10^{-8} Km^2W^{-1} when the GS are in vacuum. These values are slightly larger than those observed at the GS-octane interface, ~ 5.5×10^{-8} Km^2W^{-1}. Our results suggest significantly lower Kapitza resistances for the GS-GS interface than those reported at the CNT-CNT interface.

5 Simulation Insights on Thermally Conductive Graphene-Based Nanocomposites

The material presented below was published in 2011 in volume 109, issue 1, and page 97 of the Taylor & Francis journal Molecular Physics.

5.1 Introduction

Dispersing nanoparticles in a polymer can enhance both mechanical and transport properties. Nanocomposites with high thermal conductivity could be obtained by using thermally conductive nanoparticles. Carbon-based nanoparticles are extremely promising, although high resistances to heat transfer from the nanoparticles to the polymer matrix could cause significant limitations.

We focus here on GS dispersed within n-octane. Although pristine GS agglomerate, our equilibrium MD simulations suggest that when the GS are functionalized with short branched hydrocarbons along the GS edges, they remain well dispersed. We report results from equilibrium and non-equilibrium molecular dynamics simulations to assess the effective interactions between dispersed GS, the self-assembly of GS, and the heat transfer through the GS-octane nanocomposite. Our tools are designed to understand the effect of GS size, solvent molecular weight and molecular architecture on the GS dispersability and GS-octane thermal conductivity. We provide evidence for the formation of nematic phases when the GS volume fraction increases within octane. The atomic-level results are input for a coarse-grained Monte Carlo simulation that predicts anisotropic thermal conductivity for GS-based composites when the GS show nematic

phases. The remainder of the Chapter is organized as follows: in Section 5.2 we discuss our simulation methods, which range from all-atom equilibrium simulations to coarse-grained Monte Carlo methods; in Section 5.3 we discuss some recently obtained results and compare them to other GS-based nanocomposites; in Section 5.4 we summarize our main conclusions and highlight some questions that require further research.

5.2 Simulation Methodology

To conduct our all-atom molecular dynamics (MD) simulations for the stability of GS we employed the simulation package LAMMPS.[193-194] All results were obtained using equilibrium MD within the NVT and NPT ensembles and 1 fs timestep. Periodic boundary conditions were applied in all three directions. Parameters and other details necessary to implement all force fields implemented are given in Table 1.1. In our previous work we considered n-octane, n-hexane and n-dodecane.[203] Here we only consider n-octane, which is described as a flexible linear chain of CH_2 pseudo atoms terminating at both ends with CH_3 groups. In each simulation box 5 or more GS of 216 carbon atoms (~ 2.5 nm in diameter) were diluted in up to 2500 molecules of n-octane. Details about the simulation protocol are described in section 2.1. Suffice it to say that after a NPT equilibration phase conducted at ambient conditions, the simulations were conducted in the NVT ensemble at 300 K for up to 250 ns. The system density during the production phase was comparable to the experimental densities of liquid n-octane at 300K. The size of the simulation box was ~ 100×100×100 Å.

To assess, via non-equilibrium all-atom molecular dynamics simulations, macroscopic thermal conductivities we implemented the method proposed by Muller-Plathe.[206]

Further details about this algorithm are discussed in Section 5.4. These calculations are performed using the force fields of Table 1.1.

Details of the Monte Carlo algorithm implemented to estimate macroscopic thermal conductivity for GS-based composites have been described in previous works.[224-226] The heat transport is considered to depend on the behavior of discrete heat walkers that travel through the composite by Brownian motion.[227] At each time step, the walkers move in each one of the three Cartesian directions via random jumps of length randomly sampled from a normal distribution with zero mean and standard deviation σ, given as

$$\sigma = \sqrt{2D_m \Delta t} \quad . \tag{5.1}$$

In Eq. (5.1), D_{m} is the thermal diffusivity of the matrix material and Δt is the time increment characteristic of the Monte Carlo simulation. Once a thermal walker arrives at a matrix-GS interface, it can either enter the GS or remain within the matrix. The probability $f_{\mathrm{m}-i}$ determines whether the heat walker can move into the GS; $(1-f_{\mathrm{m-i}})$ is the probability for the random walker to remain within the matrix. Once a walker moves inside a GS, because the thermal conductivity of the GS is about four orders of magnitude larger than that of typical polymeric matrixes, it is assumed that the walker distributes randomly and uniformly inside the GS. In every subsequent time step, the heat walker can exit the GS or remain inside it, depending on the probability $f_{i\text{-}m}$. If the walker remains inside a GS, it is randomly assigned a different position inside the GS. Based on thermal equilibrium, and assuming that the Kapitza resistance is the same

when entering and when exiting the inclusion, the probabilities f_{m-i} and f_{i-m} are related as follows:

$$V_i \, f_{i-m} = C_f \, \sigma A_i \, f_{m-i} \quad . \tag{5.2}$$

In Eq. (5.2), A_i and V_i are the surface area and the volume of the GS, respectively, and C_f is a thermal equilibrium factor, which depends on the nanoinclusions geometry and needs to be determined empirically.[216]

In the present work, instead of placing the walkers at the interface before moving out of the GS as done in our prior work for simulating CNT composites,[225-226] the exiting walkers are placed randomly inside the GS. This scheme results in a uniform and continuous distribution of walkers inside and outside the GS, even across the interface, at conditions of thermal equilibrium.

The numerical methodology for calculating the thermal equilibrium factor C_f in Eq. (5.2) has been described by Duong et al.[225-226] for systems containing CNT. For GS, C_f is obtained as follows: First, one parallelepiped (because C_f only depends on the nanoinclusion geometry, this parallelepiped represents one GS even though the dimensions may not correspond to actual GS used as fillers in subsequent simulations) with dimensions of 5.67nm x 20.35nm x 1.27 nm is placed randomly inside a cubic computational cell of size 64nm (64 x 64 x 64 grid points). Second, heat walkers are released at every grid unit and are allowed to perform a random walk. The fraction of heat walkers inside the GS is calculated after increments of 500 time steps and the simulation is stopped once this value does not change any longer (equilibrium state). The correct value of the equilibrium factor (C_f = 0.33) is considered to have been

reached when the volume fraction of the parallelepiped in the simulation box is equal to the fraction of heat walkers inside the parallelepiped. Lastly, the C_f just obtained is checked for consistency by inserting 55 GS (each of size 5.67nm x 20.35nm x 1.27 nm) inside a cubic computational domain of size 100nm (96 x 96 x 96 grid points) and examining the fraction of heat walkers inside each GS as compared to the GS volume fraction.

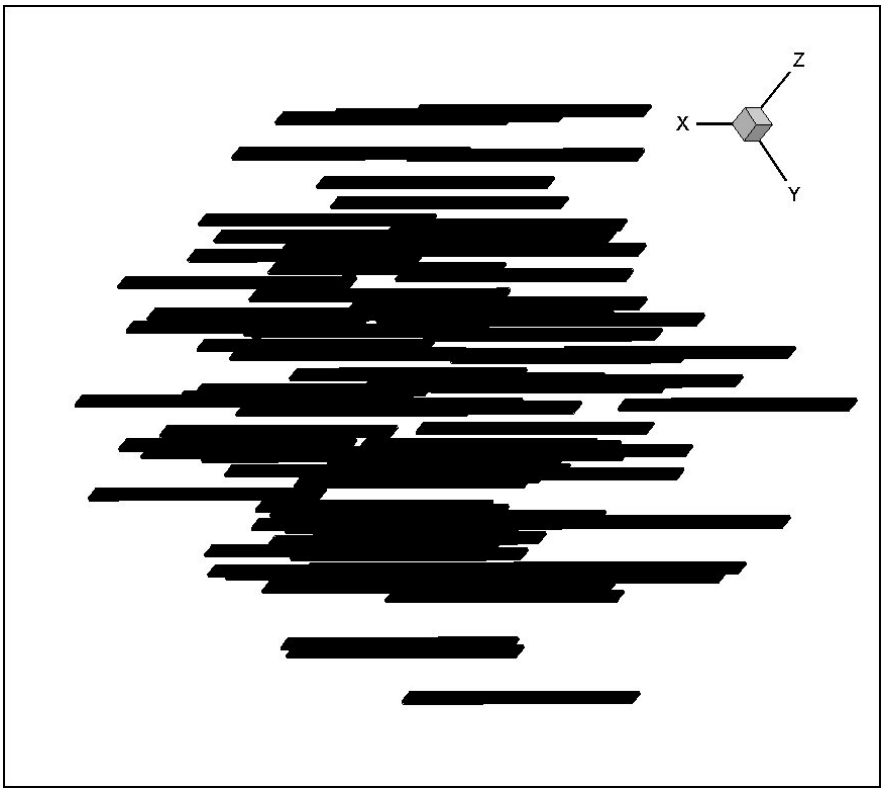

Figure 5-1 Schematic representation of a GS-based material in which the GS are considered as rectangular inclusions parallel to the X direction. 88 GS are considered in the simulation box of size 100X100X100 nm. The GS has length ~30 times the width and ~190 times the thickness, 0.34 nm.

In order to estimate the effective thermal conductivity of a GS nanocomposite, a cubic computational domain of size 100 nm and with 300x300x300 grid points was used. The GS are considered as rectangular sheets with thickness equal to the distance between

two graphite layers, 0.34nm.[228] The GS are placed randomly inside the domain, but controlling their relative orientation and preventing overlaps or contacts with each other (see Fig 5.1). A large number of hot thermal walkers (90,000) are released from one side of the computational domain, at $x = 0$, representing a heated surface. An equal number of cold walkers were released from the opposite side of the computational domain, a cooled surface. The time step is set at 10^{-4} sec. The simulation is conducted under the periodic-image convention along the y and z directions. This scenario corresponds to the case of imposing a constant heat flux throughout the domain. The local temperature is obtained by counting the number of heat walkers in each grid unit. At steady states the temperature profile along the x direction yields a straight line with slope inversely proportional to the macroscopic, effective thermal conductivity. Because the GS distribution within the composite is not uniform, the thermal conductivity was estimated from the slope of the temperature profile at the center of the simulation box. The reliability of the method just described has been demonstrated earlier via comparison to available experimental data.[225] Results are shown herein as the ratio between the effective thermal conductivity of the nanocomposite and that of the organic matrix without the GS (K_{eff}/K_m). The intrinsic thermal conductivity of the GS is assumed to be 4 orders of magnitude larger than that of the organic matrix, in qualitative agreement with experimental data for GS and polymeric materials. Six different simulations with different random placements of the GS in the computational domain are conducted for each simulated case. The error in our calculations was estimated using the variance of the results calculated using Student's t-test with 95% level of confidence.

The Kapitza resistance is an input parameter to our Monte Carlo simulations. Our MD simulation results for the Kapitza resistance[220] were used to estimate values of the probability f_{m-i} shown in Eq. (3). According to the simplified acoustic mismatch theory,[106] f_{m-i} is calculated from the Kapitza resistance as follows:

$$f_{m-i} = \frac{4}{\rho_m C_m \nu_m R_{bd}} \tag{5.3}$$

In Eq. (5.3) subscript *m* designates the organic matrix and subscript *i* designates the GS inclusion, ρ is the density of the matrix material; *C* is the specific heat; ν is the velocity of sound in the matrix, and R_{bd} is the Kapitza resistance. When simulation data for R_{bd} are not available from direct simulations, alternative approaches are possible for estimating f_{m-i}, as will be discussed in our upcoming manuscript.[229]

5.3 Results and Discussion

Based on common knowledge in the field of colloidal sciences,[134-135, 184, 200] our goal is to provide stabilization in GS-based organic dispersions by functionalizing the edges of the GS. Such functionalization is experimentally possible by taking advantage of a number of oxygenated sites that are typically present in partially oxidized GS, or by following synthetic chemistry procedures, as demonstrated for example by Yang et al.[24]

In Chapter 2 we demonstrated, using equilibrium molecular dynamics simulations, that functionalizing the edges of small GS with an appropriate number of branched organic groups it is possible to secure the stability of dispersions formed by GS and various organic solvents, including n-octane. Geometric considerations can help us determine the minimum number of functional groups, equally spaced along the GS edges,

necessary to stabilize GS of various sizes. We found that for short functional groups to be effective it is necessary that they are branched because only in this way it is possible for each functional group to protrude towards both directions perpendicular to the GS plane.[203] According to this mechanism, stabilization is achieved via steric effects. Such ideas are discussed at length in our previous manuscript.[203]

It is important to report that experimental results recently reported by the group of Liang-shi Li[117-118] corroborate our predictions. Li and coworkers functionalized small GS of 130-170 carbon atoms (comparable in size to those simulated[203]), produced via chemical synthesis, using multiple 2',4',6'-triakyl phenyl groups covalently attached to the GS edges. The graphene quantum dots obtained resulted soluble in common organic solvents such as chloroform and toluene. It should be pointed out that the 2',4',6'-triakyl phenyl groups contain three branches, and therefore are likely to provide the steric stabilization discussed above. As the GS size increases, the steric stabilization provided by functional groups on the GS edges will eventually not be sufficient to prevent agglomeration. As shown by Fang et al.,[122] under such circumstances it is possible to take advantage of the presence of oxygenated sites on partially oxidized GS to graft short polymer chains (e.g., polystyrene). This strategy yields GS of considerable size (in the range 0.5 to 1.5 μm) with stable dispersions in various organic solvents, e.g. toluene, and have been used to prepare polystyrene-GS composites.

5.3.1 Stable Dispersions of GS in Oils

Pushing the limits of modern computational resources, our recent results suggest that appropriately functionalizing the edges of GS with branched groups it is possible to

stabilize dispersions containing GS of 216 carbon atoms (with diameter of ~ 2.5 nm). In Fig 5.2 we report representative simulation snapshots (top), center-to-center radial distribution functions (middle), and effective potentials of mean force (bottom) for systems composed by 216-carbon-atoms functionalized GS in n-octane as obtained after 250 ns of MD simulations. To provide steric stabilization, each GS was functionalized by 18 alkanes, each with two branches of 11 united-atom groups. The results are shown at increasing GS volume fraction (from left to right, results are obtained at 6, 23 and 45 % GS volume fraction), and demonstrate that, within the length of our simulations, the functionalized GS remain stable in the various dispersions (note that the RDF equals zero at close GS-GS separations) despite the rather large concentrations used.

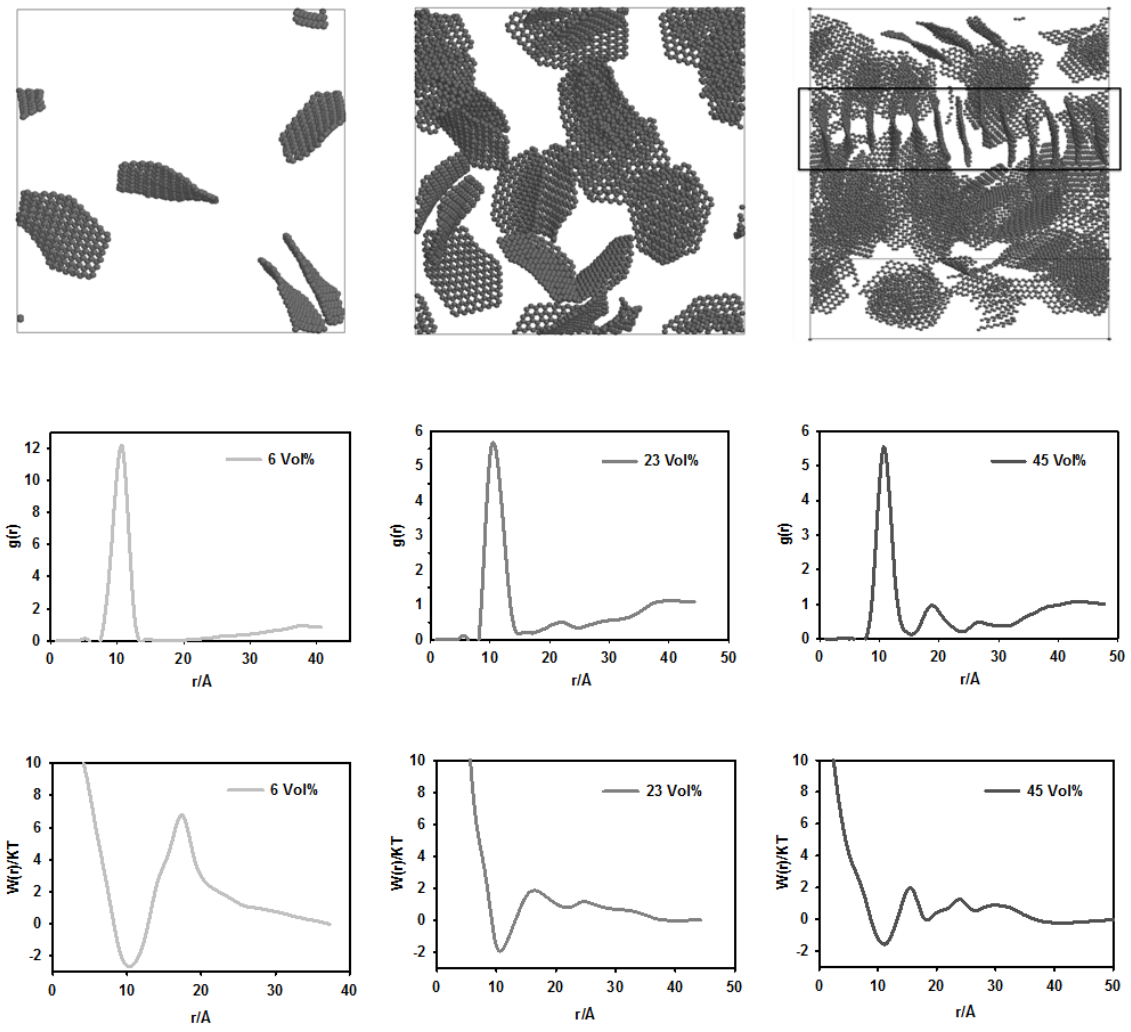

Figure 5-2 Representative simulation snapshots (top), center-to-center radial distribution functions (middle), and effective potentials of mean force (bottom) for systems composed by GS of 216 carbon atoms functionalized with 18 branched functional groups in n-octane. All simulations were conducted at 300K. In the top panel, the functional groups of GS and surrounding octane were not shown for clarity. From left to right, results are for systems at increasing GS volume fraction.

The results obtained at low GS volume fraction appear to depict isotropic systems, while those obtained at large volume fractions (i.e., 23% or larger) suggest the formation of domains within which the GS are parallel to each other. Because functionalized GS could be described as 'soft discs', it is likely that they could behave as liquid crystals and show a number of phase transitions such as those described for

systems of cut spheres by Duncan et al.[230] Unfortunately, equilibrium molecular dynamics simulations at the all-atom level are not adequate for exploring the complete phase diagram of such a complex system because of its tendency to be trapped in local minima of the free-energy landscape.

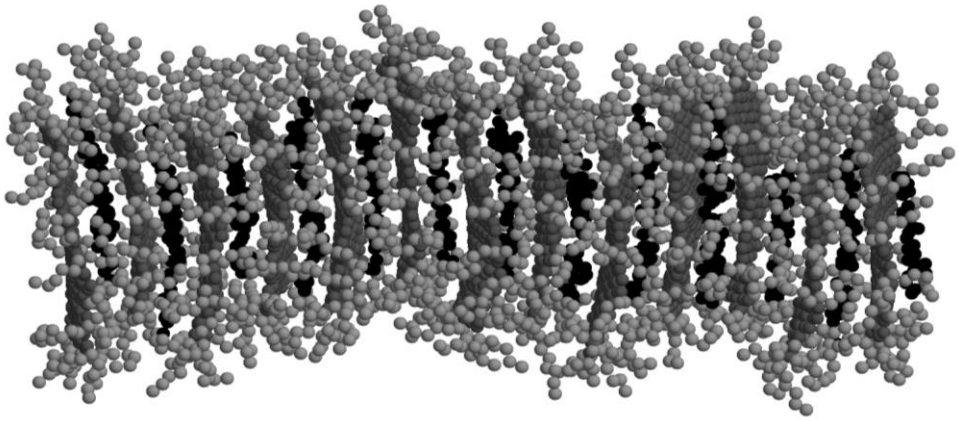

Figure 5-3 Snapshot of the column of GS formed in the system with 45.0 vol% of GS in which n-octane molecules can be seen sandwiched in between neighboring GS. The carbon atoms in GS are shown in dark gray, functional groups in light gray and octane in between the GS in black. Surrounding octane is not shown for clarity.

Nematic order-parameter calculations[231] yield values of ~ 0.45 and ~ 0.3 when the GS volume fraction is 6 and 23%, respectively. These results suggest that the system is isotropic at low GS volume fraction, as indicated by visual inspection. At larger GS volume fractions we do not attempt to quantify the order parameter because it is likely that the system shown in the right panel of Fig. 5.2 is kinetically locked and therefore may not be representative of equilibrium conditions. However, we highlight the formation of one column of GS that spans the entire length of the cubic simulation box shown in the right panel of Fig. 5.2 (see rectangle on top right panel). We reproduce this column in Fig. 5.3, where n- octane molecules can be seen sandwiched in between neighboring GS. As the size of the GS increases we expect that structures such as the

one represented in Fig. 5.3 become more frequent within a GS-based nanocomposite. The spacing between neighboring GS will certainly depend on the organic medium (in the present case n-octane), and also on the GS functionalization. Specifically, when the GS planes are functionalized with short polymer chains, as done experimentally by Fang et al.,[122] it will be possible to increase the distance between neighboring GS, and obtain nematic phases at lower GS loadings. It might also be possible to promote the formation of nematic phases in which the GS are parallel to each other by shearing a composite material containing functionalized GS. Such materials could present anisotropic properties.

5.3.2 Microscopic Thermal Conductivity

Towards the production of composite materials with anisotropic thermal conductivity it is of interest to assess whether the thermal conductivity is anisotropic in a structure such as that of Fig. 5.3. As mentioned in Section 5.2, to manufacture thermally conductive GS-based nanocomposites it is necessary to reduce the Kapitza resistance.[105] In Chapter 3, we demonstrated using non-equilibrium MD simulations, that the Kapitza resistance is important also in GS-based nanocomposites.[220] Our results, not reported here for brevity, show that the Kapitza resistance at the GS-octane interface for small GS is comparable to, but smaller than that observed for CNT. Unfortunately, our results also suggest that the Kapitza resistance increases as the GS size increases. More important, however, is that we found that it is possible to reduce the Kapitza resistance significantly by functionalizing the GS.[220] Because, based on our predictions[203] and on experimental evidence,[82, 122, 180-181] the GS functionalization is necessary to stabilize organic dispersion of GS, and because the functionalization of the GS edges is likely

not to significantly deteriorate the intrinsic thermal transport properties of individual GS, our previous results suggest that GS-based nanocomposites could show enhanced thermal conductivity. Recent experimental data seem to support this expectation.

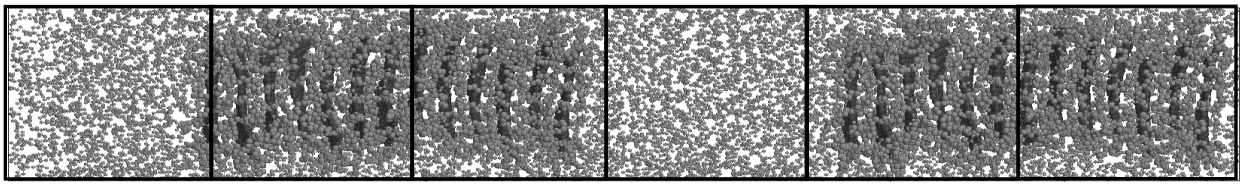

Figure 5-4 Representative snapshot of the system simulated to calculate the macroscopic thermal conductivity in a GS-octane nanocomposite. The region in the first bin from the left is maintained cold and the region in the fourth bin from the left is maintained hot.

To assess the likelihood of anisotropic thermal conductivity properties in a nanocomposite with atomic texture such as that represented in Fig. 5.3, we implemented the algorithm proposed by Muller-Plathe.[206] We studied the thermal conductivity in the directions parallel and perpendicular to the GS. The simulated system is shown in Fig. 5.4. The columnar structure is surrounded by n-octane. We first equilibrate the system, while imposing geometric constrains on the GS centers of mass, at T=350K and P=1 atm. The simulation box is divided into 6 bins in the direction of heat flow. Then kinetic energy is exchanged at fixed intervals between the five hottest n-octane molecules found on the first bin from the left (the cold region of the simulation) and the five coldest molecules found on the fourth bin from the left (the hot region of the simulation box). As a consequence of the imposed energy flux a temperature profile establishes throughout the simulation box, with the temperature in the first bin from the left lower than that on the fourth bin from the left. The simulation continues until a stable temperature profile is obtained. From the slope of the temperature profile at the center

of the simulation box (correspondent to GS-rich nanocomposite) it is possible to extract the thermal conductivity:

$$K_{eff} = -\frac{\sum_{transfers} \frac{m}{2}(v_h^2 - v_c^2)}{2tL_xL_y\langle \partial T / \partial z \rangle} \quad (5.5)$$

In Eq. (5.5), K_{eff} is the thermal conductivity of the composite, t is the simulation time, L_x and L_y are the box dimensions in x and y direction, and m is the mass of the molecule whose velocities in the hot (v_h) and cold (v_c) regions are interchanged.

In Fig. 5.6 we report a schematic of the simulation box (top) and the temperature profile obtained at steady-states (bottom) when the heat flows in the direction perpendicular to the GS. In Fig. 5.8 we report a schematic of the simulation box (top) and the temperature profile obtained at steady-states (bottom) when the heat flows in the direction parallel to the GS. Additional simulations were conducted to assess the thermal conductivity in liquid n-octane. In Fig. 5.5 we report a schematic of the simulation box (top) and the temperature profile obtained at steady-states (bottom) when the algorithm proposed by Muller-Plathe is implemented to calculate the thermal conductivity of liquid n-octane. From the slope of the temperature profile shown by the two lines in the figure (bottom) we obtained a thermal conductivity of ~ 0.11±0.02 W/mK, in reasonable agreement with experimental data (0.128 W/mK[222]).

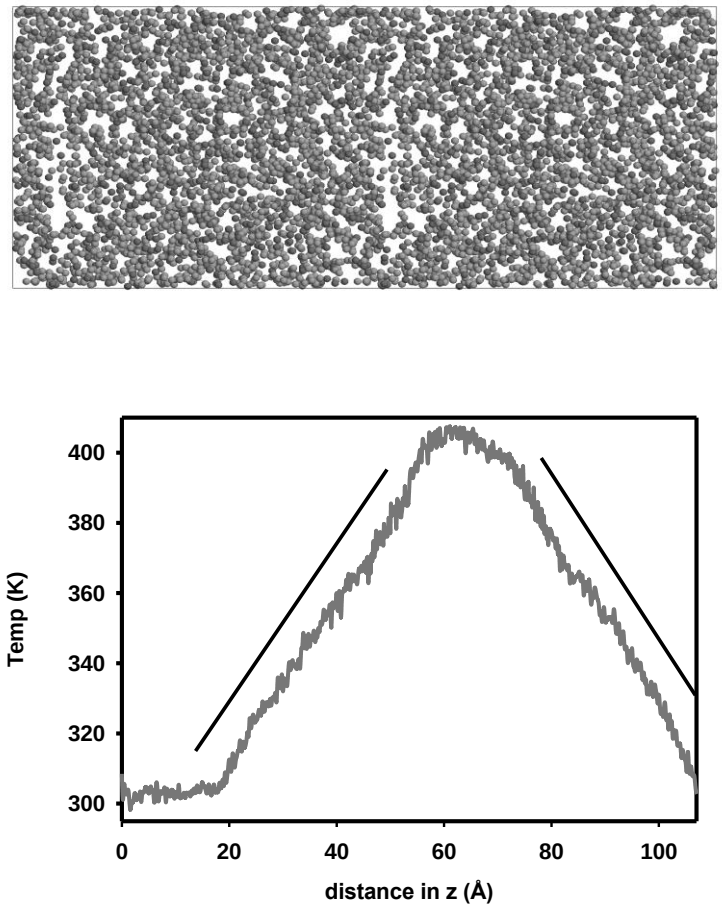

Figure 5-5 Schematic of the simulation box (top) and temperature profile obtained at steady-states (bottom) when the heat flows through octane. The lines in the bottom panel are schematics for calculating the thermal conductivity using Eq. (5.5).

From the results in Fig. 5.6 we extract a macroscopic thermal conductivity of 0.24±0.02 W/mK in the direction perpendicular to the GS, approximately twice the value obtained for n-octane. This result is surprising for two reasons. Firstly, because it was expected that GS-based nanocomposites show large thermal conductivity in the direction parallel to their plane, and not on the one perpendicular to it. Secondly, because heat should flow in and out of many GS when the nanocomposite is organized as shown in Fig. 5.6, and therefore several barriers to heat flow should become evident from the simulation

results. Instead the temperature profile appears rather linear, with no clear indication of barriers to the heat flow at the various GS-octane interfaces. It is likely that instead of flowing through the carbon atoms present within each GS plane, the thermal energy transfers along the functional groups grafted at the GS edges. Because such groups are branched, they extend along both directions perpendicular to each GS, and therefore the functional groups of one GS are intertwined with those of the neighboring ones, facilitating heat transfer. Indeed, when the temperature profile of the GS carbon atoms is analyzed, a sequence of steps is observed along the direction of heat flow, while a continuous profile is obtained for the temperature of the functional groups. Also, the temperature of the functional groups is always larger than that of the GS carbon atoms. These results are reported in Fig. 5.7.

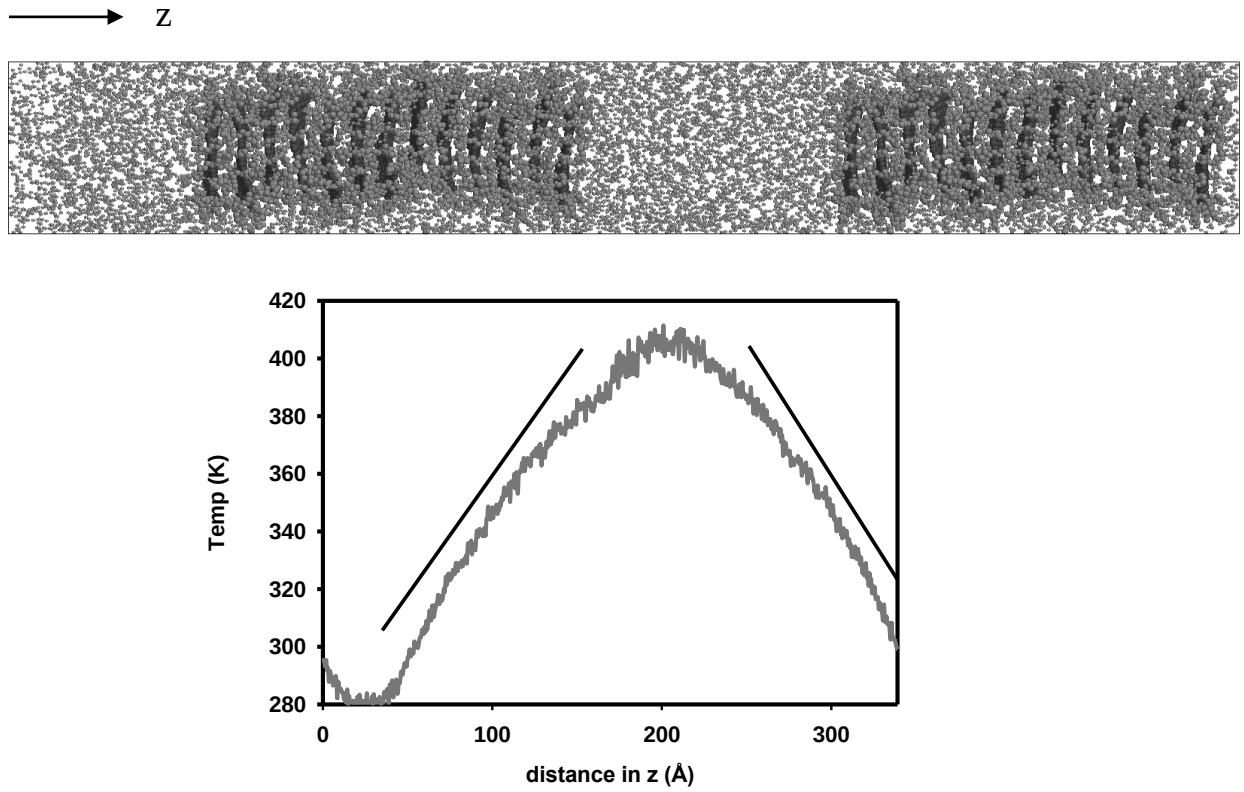

Figure 5-6 Schematic of the simulation box (top) and the temperature profile obtained at steady-states (bottom) when the heat flows in the direction perpendicular to the GS. The lines in the bottom panel are schematics for calculating the thermal conductivity using Eq. (5.5).

In Figure 5.7 we report the temperature profile of the GS carbon atoms (gray line) and the functional groups of GS (black line) when the heat flows in the direction perpendicular to the GS (see Fig. 5.6). From the results it is evident that the temperature of the functional groups is always larger than that of the GS carbon atoms. The former temperature profile shows a smooth linear profile, while a sequence of steps is observed for the temperature profile of GS carbon atoms. These results suggest that the heat flows through the functional groups grafted to the GS instead of flowing through the GS

carbon atoms. Because the branched functional groups extend along both directions perpendicular to each GS, and because the distance between two adjacent GS is smaller than the length of the grafted functional groups, the functional groups of one GS are intertwined with those of the neighboring ones, facilitating heat transfer.

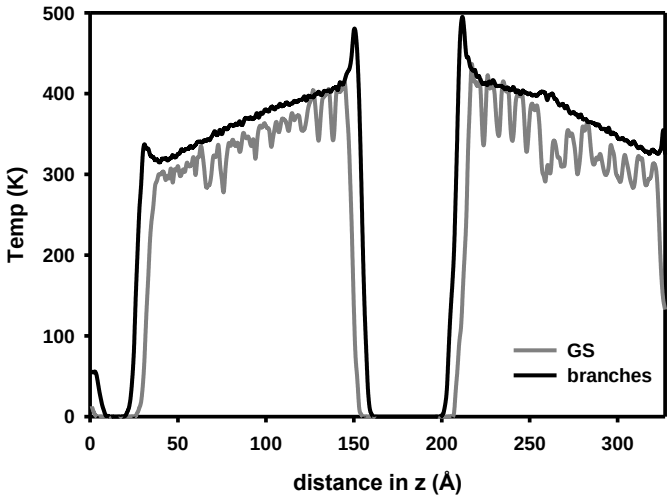

Figure 5-7 Temperature profile of the carbon atoms in GS (gray line), and the functional groups of GS (black line) in the direction of flow (perpendicular to GS). See Figure 5.6 for details.

The results presented in Fig. 5.8 show evidence of two Kapitza resistances: one encountered by the thermal energy as it enters the GS from the hot region, and one encountered as the thermal energy leaves the GS to warm the cold octane. At the center of the simulation box, roughly correspondent to the position in which heat flows predominantly through the GS planes, we observe a thermal conductivity of 0.345±0.02 W/mK, approximately three times that observed for liquid n-octane. Although this thermal conductivity is not near that observed both experimentally and via simulations[62-63] for large GS, this value corresponds to a significant enhancement compared to the thermal conductivity of liquid n-octane (0.11±0.02 W/mK). It is likely

that for small GS such as those considered in our simulations the thermal conductivity is not as high as it is for macroscopic GS, and it is also possible that in small GS the edge functionalization necessary to prevent agglomeration actually deteriorates the intrinsic thermal transport properties of individual GS. Detailed analysis (see Fig. 5.9) of the temperature profile for GS and for n-octane, sandwiched in between neighboring GS as shown in Fig. 5.3, shows that heat transfers more effectively through the GS inclusions than through the organic matrix.

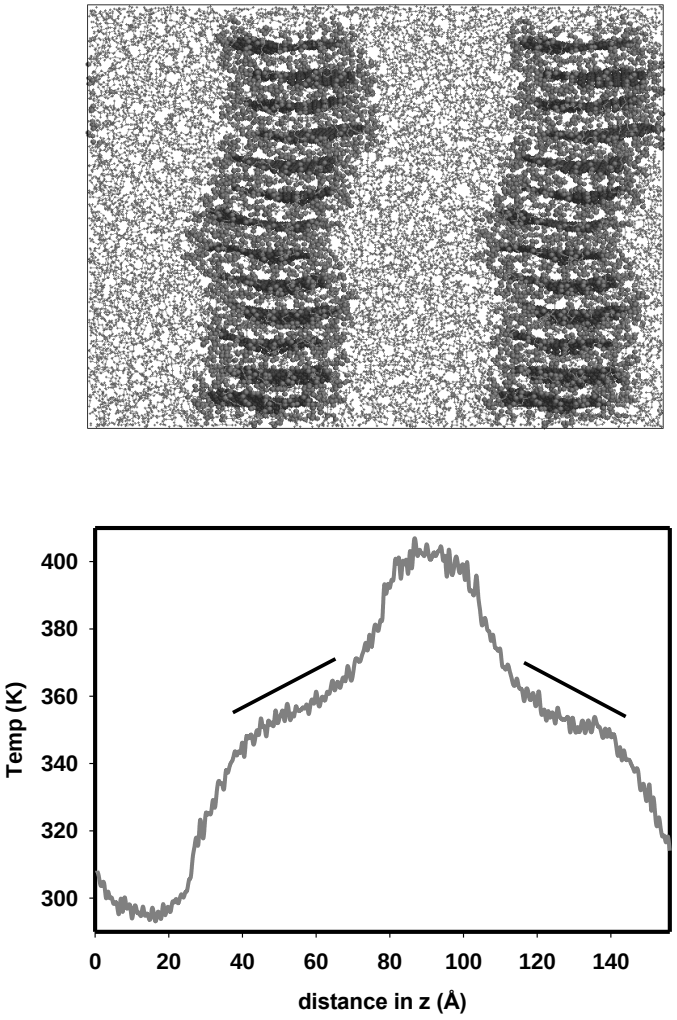

Figure 5-8 Schematic of the simulation box (top) and the temperature profile obtained at steady-states (bottom) when the heat flows in the direction parallel to the GS. The

lines in the bottom panel are schematics for calculating the thermal conductivity using Eq. (5.5).

In Fig. 5.9, we report the temperature profile for functionalized GS (gray line) and n-octane (black line) when the heat flows in the direction parallel to the GS (see Fig. 5.8). As the slope of the temperature profile is inversely proportional to the thermal conductivity of the nanocomposite (see Eq. 5.5), our results show that heat transfers more effectively through the GS inclusions than through n-octane molecules sandwiched between neighboring GS.

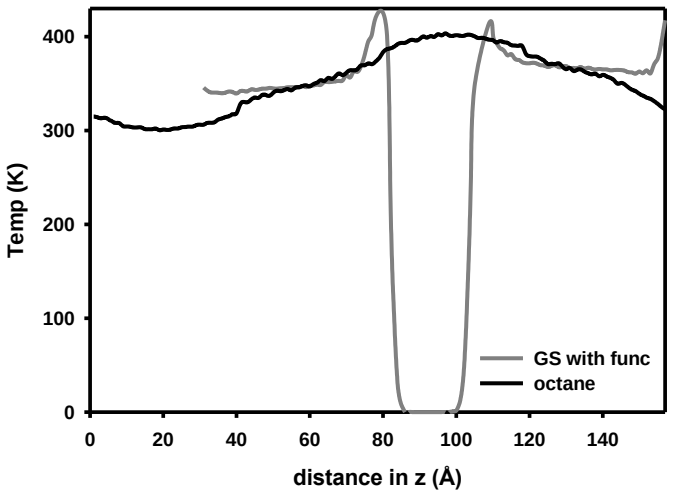

Figure 5-9 Temperature profile of GS (gray line) and octane (black line) in the direction of heat flow (parallel to the GS, see Fig. 5.8 for details).

Combining the results shown in Fig. 5.6 and those shown in Fig. 5.8 we conclude that our simulations, although conducted for one system composed by rather small and densely packed GS, show evidence of anisotropic thermal conductivity, with thermal conductivity in the direction parallel to the GS approximately 50% larger than that observed in the direction perpendicular to the GS. For the reasons discussed above, this anisotropic property is expected to become more accentuated as the GS size increases

(because the number of GS-organic matrix barriers in the direction parallel to the GS should decrease and because the GS functionalization should have less of an impact on the intrinsic thermal transport properties of individual GS). More coarse grained methods are necessary for exploring such systems from a theoretical perspective.

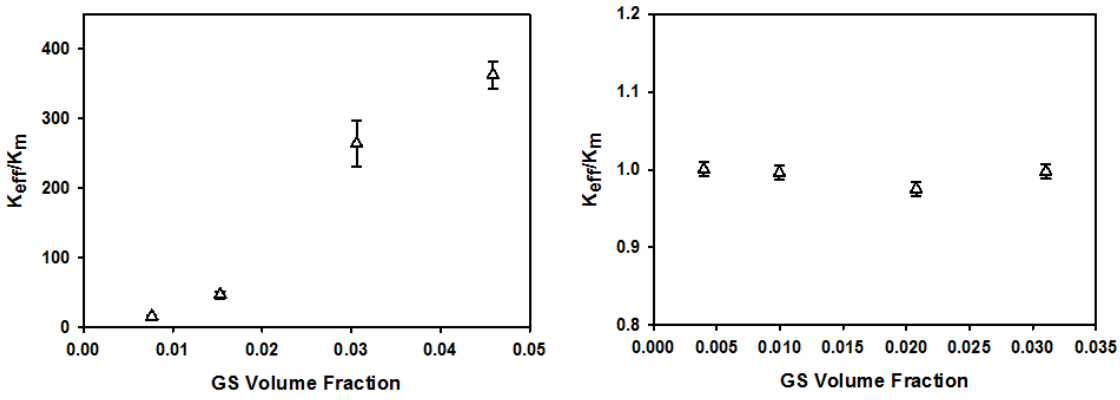

Figure 5-10 Reduced thermal conductivity along the direction parallel to the GS (left panel) and that perpendicular to the GS plane (right panel) for a GS-based nanocomposite schematically represented in Fig. 5.1. The results are shown as a function of the GS volume fraction. While the thermal conductivity in the direction perpendicular to the GS does not change significantly as the GS loading increases, GS yield large increases in the thermal conductivity along the direction parallel to the GS even at modest loading (GS size: 64nm x 2.52nm x 0.34nm).

5.3.3 Macroscopic Thermal Conductivity

Along those lines, following the methods developed earlier to study the thermal conductivity of nanocomposites containing CNT (described in Section 5.3),[216, 225] we assessed the effective thermal conductivity (the ratio between the calculated thermal conductivity of the GS composite to that of the polymer matrix) of a GS composite as a function of the GS volume fraction up to 5% GS loading. It should be pointed out that within our coarse-grained model, the chemical nature of both GS and organic matrix is only rendered via their respective thermal conductivities, the Kapitza resistance

encountered by heat as it flows from the GS to the organic matrix, and by the size and shape of the GS inclusion. As a consequence, systems much larger than those simulated at the all-atom level can be considered. To assess the possibility of observing anisotropic thermal conductivity, the GS are distributed randomly within the organic matrix, but are parallel to each other, as shown schematically in Fig. 5.1. The thermal conductivity is evaluated in the directions parallel and perpendicular to the GS. The results are shown in Fig. 5.10 for GS of size 64 nm in length and 2.52 nm in width, thus much larger than those considered in our all-atom simulations. Several simulations were considered at varying aspect ratio (L/D) for the GS. The effective thermal conductivity was found to be almost constant when L/D was changed in the range between 80 and 120. For computational economy reasons, we chose L/D=80. Such a high aspect ratio is expected to enhance anisotropic thermal conductivity. Note also that such large GS cannot be simulated using the all-atom approach discussed above. The GS thermal conductivity is assumed to be several orders of magnitude larger than that of the organic matrix, in accordance with experimental observations, allowing the simulation of the large GS in the model as having infinite thermal conductivity relative to the matrix. The results indicate that the thermal conductivity in the direction parallel to the GS plane, along the longest dimension of the GS, increases as the GS loading increases (left panel in Fig. 5.10), while the thermal conductivity perpendicular to the GS remains comparable to that of the organic matrix at all GS loadings (right panel in Fig. 5.10). The latter observation is due to the high GS-matrix Kapitza resistance and to the small thickness of the GS. Quantitative comparison between the results in Fig. 5.10 to those in Figs. 5.6 and 5.8 is not possible because of different GS dimensions considered,

because of different GS loadings simulated, and also because the mechanism for thermal conductivity observed in Fig. 5.6 is dictated by heat flowing through the GS functional groups, which is not considered in the coarse-grained system where the GS are separated from each other. The main difference between the two sets of calculation, however, is to be found on the size of the GS. Because the length of the GS is 64nm (those in Figs. 5.6 and 5.8 are of about 2 nm in size), enhancements on the macroscopic thermal conductivity up to 400% are predicted in the direction parallel to the GS. The results of Fig. 5.10 are dependent on the input parameters. Specifically, the GS thermal conductivity is assumed to be four orders of magnitude larger than that of the organic matrix (this is consistent with experimental data for macroscopic GS, but may not hold for small GS such as those considered in Fig. 5.10), and the Kapitza resistance is taken from MD simulations of small functionalized GS (0.42×10^{-8} m^2K/W)[220] and assumed to remain constant anywhere on the GS-octane interface. Because our MD simulations showed that the Kapitza resistance depends on the GS size, the Kapitza resistance used in the calculations of Fig. 5.10 may be lower than it should, but our MD simulations also show that appropriate functionalization reduces the Kapitza resistance. Despite the large difference in the effective thermal conductivities predicted at the all-atom and at the coarse-grained levels, it is encouraging to observe that both calculations consistently predict the possibility of attaining anisotropic thermal conductivity for GS-based nanocomposites.

5.3.4 Comparison of Effective Thermal Conductivity between various GS-based Nanocomposites

In Table 5-1 we compare the effective thermal conductivities of various GS-based nanocomposites in the literature with those in our study. The symbols ⊥ and ∥ indicate whether the direction of the measurement is perpendicular or parallel to the surface of the GS, respectively. The experimental techniques used in the literature studies to measure the thermal conductivity are transient plane source method, laser flash method, hot-wire method, and steady-state method. Non-equilibrium MD, Monte Carlo and finite element method were used to estimate the thermal conductivity in simulation studies. The types of fillers used are graphene, functionalized graphene, single layer graphene (SLG), exfoliated graphene, graphene oxide (GO), functionalized graphene oxide (FGO), graphene nanoplatelets (GNP), multilayer graphene (MLG), etc. The various types of matrix used are epoxy, polystyrene, silicone polymer, polyurethane, octadecanol, deionized water, poly (vinylidene fluoride), polypropylene, aluminum/Teflon, high density polyethylene, polyimide, paraffin, polyaniline, bromobutyl rubber, stearic acid, polyamide-6, 6, and phenolic resin. From the table, we can observe that the addition of GS as fillers enhances the thermal conductivity of the resulting nanocomposites. The effective thermal conductivity of the various GS-based nanocomposites ranges between 1.10 – 400.0 depending on the type of the filler, the type of matrix, synthesis method of filler, the composition and alignment of the filler in the matrix. Our results for the direction dependent thermal conductivity of the GS-octane nanocomposites are consistent with the results of Alghemandi et al.[232] and Eslami et al.,[233] who observed that the thermal conductivity of GS-polyamide-6,6

nanocomposite in the direction parallel to the plane of the GS is higher than the thermal conductivity in the direction perpendicular to the plane of the GS.

Table 5-1. Summary of Effective Thermal Conductivity (K_{eff}/K_m) of GS-based Nanocomposites. The symbols ⊥ and ‖ indicate whether the direction of the measurement is perpendicular or parallel to the surface of the GS, respectively.

Filler – Matrix	**Filler Synthesis Method**	**Matrix**	**Measurement Method**	**Loading of Filler**	**(K_{eff}/K_{m})**	**Authors**
Graphene oxide (GO)	Hummers Method	Epoxy	Laser Flash	3.0 wt%	2.00	Kim et al.[234]
Graphene – multilayer graphene	Liquid-phase-exfoliation	Epoxy	Laser Flash	10.0 vol%	23.00	Shahil et al.[210, 235]
1-pyrenebutyric acid functionalized graphene flakes	Exfoliation from graphite and non-covalent functionalization	Epoxy	Laser Flash	10 wt%	7.65	Song et al.[207]
Silica coated functionalized graphene	Graphene oxide reduction and funtionalization	Epoxy	Modified Transient Plane Source	8.0 wt%	1.72	Pu et al.[236]
Graphene – metal	Density gradient ultra-centrifugation	Epoxy	Transient Plane Source	5.0 vol%	5.00	Goyal et al.[208]
MLG	--	Epoxy	ASTM	11.8 wt%	166.70 ‖	Li et al.[237]
CNTs + GNPs	Thermal exfoliation and graphite oxide reduction	Epoxy	Laser Flash	20.0 vol% CNTs 20.0 vol% GNPs	38.00	Huang et al.[211]

Filler – Matrix	Filler Synthesis Method	Matrix	Measurement Method	Loading of Filler	(K_{eff}/K_m)	Authors
GS	--	Epoxy	Finite Element Method	10.00 vol%	24.00	Mortazavi et al.[215]
Single-layer graphene nanosheets	Exfoliated graphite oxide reduction aided by a surfactant	Polystyrene	Laser Flash	2.0 wt%	2.60	Fang et al.[122]
Functionalized graphene oxide (FGO)	Reaction of GO with vinyl trimethoxy silane	Silicone polymer	Transient Plane Source	0.5 wt%	1.78	Ma et al.[238]
Ionic liquid modified graphene	Reduction of GO and non-covalent functionalization	Polyurethane	Transient Plane Source	0.6 wt%	1.34	Ma et al.[239]
Graphene	Thermal exfoliation of graphite	1-octadecanol	Heat Conduction	4.0 wt%	2.50	Yavari et al.[240]
Copper oxide decorated hydrogen induced exfoliated graphene	--	Deionized water	Transient Line Source	0.05 wt%	1.28	Baby et al.[241]
Graphene	Graphene oxide reduction	Poly (vinylidene fluoride)	Laser Flash	0.5 wt%	2.00	Jinhong et al.[242]
Exfoliated graphene	Exfoliation of graphite oxide	Polypropylene	Laser Flash	2.2 vol%	2.00	Song et al.[232]
Graphene	--	Aluminum/ Teflon	Laser Flash	10.0 wt%	1.98	Kappagantula et al.[233]

Filler – Matrix	Filler Synthesis Method	Matrix	Measurement Method	Loading of Filler	(K_{eff}/K_m)	Authors
Exfoliated GNP	Exfoliation of acid intercalated graphite	High density polyethylene	Heat Flow Meter	15.0 vol%	3.00	Jiang et al.[243]
Functionalized GO	Exfoliation of graphite and functionalization	Polyimide		10.0 wt%	6.23	Tseng et al.[244]
Graphene	Exfoliation of graphite and thermal expansion	Polyimide		2.4 wt%	1.17	Koo et al.[245]
GNP	--	Paraffin	Transient Hot-wire	5.0 wt%	2.64	Fan et al.[246]
MLG	--	Paraffin	Transient Plane Source	20.0 vol%	28.00	Warzoha et al.[247]
GNP	--	Polyaniline	Steady-state	50.0 wt%	6.60	Abad et al.[248]
Ionic liquid modified graphene oxide	Graphite oxide oxidation	Bromobutyl rubber	Quickline-10 Test	4.0 wt%	1.30	Xiong et al.[249]
4-phenylbutylamine functionalized GS	Hummers method and functionalization	Polyimide	Laser Flash	3.0 wt%	3.34	Heo et al.[250]
Graphene	--	Stearic acid	Hot Disk Thermal Analyzer	5.0 wt%	2.07	Li et al.[251]
Thermally reduced GO	Modified Hummers method	n-eicosane/silica	Hot-wire	1.0 wt%	2.93	Wang et al.[252]
GS functionalized with	--	Octane	Non-equilibrium MD	--	3.13 ∥ 2.18 ⊥	Our work

Filler – Matrix	Filler Synthesis Method	Matrix	Measurement Method	Loading of Filler	(K_{eff}/K_m)	Authors
alkane chains						
GS	--	Polyamide-6,6	Non-equilibrium MD	--	1.6 – 9.0 ∥	Alaghemandi et al.[253]
GS	--	Polyamide-6,6	Non-equilibrium MD	--	3.70 ∥ 1.85 ⊥	Eslami et al.[254]
GS	--	Phenolic resin	Non-equilibrium MD	--	11.66 ∥	Hu et al.[209]
Functionalized GS	--	Octane	Monte Carlo Simulation	10.00 vol%	400 ∥ 1.00 ⊥	Our work

5.4 Conclusions

Graphene sheets (GS) belong to an interesting class of new materials that could be used to enhance the properties of polymeric nanocomposites. Recent technological advances are promising towards the production of large quantities of GS. Our simulation results, in some cases supported by experimental observations, suggest that it is possible to prevent the agglomeration of GS within organic matrixes by appropriately functionalizing the GS. We also found that this functionalization may be useful in abating the barriers typically encountered by heat when it flows from one inclusion to the surrounding organic matrix. Thus, based on our calculations, it is possible that, by inducing the appearance of nematic phases within GS – based nanocomposites, materials with anisotropic properties such as thermal conductivity are obtained.

Because it is possible that functionalizing the GS has a detrimental effect on their exceptional intrinsic properties, i.e. exceptional thermal conductivity, future theoretical studies should determine what is the optimum degree of functionalization that contains the resistances to heat flow from the GS to surrounding organic matrixes while leaving unaffected the thermal conductivity within the GS.

Our calculations are so far restricted to rather small GS, short oils, and small systems. To better understand GS – based nanocomposites it is necessary to develop coarse-grained simulation models to explore larger, more relevant GS, and their phase diagrams within organic matrixes of technologically important polymers such as PMMA. One such model, used herein, uses as input values for the Kapitza resistance obtained from atomistic simulations to predict macroscopic thermal conductivities. The reliability of our model depends on the accuracy of the parameters obtained at the all-atom level. This model is also limited by the size of the computational domain that can be studied, and therefore by the size of the GS that can be considered within the material. When more complex models will become available, direct comparison between simulation predictions and experimental data will be possible, and it will also be feasible to use theoretical models to propose compositions for graphene – based nanocomposites in which both mechanical and transport properties are optimized.

6 Simulation Insights for Graphene-based Water Desalination Membranes

The material presented below was published in 2013 in volume 29, issue 38, and page 11884 of the ACS journal Langmuir.

6.1 Introduction

Molecular dynamics simulations were employed to study the transport of water and ions through pores created on the basal plane of one graphene sheet (GS). Graphene pore diameters ranged from 7.5 to 14.5 Å. Different pore functionalities (COO^-, NH_3^+ and OH) were considered, obtained by tethering various functional groups to the terminal carbon atoms. The ease of ion and water translocation across the pores was monitored by calculating the potential of mean force along the direction perpendicular to the GS pore. The results are explained in terms of hydration structure for the ions across the membrane, as well as of appropriate density profiles. Comparison with available data for the PMFs across similar CNT pores is also discussed.

6.2 Simulation Method

In Fig. 6.1 (top panel) we show a schematic representation of the simulation box used in this study. The model GS membrane (56.58 Å X 55.38 Å), with a pore in its center, was placed parallel to the XY plane at the center of the simulation box. The pore diameter (Ø) was of ~ 14.5, 10.5, or 7.5 Å, obtained by removing carbon atoms, as necessary. The membrane was surrounded by 20 Å of water along the Z direction on both sides.

Periodic boundary conditions were employed to maintain a continuous two-dimensional membrane.

In the middle panel of Fig. 6.1 the three pore sizes (14.5, 10.5, and 7.5 Å) are shown. Three types of functional groups (carboxyl anion COO^-, amine cation NH_3^+, and hydroxyl OH) were grafted to the pore rim (bottom panel of Fig. 6.1). Note that, because of steric constraints, the functional groups in our GS pores point towards the center of the pore. The diameter of the pore changes depending on the size of the functional groups grafted to it. The diameter of the functionalized pore is calculated as the distance between the ends of two opposite functional groups. The COO^- and NH_3^+ groups are grafted to the 14.5 Å diameter pore, yielding pores of diameter ~ 10.0 and 11.0 Å, respectively. The OH group is grafted to the 10.5 Å pore, yielding a pore of diameter ~ 7.5 Å. In each functionalized pore six functional groups were spread uniformly around the rim of the GS pore. When charged functional groups were used, six counter-ions were added to maintain the electro neutrality of the system. These counter ions were placed far from the pore, and maintained fixed during the course of the simulations. This prevented the ions from accumulating near the functional groups, affecting the results. Care was taken so that these ions did not introduce artificial dipole moments. Although these ions were not allowed to move, additional ions included in the system to control the ionic strength were allowed to move according to the equations of motion.

Sodium ions (Na^+) and chloride ions (Cl^-) were randomly placed within the simulation box to yield a concentration of either 0.025 or 0.25 M. At 0.025 M, there were only one Na^+ and one Cl^- in the system (infinite dilution, within the limits of our simulation box).

At 0.25 M, 18 Na^+ and Cl^- ion pairs were present. Additional simulation results obtained at 0.6 M are also presented. These ions were allowed to freely move within the simulation box. The number of water molecules was maintained constant at 4100.

Carbon atoms in the GS were held stationary and modeled as LJ spheres using the parameters proposed by Cheng and Steele.[255] As a first approximation, the carbon atoms on the GS pore rims were modeled as the other carbon atoms on a GS, although they are intended to be terminated by hydrogen atoms, unless they are functionalized. The functional groups on the GS pores were not rigid. Instead they were modeled using the flexible Optimized Potentials for Liquid Simulations (OPLS) force field parameters proposed by Jorgensen et al.[204] Water molecules were modeled using the non-polarizable, rigid point charge extended (SPC/E) model[256] because of its simplicity, reliability in reproducing water structure and dynamics, and because of the availability of ion-water potentials specifically parameterized for SPC/E water.[257] Recent work[258] suggests that polarization effects are not significant in monovalent salt solutions since the field associated with monovalent ions does not significantly perturbs the water molecules within the hydration shell. However, considering the polarizability of graphene might affect the structure of aqueous ionic systems at the solid-liquid interface.[259] In Table 6.1 we report the force field parameters implemented in our simulations.

Bond lengths and angles in water molecules were fixed using the SHAKE algorithm.[260-261] Non-bonded interactions were modeled by means of dispersive and electrostatic forces. Van der Waals interactions were treated according to the 12-6 Lennard-Jones (LJ) potential.[262] The LJ parameters for unlike interactions were obtained using the

Lorentz-Berthelot mixing rules from pure component ones. The cutoff for Van der Waals interactions was set to 10 Å; that for electrostatic interactions to 9 Å. Corrections to long-range electrostatic interactions were calculated using the particle mesh Ewald (PME) summation technique.

All the simulations were carried out at 300K with a timestep of 2 fs, using the simulation package GROMACS 4.5.5.[263-266] All the systems were first equilibrated for 2 ns in the NPT ensemble to replicate ambient conditions. For simulation results obtained at high pressure, we refer the interested reader to the recent contribution by Cohen-Tanugi and Grossman.[168]

After equilibration, to determine the free energy barrier for ion/water permeation through the pore, the umbrella-sampling algorithm[267-268] was implemented (detailed description of the method is given in section 8.1 of Appendix). In short, a harmonic biasing potential $K_z(z\text{-}z_i)^2/2$, where z is the axial coordinate of the ion defined from the center of the pore, z_i is the target position, and K_z is the force constant (ranging from 30 to 100 kcal/mol nm^2), was applied to the target species (Na^+, Cl^-, or water). The target positions varied from z = 20 to z = -20 Å in increments of 1 Å. This resulted in 41 simulations yielding overlapping windows of density probability. Each window was sampled for 4 ns. The last 3 ns of data were analyzed using the weighted histogram analysis method (WHAM).[267, 269-270]

Table 6-1 The Lennard Jones and force field parameters considered in this work.

The Lennard Jones parameters and partial charges for the ions, water molecules, carbon atoms in GS, and functional groups.

Atom	σ/Å	ε/kJmol^{-1}	*q/e*
Ions			
Na^+	2.583	0.4184	1.000
Cl^-	4.401	0.4184	-1.000
Water			
OW	3.166	0.6502	-0.8476
HW	0.000	0.0000	0.4238
GS			
C	3.400	0.2330	0.000
COO^-			
C (GS)	3.400	0.2330	0.100
C (FG)	3.750	0.4600	0.700
O (C=O)	2.960	0.8792	-0.800
O (C – O^-)	2.960	0.8792	-1.000
NH_3^+			
C (GS)	3.400	0.2330	0.300
N	3.250	0.7117	-0.300
H	0.000	0.0000	0.330
OH			
C (GS)	3.400	0.2330	0.265
O	3.070	0.7117	-0.700
H	0.000	0.0000	0.435

Force field parameters for the functional groups of GS

Bond stretching potential

$$V(r) = \frac{K_r}{2}(r - b_{eq})^2$$

	Bond type	K_r/kJmol^{-1}Å^{-2}	b_{eq}/Å
COO^-			
	C (GS) – C (FG)	3927.20	1.41
	C (FG) – O (C=O)	4772.93	1.22
	C (FG) – O (C – O^-)	5493.05	1.25
NH_3^+			
	C (GS) – N	4027.70	1.34
	N – H	3634.14	1.01
OH			
	C (GS) – O	3767.76	1.36
	O – H	4625.28	0.96

Bond bending potential

$$V(\theta) = \frac{K_\theta}{2}(\theta - \theta_{eq})^2$$

	Angle type	K_θ/kJmol^{-1}rad^{-2}	θ_{eq}/°
COO^-			
	C (GS) – C (GS) – C (FG)	586.15	120.0
	C (GS) – C (FG) – O (C=O)	669.88	120.4
	C (GS) – C (FG) – O (C – O^-)	544.28	117.0
	O (C=O) – C (FG) – O (C – O^-)	669.88	126.0
NH_3^+			
	C (GS) – C (GS) – N	586.15	120.1
	C (GS) – N – H	293.07	111.0
	H – N – H	365.09	106.4
OH			

C (GS) – C (GS) – O	585.48	120.0
C (GS) – O – H	292.74	113.0

Torsional potential

$$V(\phi) = \frac{1}{2}[V_1(1 + cos\phi) + V_2(1 - cos2\phi) + V_3(1 + cos3\phi) + V_4(1 - cos4\phi)]$$

Torsion type	V_1/kJmol^{-1}	V_2/kJmol^{-1}	V_3/kJmol^{-1}	V_4/kJmol
COO^-				
C (GS) – C (GS) – C (FG) – O (C=O)	-3.4330	1.7165	0.0	0.0
C (GS) – C (GS) – C (FG) – O (C – O^-)	-3.4330	1.7165	0.0	0.0
NH_3^+				
C (GS) – C (GS) – N – H	0.00	8.4990	0.0	0.0
OH				
C (GS) – C (GS) – O – H	-28.1364	14.0682	0.0	0.0

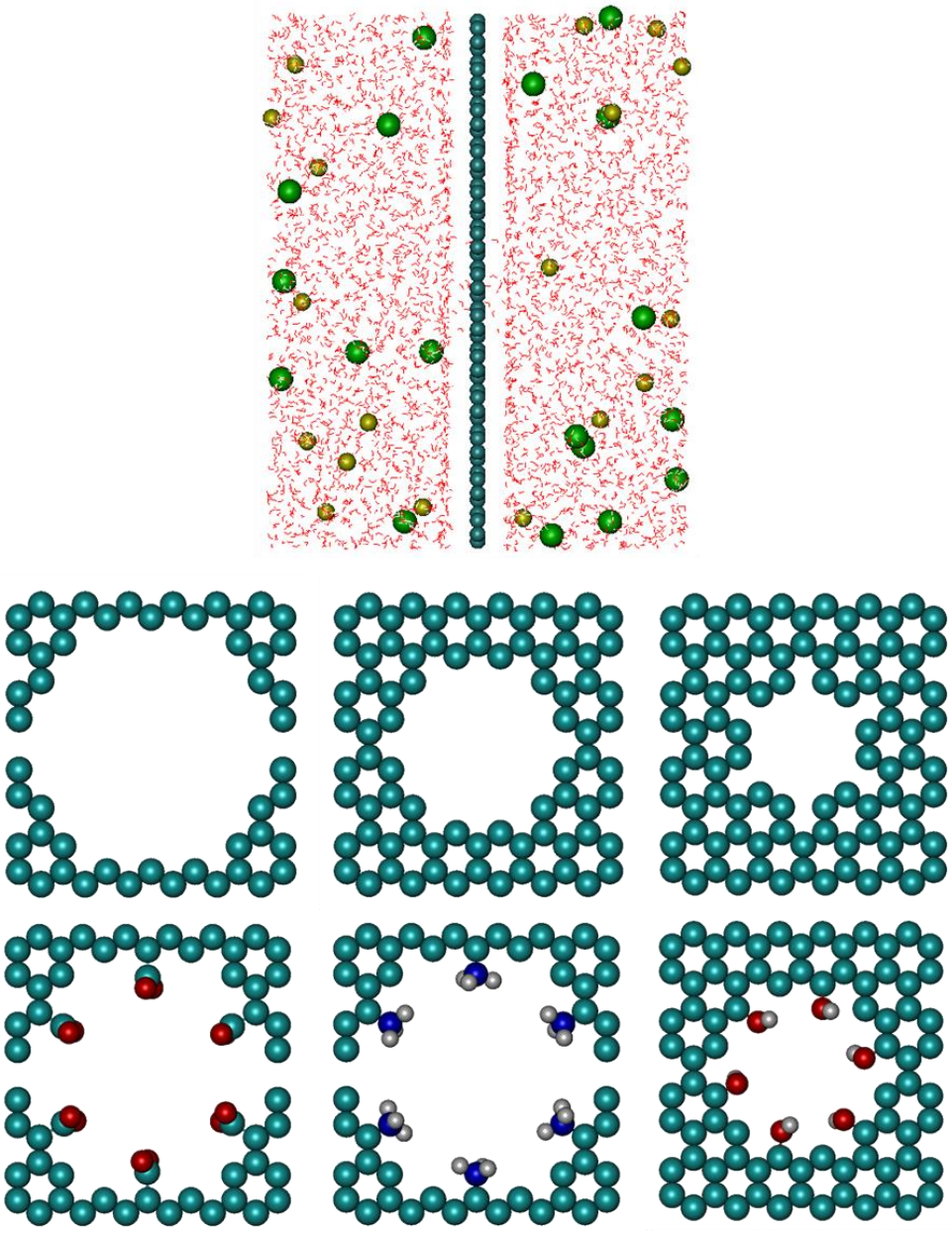

Figure 6-1 *Top panel*: Lateral view of the system simulated herein, showing the GS membrane at the box center and an aqueous 0.25 M NaCl solution that extends for 20 Å on both sides of the GS. *Middle panels*: top view of the three pristine GS pores considered, with pore diameter (from left to right) 14.5, 10.5, and 7.5 Å. *Bottom panels*: Top view of three GS pores functionalized with, from left to right, 6 COO^- (Ø = 10.0 Å), 6 NH_3^+(Ø = 11.0 Å), and 6 OH (Ø = 7.5 Å) groups. In these figures GS carbon atoms are shown as cyan spheres, oxygen in red, hydrogen in white, and nitrogen in blue. Yellow and green spheres represent sodium and chloride ions, respectively. Water is shown in the wireframe representation.

6.3 Results and Discussion

6.3.1 Pristine GS Pores

To monitor the likelihood of ion and water exclusion through the GS membrane, the potential of mean force (PMF) was calculated in the direction perpendicular to the membrane, as described in the methods section. The PMF was calculated when a molecule (one Na^+ or Cl^- ions, or one water molecule) was forced to move from the bulk region (z = 20 Å), through the center of each pore (z = 0 Å), to the bulk region (z = -20 Å) (from right to left in the schematic of Fig. 6.1). The resultant PMF is one-dimensional. The values obtained at each position are referred to that obtained in the bulk. A positive PMF is indicative of a free-energy barrier that needs to be overcome by the molecule of interest traveling across the pore. The higher the barrier, the more difficult it will be for a molecule to overcome it. PMF minima identify preferential positions assumed by the molecule of interest at equilibrium. The more negative the PMF, the more likely it will be to observe the molecule of interest at that location.

In Fig. 6.2 we report PMF results for Na^+ (left) and Cl^- (right) ions in 0.025 (top) and 0.25 M (bottom) NaCl solutions across the non-functionalized (pristine) GS pores. Data are reported for ions across the 14.5 (black continuous line), 10.5 (red dashed line), and 7.5 Å (black dashed line) pores. From Fig. 6.2, we can observe that the ionic concentration has little effect on the PMF of ions across the pristine GS pores. PMF profiles suggest that both Na^+ and Cl^- ions can diffuse through the pristine 14.5 Å pore (black line) without the need of overcoming significant free-energy barriers, indicating that this pore will not be efficient in water desalination. As the pore diameter decreases,

the PMF profiles show more pronounced maxima, which depend on the ion type. Explicitly, the maximum PMF values encountered by Na^+ and Cl^- ions as they diffuse through the pristine 10.5 Å pore are ~ 4.0 and ~ 5.0 kcal/mol, respectively. The energy barrier is higher for the Cl^- ion probably because of its bigger size compared to Na^+. When the pore diameter is further reduced to 7.5 Å (black dashed line), the PMF maxima obtained for Na^+ and Cl^- ions increase to ~14 and ~10 kcal/mol, respectively. The fact that the larger PMF barrier is not encountered for the larger ion suggests that not only the ion size (the diameters of Na^+ and Cl^- are 2.58 and 4.40 Å, respectively), but also the ions hydration structure (discussed later) might affect the free energy profile. Structural changes within the hydration shell as the ions approach the pores might also be responsible for the fact that the PMF profiles (especially the ones obtained in the 10.5 and 7.5 Å pores) in general do not show a monotonic increase as the distance from the pore center decreases. It should at this point be mentioned that the PMF barriers shown in Fig. 6.2 are consistent with those reported by Corry et al.,[160] who calculated the PMF for ions diffusing through CNTs of diameter ranging from 6.6 to 10.9 Å. Using the transition state theory we can estimate the diffusion coefficients for the ions across the pores from the PMF profile.[271] Such estimates suggest that the 14.5 Å pores do not hinder ionic diffusion compared to ions in bulk aqueous solutions, while the 7.5 Å pores reduce the ions mobility by several orders of magnitude. Qualitatively, these results suggest that GS membranes with pristine pores can be effectively used in water desalination only when the pores are rather narrow (7.5 Å out of the three pores considered here).

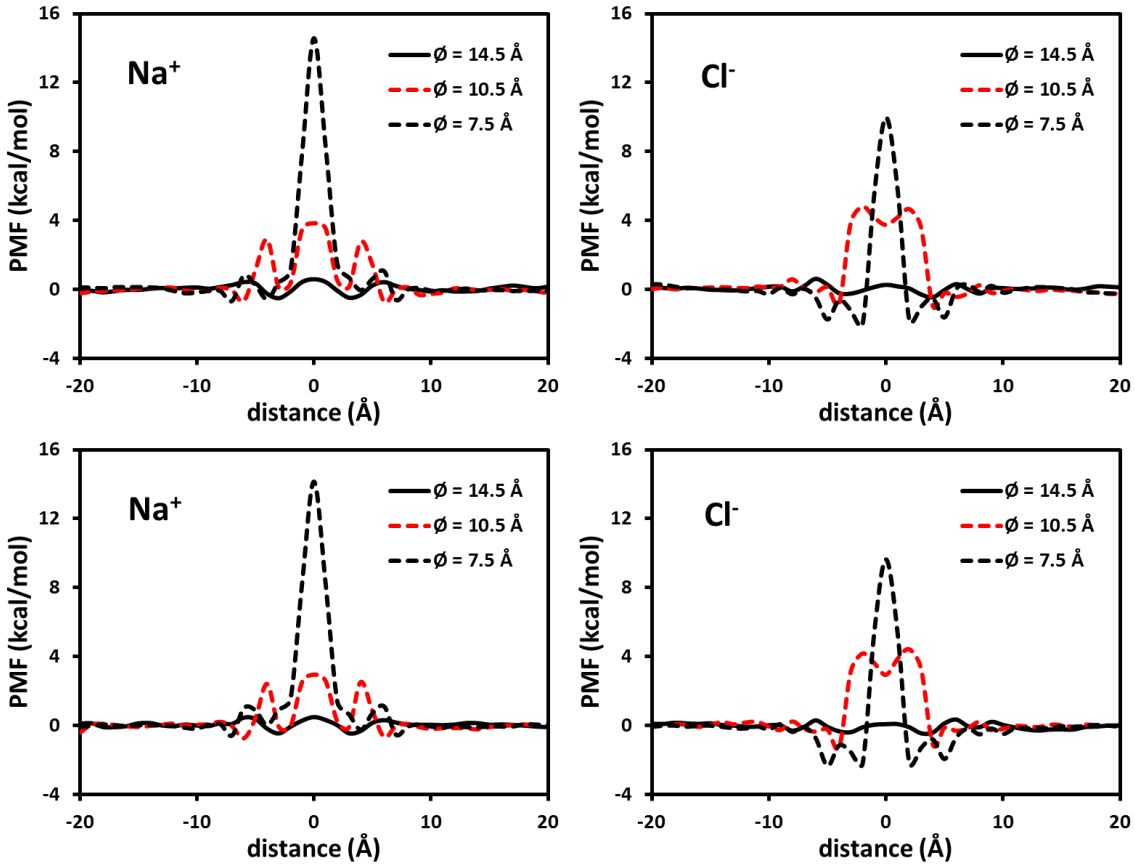

Figure 6-2 One-dimensional potential of mean force profiles obtained along the direction perpendicular to the GS pores for Na^+ (left) and Cl^- (right) ions in 0.025 (top) and 0.25 M (bottom) NaCl solutions. Pristine GS pores of diameter 14.5 (black continuous line), 10.5 (red dashed line), and 7.5 Å (black dashed line) are considered.

In Fig. 6.3 we show plots of atomic density profiles of oxygen (red line) and hydrogen (blue line) atoms of water molecules obtained along the direction perpendicular to the pristine GS pores at 0.025 M NaCl. The density profiles were calculated within a cylinder centered on the pore center with axis perpendicular to the GS. The diameter of the cylinder was equal to the diameter of the pore. Results are reported for pores of diameter 14.5, 10.5, and 7.5 Å (from top to bottom). The results are compared to the PMF profiles (dashed gray line) of Na^+ (left) and Cl^- (right) ions. The density profiles

for oxygen and hydrogen atoms show the formation of two atomic layers on either side of the pores, with peak positions varying with the diameter of the pores. Our results suggest that the structure of water near the pores is related to the PMF profiles (e.g., in some cases the minima and maxima in the atomic density profiles of oxygen match the positions of maxima and minima in the PMF profiles). These qualitative observations suggest that Na^+ and Cl^- ions preferentially partition within or in between water, perhaps to maintain their hydration shell.

Although it is important for a RO membrane to reject salt ions, it is equally important that water molecules can diffuse through the membranes. In Fig. 6.4 we report the PMF profiles as experienced by one water molecule as it diffuses through the pristine pores of Fig. 6.1 in an aqueous solution of 0.025 (left) and 0.25 M NaCl (right). There is no significant difference in the PMF profiles of water molecule obtained in 0.025 and 0.25 M solutions, except at the center of the pore, where the PMF minima are a little more pronounced at 0.25 M. The PMF for the 14.5 Å pore (black continuous line) indicates that water passes through the pore without any significant energy barrier (PMF maximum ~ 0.5 kcal/mol). For the 10.5 Å pore, water faces an energy barrier of ~ 6.5 kcal/mol to pass through the center of the pore (red dashed line), which is larger than the energy barrier encountered by Na^+ and Cl^- ions (discussed in Fig. 6.2). These results suggest that the 10.5 Å pore will not be effective in desalinating water. For the 7.5 Å pore (black dashed line), the energy barrier for water passage is ~ 5.0 kcal/mol at 3 Å away from the pore, although the PMF is ~ -9.0 kcal/mol at the center of the pore. The maximum PMF of water is much lower than the PMF maxima of Na^+ and Cl^- ions

(discussed in Fig. 6.2), indicating that the 7.5 Å pore will be effective for water desalination.

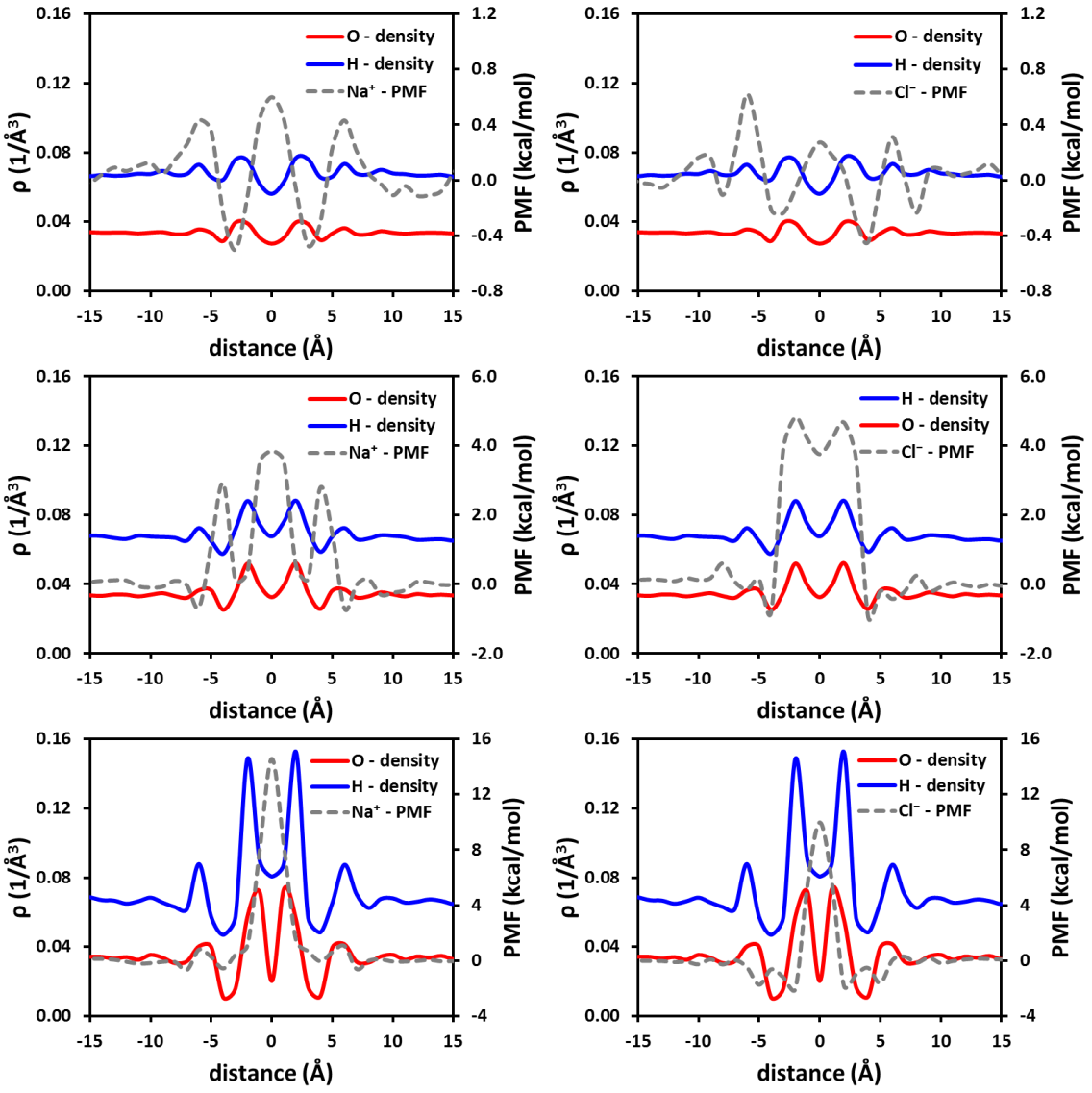

Figure 6-3 Atomic density profiles of oxygen (red) and hydrogen (blue) atoms of water within a cylinder centered on the pore center whose diameter equals the pore diameter. Three pores are considered with diameter (from top to bottom) 14.5, 10.5, and 7.5 Å. For comparison, traces of the PMF obtained for Na^+ (left) and Cl^- (right) ions are also reported (dashed lines). Results obtained at 0.025 M are shown here.

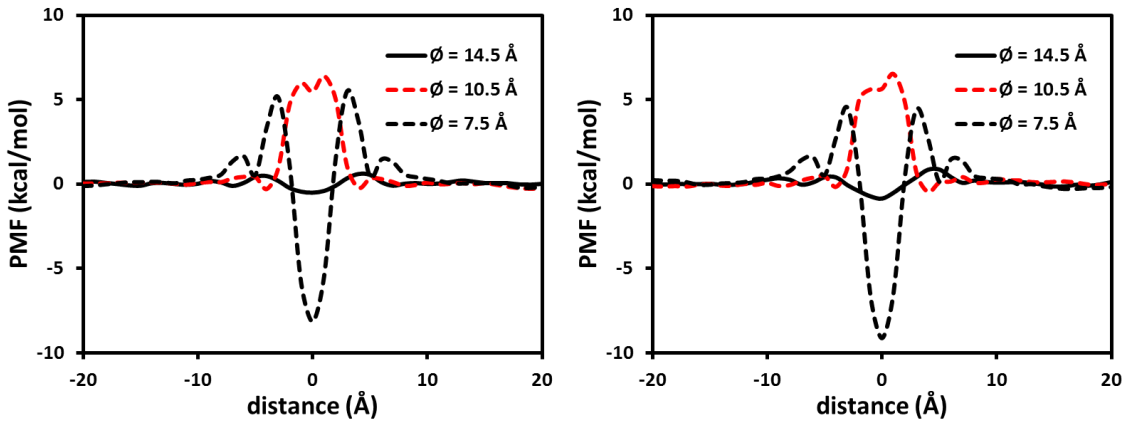

Figure 6-4 Potential of mean force for one water molecule as a function of its axial distance from the center of the pristine GS pores. The water-pore distance is measured from the center of the water molecule. The aqueous solution is maintained at 0.025 (left) and 0.25 M (right) NaCl concentration. Three pores are considered, with diameter 14.5 (black continuous line), 10.5 (red dashed line), and 7.5 Å (black dashed line) respectively.

As in the case of ions, the PMF profiles of water in general do not show a monotonic increase as the distance from the pore center decreases. This is because the structure of water molecules near the pore is significantly different from that of water molecules in the bulk region. The atomic density profiles of oxygen atoms of water with the PMF of water obtained along the direction perpendicular to the pristine GS pores at 0.025 M NaCl are plotted in the left panels of Fig. 6.5. Results are reported for pores of diameter (from top to bottom) 14.5, 10.5, and 7.5 Å, respectively. The oscillations in the PMF are consistent with the peaks in the density profile for the 14.5 Å pore. Whenever there is a minimum in the density profile, we observe a maximum in the PMF. In the right panels of Fig. 6.5, we show the planar density distribution for the oxygen atoms of water molecules inside these pores. In this calculation we only consider the water molecules whose oxygen atoms belong to a slab of thickness ΔZ = 3.4 Å centered on the GS membrane. From the planar density distribution of oxygen, we can observe that the

water molecules yield hexagonal chains inside the pore, and that water is present at the center of the 14.5 Å pore. These density distributions explain, qualitatively, the lack of PMF barrier as one water molecule translocates across this pore (black line in Fig. 6.4).

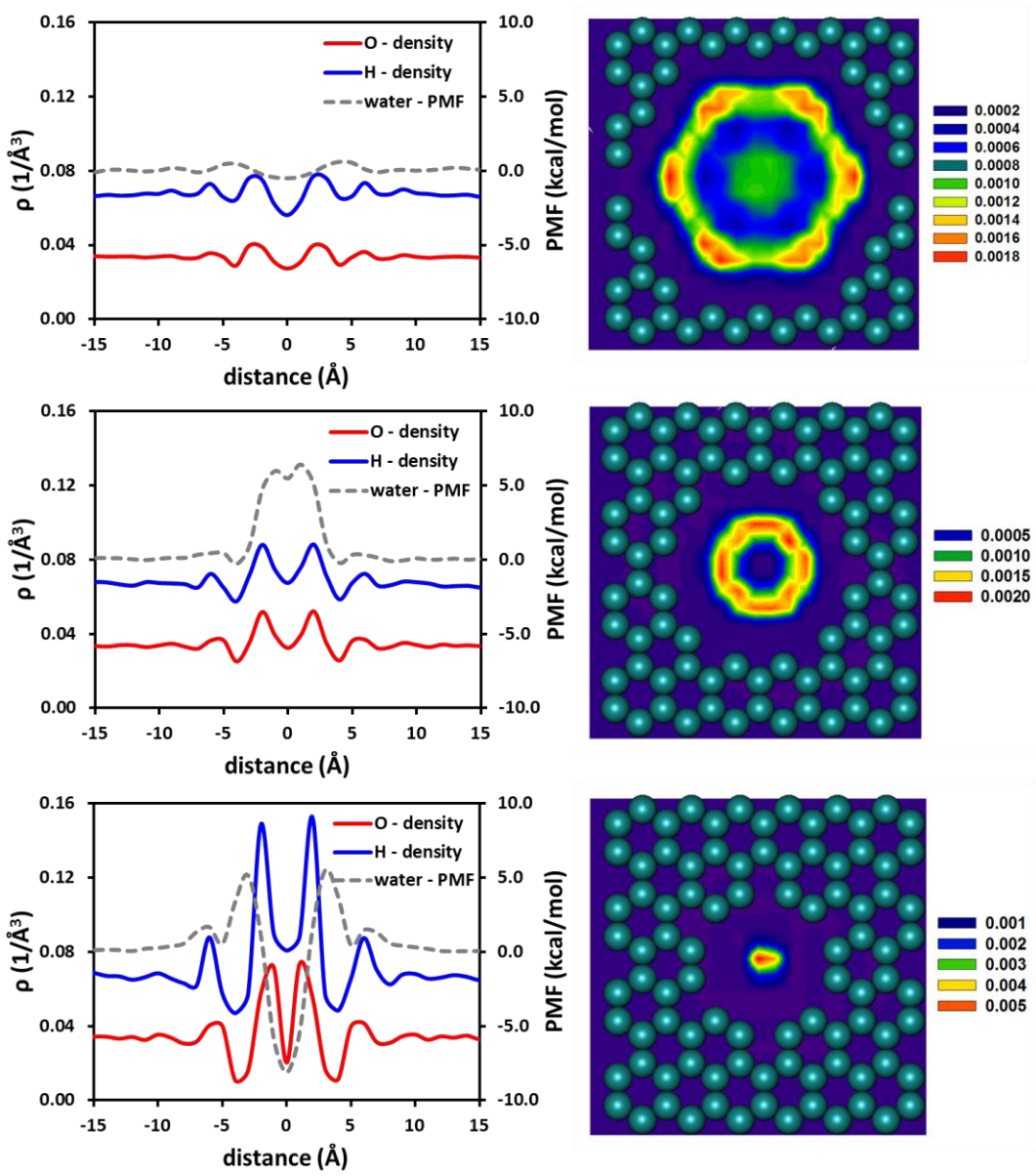

Figure 6-5 Left: Atomic density profiles of oxygen (red) and hydrogen (blue) atoms of water obtained within a cylinder of diameter equal to the pore diameter and perpendicular to the GS, together with the trace of the PMF experienced by water molecules across the pore (dashed lines). Right: Planar oxygen density distribution inside the GS pores. The units of the atomic density are $Å^{-3}$. The aqueous solution is maintained at 0.025 M NaCl concentration. Three pores are considered, with diameter (from top to bottom) 14.5, 10.5, and 7.5 Å.

When the pore diameter is reduced to 10.5 Å, the water density profile is not consistent with the PMF profile. The planar oxygen density distribution within the pore (right

panel) shows that water molecules form a circular chain inside the pore, and that no water molecule is present at the center of the pore. These results suggest that water molecules cannot readily occupy the center of the pore, explaining the large PMF barrier of ~ 6.5 kcal/mol shown in Fig. 6.4. When the Cl^- ion passes through the center of this pore we observed no water inside the pore because of the bigger size of the Cl^- ion. This explains the mismatch between the density profiles and the PMF of Cl^- ion (discussed in Fig. 6.3).

When the pore diameter is further reduced to 7.5 Å, the oxygen density profile shows the formation of two atomic layers on either side of the pore, consistent with the oscillations in the PMF profile. The maxima and minima in the PMF are observed when the water molecule is 3 Å away from the pore and at the center of the pore respectively. When the water molecule is 3 Å away from the pore, the density profile shows a minimum i.e., it is not a preferential equilibrium position. The water molecule experiences an energy barrier of ~ 5.0 kcal/mol at this distance. The planar oxygen density profile suggests that a single file movement can be established for water molecules inside this pore, and that water molecules preferentially reside at the center of the pore, where we observed a minimum in the PMF profile. It should be mentioned that the structure of water inside the pristine 10.5 and 7.5 Å GS pores agrees well with that predicted inside pristine 10.9 and 8.1 Å CNT.[160]

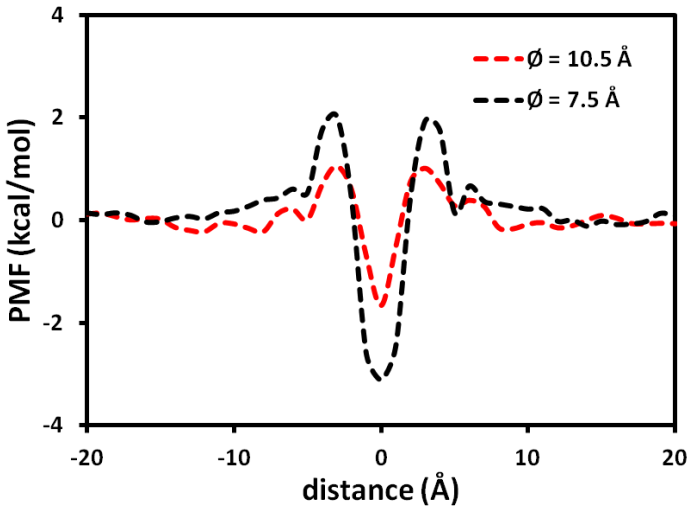

Figure 6-6 Potential of mean force for one water molecule as a function of its axial distance from the center of the pristine GS pores at 0.25 M NaCl concentration. Two pores are considered, with diameter 10.5 (red dashed line) and 7.5 Å (black dashed line) respectively. As opposed to results shown in figure 6.4, the results presented here are obtained when the reference water molecule was allowed to move in the directions X and Y parallel to the GS, while being constrained at fixed distances from the GS pore.

The simulations just discussed were conducted by constraining the reference water molecule within an axis perpendicular to the membrane through the center of the pore. We conducted additional simulations for water through the 10.5 and 7.5 Å pores in which the constraints imposed along the X and Y directions (parallel to the GS) were removed. The correspondent PMF results are reported in Fig. 6.6. As expected, the PMF profiles obtained when the water molecule is allowed to move along X and Y directions show less pronounced repulsive peaks, because water molecules will find preferential positions within the pores if allowed to. The main evidence for this occurs for the 10.5 Å pore, in which case the PMF is negative in the center of the pore when water can move along the X and Y directions, and positive when it is not (as shown in Fig. 6.4). When water is forced to stay at the center of the pore, it has to stay within a region of

low water density (see Fig. 6.5), while when it can move water will stay closer to the pore rim, where it can favorably interact with other water molecules.

6.3.2 Functionalized GS Pores

Based on both experimental and theoretical reports, summarized in the introduction, it is expected that more effective ions rejection can be achieved when carbon-based membranes are appropriately functionalized. The functionalized GS pores shown in the bottom panel of Fig. 6.1 are used for our calculations along this line of thought. Three functional groups were considered: carboxyl anion COO^-, amine cation NH_3^+, and hydroxyl OH. As mentioned above, each functionalized pore contains 6 functional groups. Because of geometric constraints, the effective pore diameter decreases upon functionalization. The effective pore diameter for the three functionalized pores differs, but not too much (see details in Fig. 6.1).

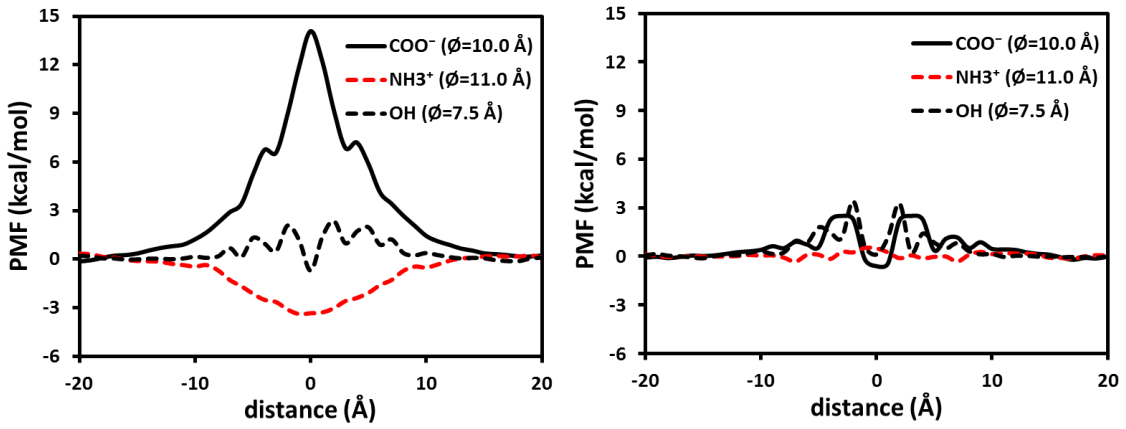

Figure 6-7 Potential of mean force for one water molecule as a function of its axial distance from the center of the functionalized GS pores. Results are shown for 0.025 (left) and 0.25 M (right) NaCl concentration at ambient conditions. Three pores are considered, functionalized with COO^- (black continuous line), NH_3^+ (red dashed line), and OH groups (black dashed line), respectively.

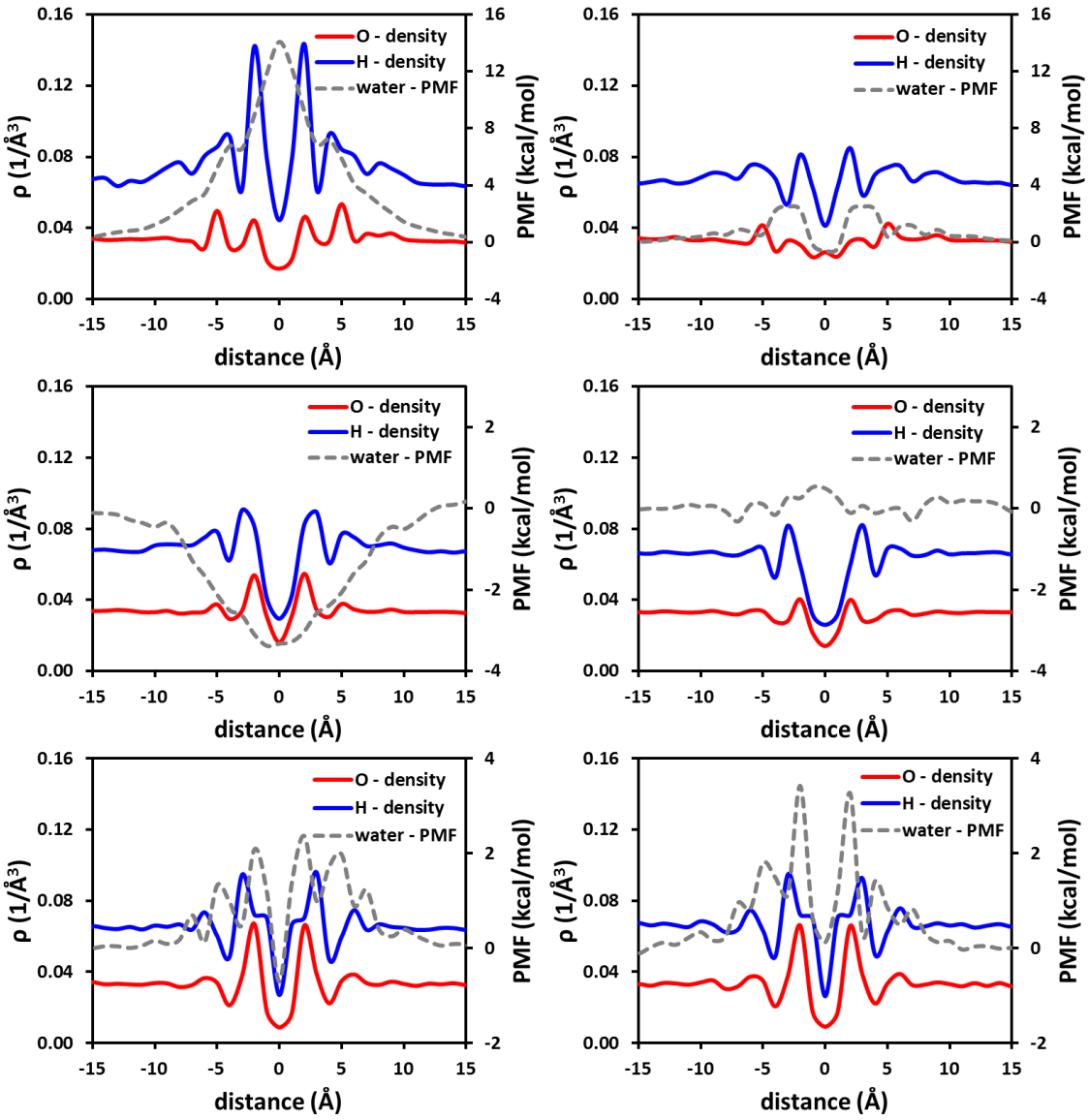

Figure 6-8 Atomic density profiles of oxygen (red) and hydrogen (blue) atoms of water within a cylinder of diameter equal to the pore diameter and perpendicular to the functionalized GS pores, together with the trace of PMF experienced by water molecules across the pore (dashed lines). Three pores are considered, functionalized with, from top to bottom, COO^-, NH_3^+, and OH groups. Data obtained at 0.025 (left) and 0.25 M (right) NaCl concentration are both shown.

In Fig. 6.7 we report the PMF profiles as experienced by one water molecule across the functionalized pores in a 0.025 (left) and 0.25 M (right) NaCl solutions. The results are shown for GS pores functionalized with COO^- (Ø = 10.0 Å), NH_3^+ (Ø = 11.0 Å), and

OH (Ø = 7.5 Å) groups. The PMF peaks depend on the functional group, and they do not always appear at the center of the pore. The results shown in Fig. 6.7 suggest that at infinite dilution (left panel) the water molecule is strongly repelled by the center of the COO^- pore (PMF ~ 14 kcal/mol), while it is attracted to the NH_3^+ pore (PMF ~ -3 kcal/mol). The PMF profiles obtained for OH functionalized pore show oscillations between 0 and 3 kcal/mol. As the ions concentration increases, the strong repulsion due to the COO^- groups and the pronounced attraction due to the NH_3^+ groups both disappear. These observations suggest that the features of the PMF profiles are due, to a large extent, to electrostatic effects, which are shielded at high salt concentration. However, the features of the PMF profiles also depend on the structure of water near the pore. In Fig. 6.8 we report the density of water within a cylinder centered in the pore center and perpendicular to the membrane in an aqueous solution of 0.025 (left) and 0.25 M (right) NaCl. Three pores are considered, functionalized with, from top to bottom, COO^-, NH_3^+, and OH groups. From the figure we observe that the maxima/minima in the PMF profile sometimes correspond to minima/maxima in the density profile.

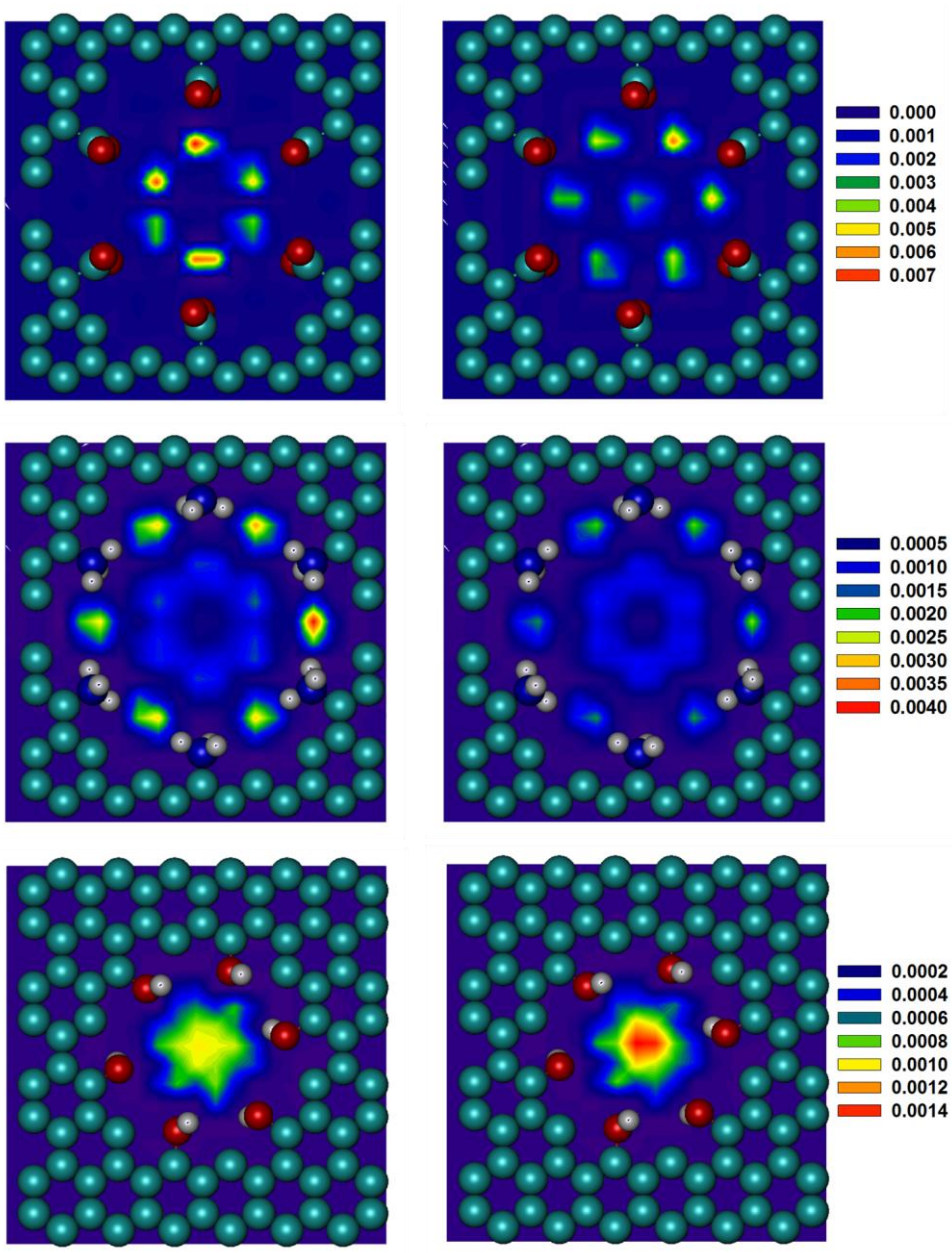

Figure 6-9 Planar density distribution of oxygen atoms of water inside the GS pores at 0.025 (left) and 0.25 M NaCl concentration (right). Results are reported for pores functionalized with, from top to bottom, COO^- (Ø = 10.0 Å), NH_3^+ (Ø = 11.0 Å), and OH groups (Ø = 7.5 Å). The units of the atomic density are $Å^{-3}$.

In Figure 6.9 we report the density maps for the oxygen atoms of water inside the functionalized GS pores at 0.025 (left) and 0.25 M (right) NaCl concentration. From top to bottom, the results are for COO^-, NH_3^+, and OH functional groups, respectively. At

0.025 M concentration, our results suggest that water molecules are not present at the center of the pores functionalized with either COO^- or NH_3^+ groups. Strong electrostatic interactions seem to dictate association between water and the functional groups. The situation is different when OH functional groups are considered. Within this pore water is found to accumulate near the pore center. It is likely that these structural differences are related to the differences observed in the PMF profiles when the results obtained for different functional groups are compared (Fig. 6.7). Our results suggest that increasing the ionic concentration causes changes in the structure of water within the pores (right panels of Fig. 6.9). The effects are more pronounced for the COO^- functional groups, but are still evident for the other functional groups considered. Inside the COO^- pore, the position of the water molecules changes due to the accumulation of Na^+ ions near the pore. Inside the NH_3^+ and OH pores, the accumulation of Cl^- and Na^+ ions causes a change in the intensity of the density distribution. The number of water molecules decreased inside the NH_3^+ pore while they increased inside the OH pore compared to that at 0.025 M. To visualize these effects we resort to visualization of representative simulation snapshots, reported in Fig. 6.10. We show ions and water near the pores functionalized with COO^- (left), NH_3^+ (middle) and OH (right) groups at 0.25 M salt concentration. From the snapshots, we can observe the accumulation of ions around the COO^-, NH_3^+, and OH groups, which screens electrostatic interactions.

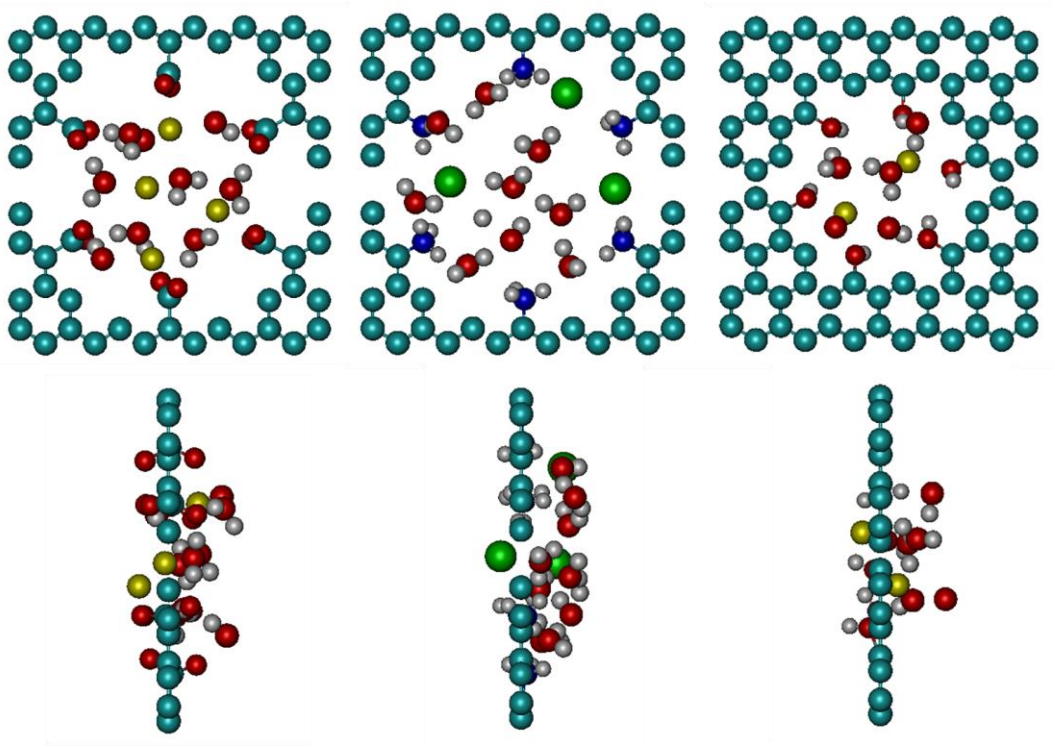

Figure 6-10 Top (top panel) and side view (bottom panel) of representative simulation snapshots showing the location of ions and water near the pore when a single water molecule (purple) is present at the center of the functionalized GS pores. Three pores are considered, functionalized with, from left to right, COO^-, NH_3^+, and OH groups, respectively. The color code is the same as that used in Figure 6.1.

Concluding the analysis of Fig. 6.7, our results suggest that water molecules do not experience a prohibitive free energy penalty as they diffuse across the functionalized pores at moderate ionic strength. In analyzing the PMF profiles experienced by ions across the functionalized pores we consider separately the pores functionalized with COO^-, NH_3^+, and OH groups; we compare the results to those obtained in the parent non-functionalized pores; we compare results obtained at infinite dilution (0.025 M) vs. moderate NaCl concentration (0.25 M); and we separately investigate the PMF profiles experienced by Na^+ and Cl^- ions.

In Fig. 6.11 we show the PMF results obtained for the pores functionalized with COO^- groups. At infinite dilution Na^+ ions are strongly attracted to the pore center (PMF ~ -18 kcal/mol) while Cl^- ones are strongly repelled (PMF ~ 46 kcal/mol). These values are particularly significant when compared to those obtained in the non-functionalized parent pores (gray lines), confirming that the functional groups are responsible. As the ionic strength increases, however, both minima and maxima in the PMF profiles (for Na^+ and Cl^- ions, respectively) decrease in intensity. This suggests that increasing the ionic strength screens the electrostatic forces responsible in large part for the results just discussed. In addition to electrostatic interactions, steric effects due to the packing of water molecules are responsible for the oscillations observed in the PMF profiles. Despite the screening of electrostatic interactions, our results suggest that functionalizing the GS pores with COO^- groups induces an effective free energy barrier of ~ 11 kcal/mol for Cl^- ions as they attempt to diffuse across the pore. In Fig. 6.12 we report the planar density distribution of Na^+ ions near the COO^- pore showing the accumulation of Na^+ ions within the COO^- functionalized pores at 0.25 M salt concentration. In Fig. 6.13 we show the results for the density distribution of water molecules within a cylinder centered in the pore center and perpendicular to the GS membrane. The results are shown together with the PMF of Na^+ (left) and Cl^- (right) ions across the COO^- functionalized pore in an aqueous solution of 0.025 (top) and 0.25 M (bottom) NaCl. The results from Fig. 6.12 and 6.13 show that multiple ions are attracted near the pore, which causes screening of electrostatic effects, and that the water structure is in some cases responsible for the non-monotonic behavior of the PMF profiles shown in Fig. 6.11.

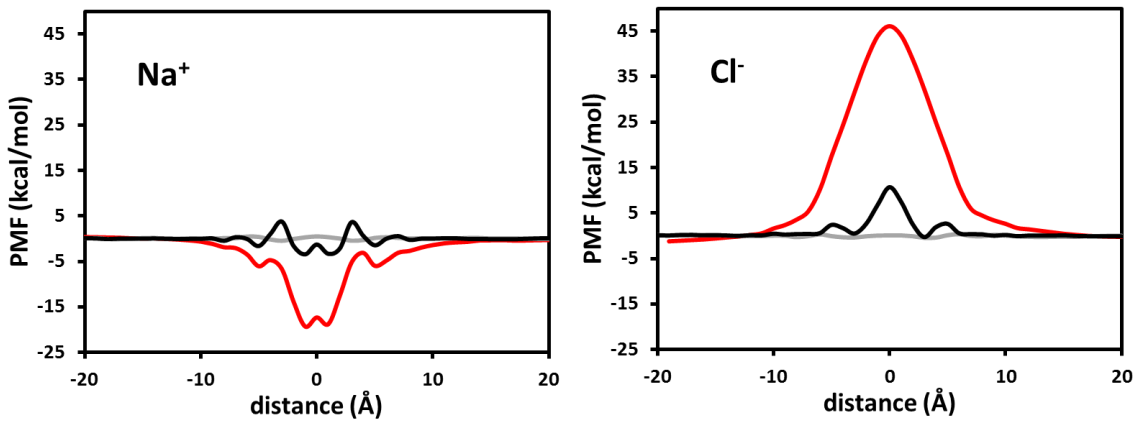

Figure 6-11 One-dimensional PMF along the direction perpendicular to the COO^- functionalized GS pores for Na^+ (left) and Cl^- (right) ions at 0.025 (red) and 0.25 M NaCl concentration (black). For comparison, the results obtained on the non-functionalized pore of diameter 14.5 Å at 0.25 M NaCl concentration are also shown in gray.

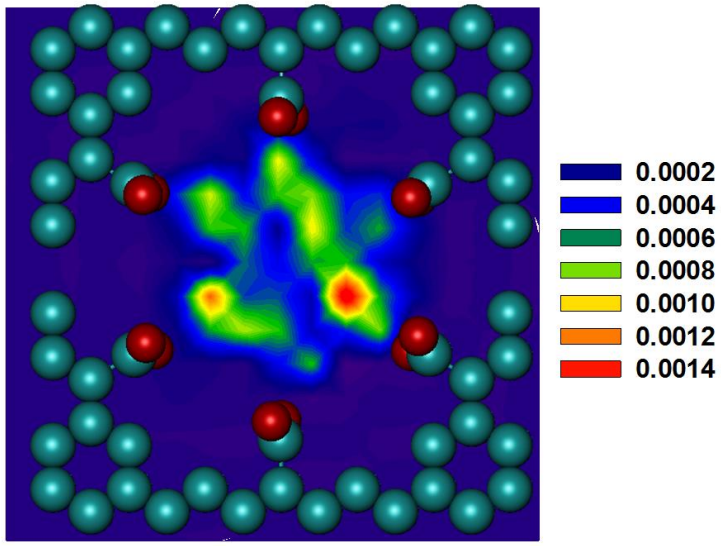

Figure 6-12 Planar density distribution for Na^+ ions near the COO^- functionalized pore at 0.25 M NaCl. The units of the atomic density distribution are $Å^{-3}$.

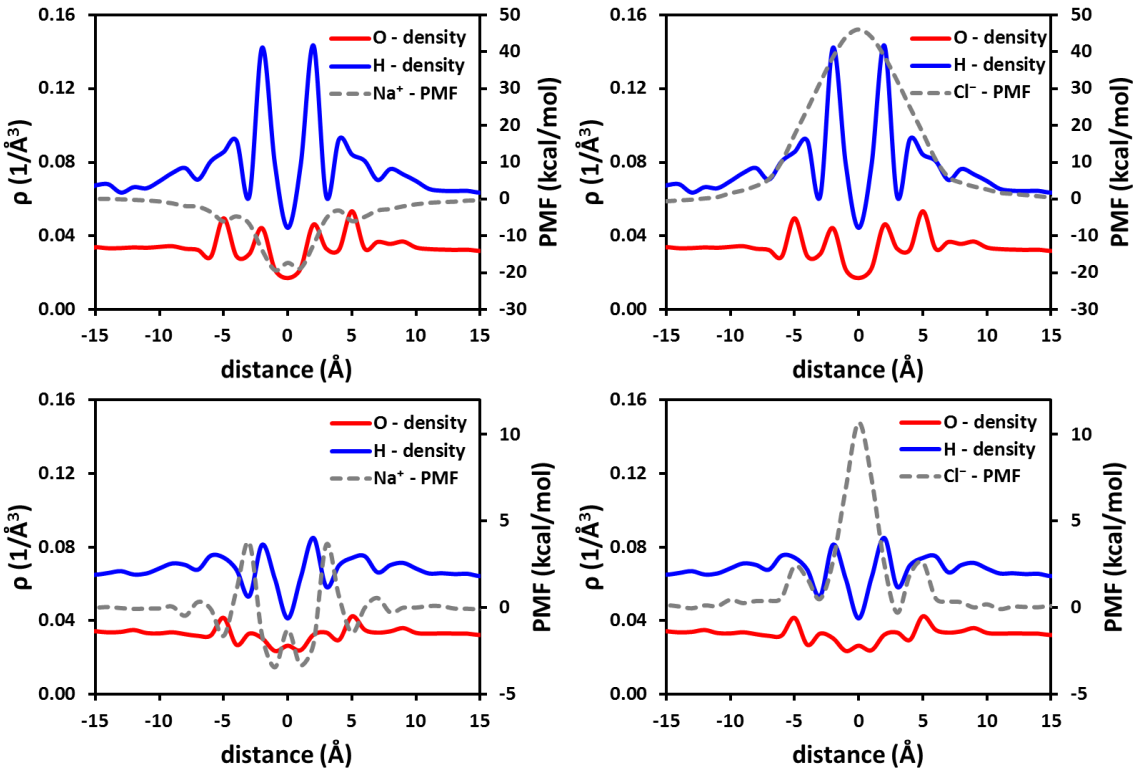

Figure 6-13 Atomic density profiles for oxygen and hydrogen atoms of water within a cylinder centered in the GS pore and perpendicular to the GS membrane. The results are shown together with the PMF results for Na^+ (left) and Cl^- (right) ions across the COO^- functionalized pore. Data obtained at 0.025 (top) and 0.25 M (bottom) NaCl concentration are both shown.

In Fig. 6.14 we report the PMF profiles obtained for Na^+ and Cl^- ions across the pores functionalized with NH_3^+. Because these groups are positively charged while COO^- are negatively charged, the PMF results are qualitatively opposite compared to those in Fig. 6.11. At infinite dilution Na^+ are repelled by the pores (PMF ~ 12 kcal/mol), while Cl^- ions are attracted to it (PMF ~ -20 kcal/mol). The structure of water near the pores is responsible for oscillations in the PMF profiles. Increasing the ionic strength has the effect of decreasing the intensity of the free energy peaks. For the scopes of the present Chapter (designing membranes for water desalination) it is important to point out that the PMF obtained for Na^+ and Cl^- ions are significantly reduced at moderate ionic

strength (less than 4 kcal/mol), suggesting that functionalizing GS pores with NH_3^+ groups may not be as effective as desired for repelling Na^+ and Cl^- ions. The accumulation of Cl^- ions near the pore entrance is responsible for these effects, as expected. In Fig. 6.15 and 6.16 we report results to quantify the density distribution of Cl^- ions near the functionalized pores at 0.25 M NaCl concentration, and the density profiles for water in the direction perpendicular to the surface. To confirm that electrostatic interactions are for the most part responsible for the results shown in Fig. 6.11 and 6.14, we decoupled dispersive and electrostatic pore-ion interactions as a function of ion-GS distance. The results are summarized in Fig. 6.17. In Fig. 6.17 we report the ion-pore potential energy as a function of the vertical distance from the center of the pore. We only consider pores functionalized with COO^- and NH_3^+ groups. In these calculations only the interactions between the ions and the functionalized GS membranes are considered. The dispersive interactions are considered from the LJ potentials. The electrostatic ones are obtained from Coulombic GS-ion interactions, neglecting long-range corrections. The results are obtained at 0.25 NaCl concentration, but are not dependent on salt concentration. From the figure we can observe that the electrostatic interactions dominate the dispersive interactions when the pores are functionalized with COO^- and NH_3^+ groups.

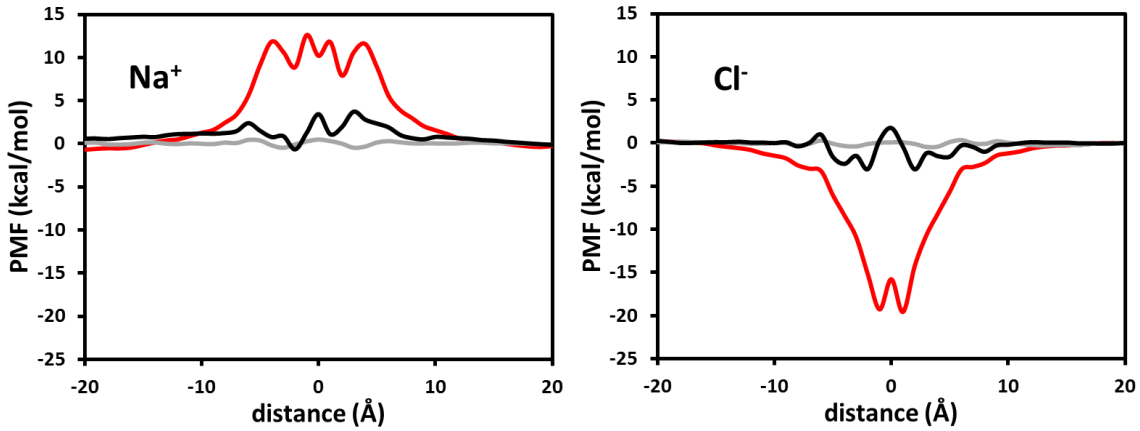

Figure 6-14 Same as Figure 6.11, but for pores functionalized with NH_3^+ groups.

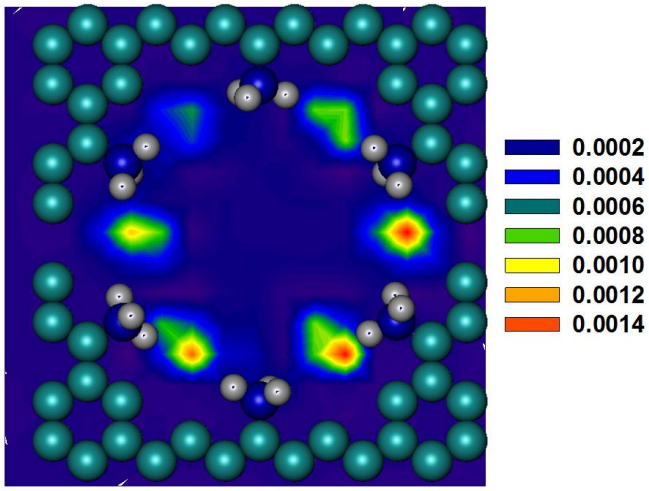

Figure 6-15 Planar density distribution for Cl^- ions near the NH_3^+ functionalized pore at 0.25 M NaCl. The units of the atomic density distribution are $Å^{-3}$.

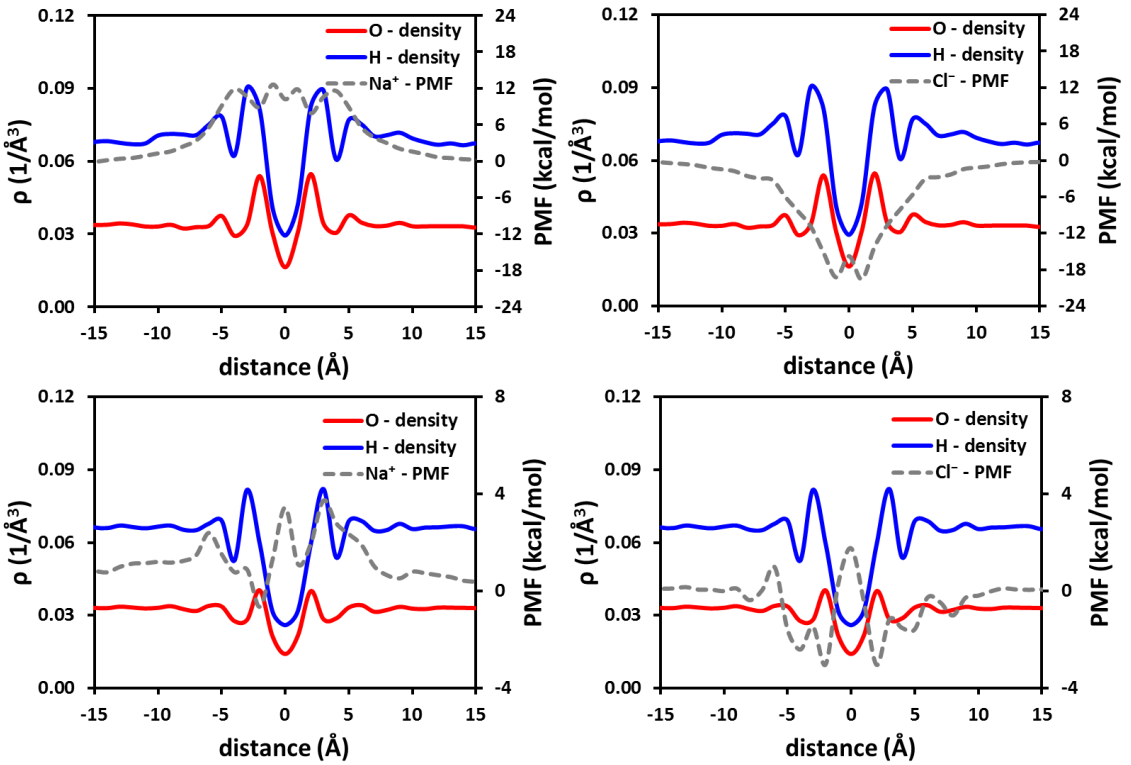

Figure 6-16 Atomic density profiles for oxygen and hydrogen atoms of water within a cylinder centered in the GS pore and perpendicular to the GS membrane. The results are shown together with the PMF results for Na^+ (left) and Cl^- (right) ions across the NH_3^+ functionalized pore. Data obtained at 0.025 (top) and 0.25 M (bottom) NaCl concentration are both shown.

In Fig. 6.18 we report the PMF profiles for Na^+ and Cl^- ions through the OH functionalized pore at 0.025 and 0.25 M NaCl. The results are compared to those obtained across the non-functionalized pore of diameter 10.5 Å. In the PMF for Na^+ (left) at infinite dilution, a repulsion is observed at 4 Å (~ 2.0 kcal/mol), and attraction at 2 Å (~ -7.0 kcal/mol), and repulsion at 0 Å (~ 2.0 kcal/mol). These effective repulsion peaks appear weak for desalination applications. The PMF profiles are qualitatively similar to those obtained for the non-functionalized pore, suggesting that the structure of water is in large part responsible for these results.

The PMF results for Cl^- (right), on the other hand, show a mild attraction at 3 Å (PMF ~ -4 kcal/mol) followed by a strong repulsion at the center of the pore (PMF ~ 19 kcal/mol). This repulsion is much stronger than that experienced across the pristine pore, suggesting that the functional groups are responsible for the results, possibly because of steric effects. When the concentration of NaCl is increased to 0.25 M, there is no significant change in the PMF profile of Na^+ ion, which is consistent with the absence of strong electrostatic interactions between the functional groups and the ions in solution. The PMF maximum for Cl^- decreases (to ~ 10.5 kcal/mol) as the NaCl concentration increases. This was unexpected because steric effects are considered for the most part responsible for the results in Fig. 6.18, not electrostatic interactions. These results are due to the accumulation of Na^+ ions near the OH-functionalized pores. As shown in the density distribution results of Fig. 6.19, Na^+ ions accumulate in correspondence to the minima in the PMF profile shown in Fig. 6.18, and near the OH groups. Electrostatic attractions between these Na^+ ions and Cl^- are likely responsible for the decreased PMF barrier experienced by Cl^- ions as they diffuse across the OH-functionalized pore. Despite this, the PMF barrier remains significant for Cl^- ions even at moderate ionic strength.

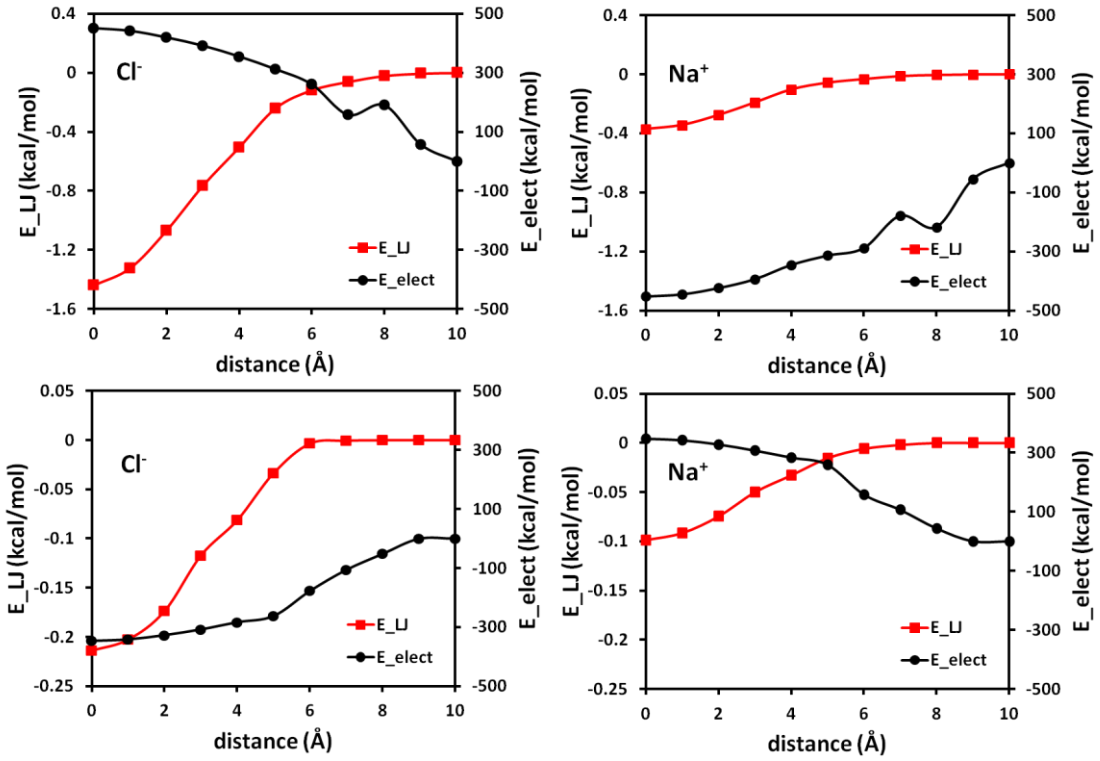

Figure 6-17 Average dispersive (E_LJ) and electrostatic (E_elec) interaction energies between Na^+ (left) and Cl^- (right) ions and functionalized GS pores as a function of the vertical distance from the pore center. Results are reported for pores functionalized with COO^- (top) and NH_3^+ (bottom) groups. The simulations were conducted at 0.25 M NaCl concentration.

In the case of the OH-functionalized pores we conducted additional simulations in which the NaCl concentration was increased further to 0.60 M, representative of seawater. The PMF results for both Na^+ (left) and Cl^- (right) ions across OH functionalized pores at 0.025 (black), 0.25 (red dashed) and 0.6 M (black dashed) NaCl are shown in Fig. 6.20. The results show no significant difference compared to those obtained at 0.25 M, except that the PMF maximum for Cl^- ion decreases to ~8 kcal/mol. This supports our speculation that electrostatic effects are not the most important ones in determining the data shown in Fig. 6.18.

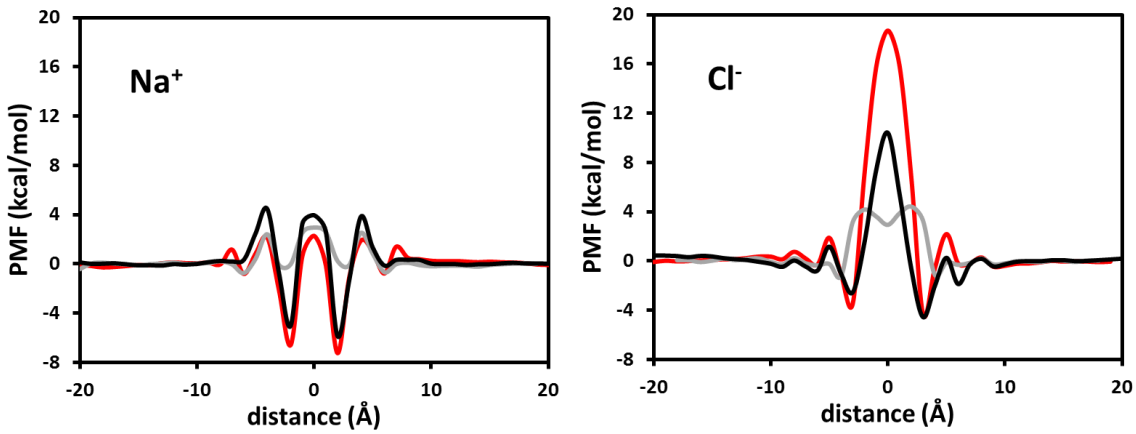

Figure 6-18 Same as Figure 6.11, but for pores functionalized with OH groups. Note that the non-functionalized pore considered for comparison is the one of diameter 10.5 Å.

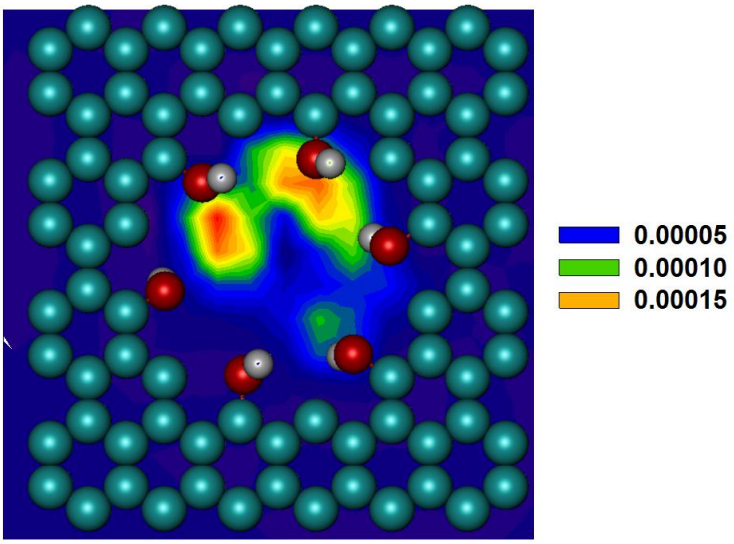

Figure 6-19 Planar density distribution for Na^+ ions near the OH functionalized pore (Ø = 7.5 Å) at 0.25 M NaCl. The units of the atomic density distribution are $Å^{-3}$.

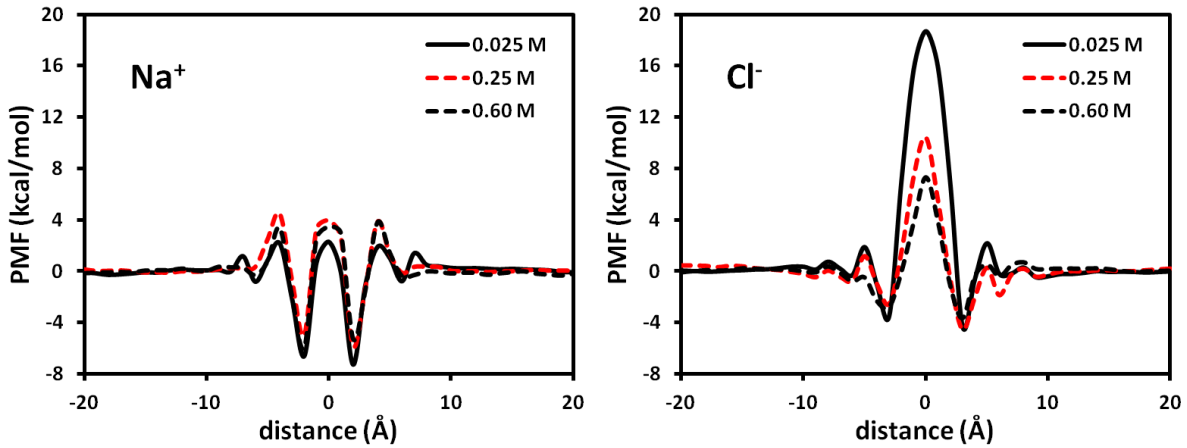

Figure 6-20 One-dimensional PMF along the direction perpendicular to the OH functionalized GS pores for Na^+ (left) and Cl^- (right) ions at 0.025 (black), 0.25 (red dashed), and 0.60 M NaCl concentration (black dashed).

To further support our speculation that steric effects are for the most part responsible for the features of the PMF data across OH-functionalized pores (Fig. 6.18), in Fig. 6.21 we report the density distribution for water within a cylinder of radius equal to the pore radius, centered in the pore center, and perpendicular to the membrane. The density profiles are compared to the PMF data. Visual inspection confirms that, for example, Na^+ ions preferentially reside within the layer formed by oxygen atoms of water at ~ 2 Å from the pore center (left panels in Fig. 6.21).

Concluding the remarks regarding data shown in Fig. 6.18, our results suggest that functionalizing narrow GS pores with OH groups may provide significant free energy barriers for the translocation of Cl^- ions at both low and moderate bulk salt concentration. These unexpected results appear to be due, for the most part, to steric effects. Also water molecules experience a free-energy penalty as they diffuse across these pores, but of significantly less intensity compared to that experienced by Cl^- ions.

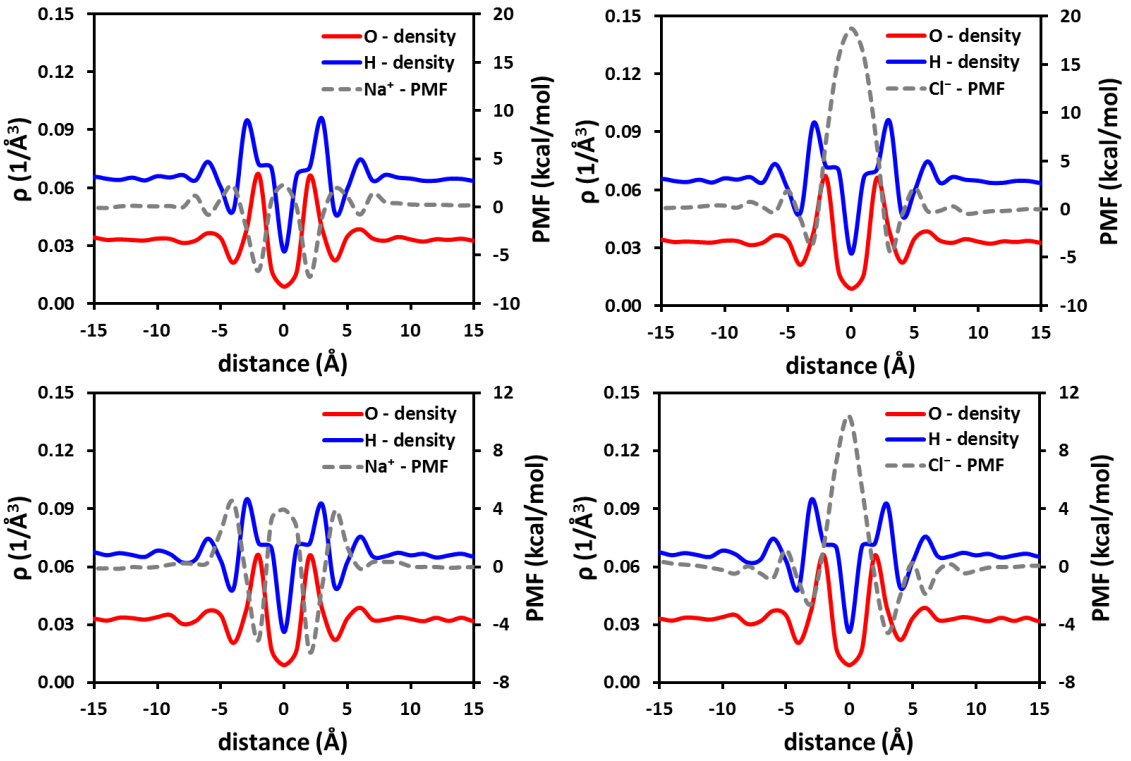

Figure 6-21 Atomic density profiles for oxygen (red) and hydrogen (blue) atoms of water within a cylinder centered in the GS pore and perpendicular to the GS membrane. The results are shown together with the PMF results for Na^+ (left) and Cl^- (right) ions across the OH functionalized pore (dashed lines) of diameter 7.5 Å. Data obtained at 0.025 (top) and 0.25 M (bottom) NaCl concentration are both shown.

6.3.3 Molecular Mechanism and Comparison to Carbon Nanotube Membranes

To gain molecular-level insights regarding the mechanism of ion transport through the various pores considered in this work, we calculated the hydration number of Na^+ and Cl^- ions as a function of their distance from the pore center. This analysis is prompted by recent simulation studies, which highlighted the role of molecular hydration on the adsorption of DNA bases on charged CNT,[272] on the hydration of solutes at interfaces,[273] on the hydrophobic hydration of small and large solutes,[274] and on the

interfacial-organized monolayer water film (MWF) induced aggregation of nanographene.[275] In our simulations the hydration number of an ion is calculated by counting the number of water molecules in the first solvation shell every 2 ps. The data are averaged over 4 ns. The diameters of the first solvation shell for Na^+ and Cl^- ions are 6.4 and 7.6 Å respectively. The coordination number is calculated for those ions that are pulled using umbrella sampling. Detailed results for the coordination number of Na^+ and Cl^- in all the systems considered are summarized in Table 6.2 and Table 6.3, respectively. In the bulk solution, Na^+ was found to be surrounded by ~ 6.0 and Cl^- by ~ 7.0 water molecules, consistent with the values reported in literature.[276] For non-functionalized GS pores, we observed that there was no significant difference in the coordination number for both ions as a function of ionic strength. The coordination number for Na^+ remained constant at ~ 6.0 (bulk value) as it passed through the 14.5 Å and 10.5 Å pores but reduced to ~ 4.0 at the center of the 7.5 Å pore. For the Cl^- ion, the coordination number was ~ 6.8, 6.3, and 5.4 at the center of the 14.5 Å, 10.5 Å, and 7.5 Å pores, respectively. Thus both ions had to lose part of their hydration shell to pass through the 7.5 Å pore, explaining the large energy penalty observed in the PMF profile of Fig. 6.2. The fact that the Na^+ ion had to lose more water molecules than the Cl^- ion explains the larger energy barrier encountered by the Na^+ ion.

Table 6-2 Hydration number for one Na^+ ion in the bulk and at the pore center in all the systems considered. Results obtained at 0.025 M and 0.25 M concentrations are compared.

	0.025 M	**0.25 M**
bulk	5.8 ± 0.6	6.0 ± 0.5
Non functionalized – ∅ = 14.5 Å	5.9 ± 0.5	5.7 ± 0.6
Non functionalized – ∅ = 10.5 Å	6.0 ± 0.6	6.0 ± 0.6
Non functionalized – ∅ = 7.5 Å	3.9 ± 0.4	3.9 ± 0.4
6 COO^-	6.3 ± 0.7	7.0 ± 0.8
6 NH_3^+	6.0 ± 0.5	5.9 ± 0.5
6 OH	5.6 ± 0.5	5.6 ± 0.5

Table 6-3 Hydration number for one Cl^- ion in the bulk and at the pore center in all the systems considered. Results obtained at 0.025 M and 0.25 M concentrations are compared.

	0.025 M	**0.25 M**
bulk	7.2 ± 0.9	6.9 ± 0.6
Non functionalized – ∅ = 14.5 Å	6.9 ± 0.8	6.8 ± 0.9
Non functionalized – ∅ = 10.5 Å	6.5 ± 0.8	6.3 ± 0.8
Non functionalized – ∅ = 7.5 Å	5.4 ± 0.6	5.4 ± 0.7
6 COO^-	6.4 ± 0.6	4.9 ± 0.9
6 NH_3^+	6.8 ± 0.7	7.0 ± 0.7
6 OH	4.9 ± 0.8	4.8 ± 0.9

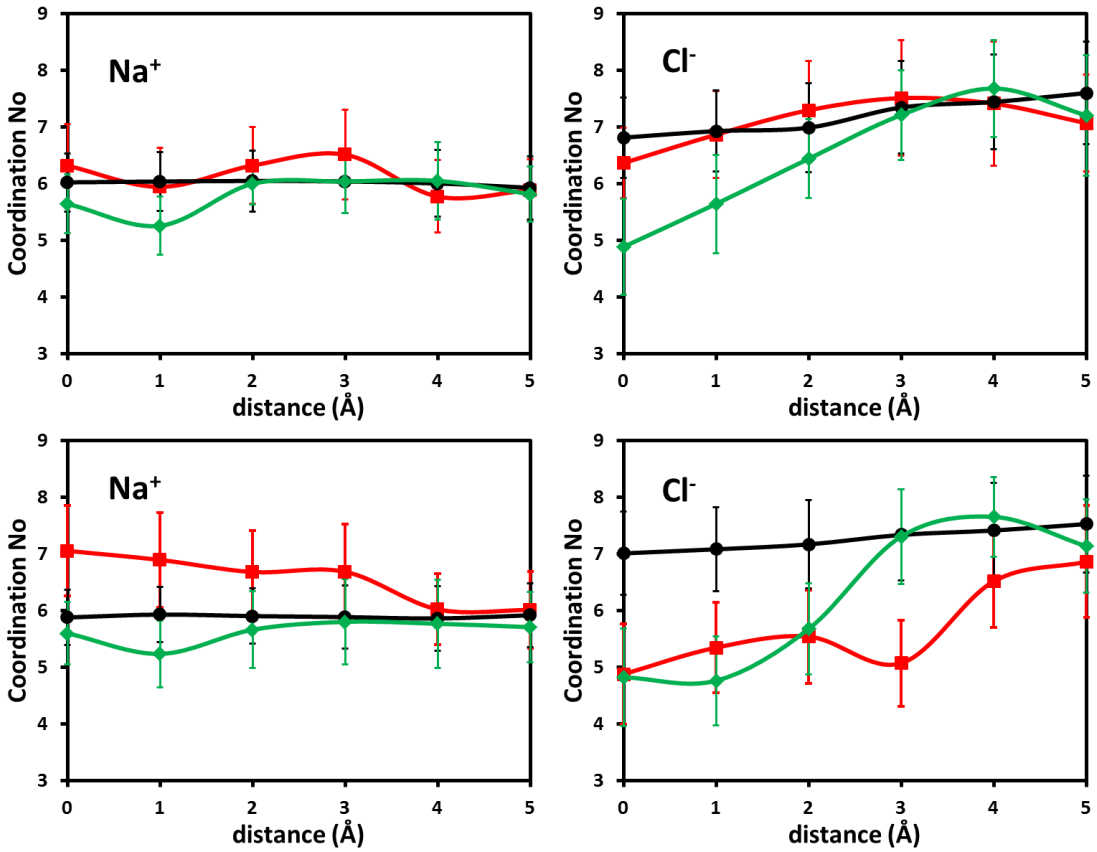

Figure 6-22 Coordination number for Na^+ (left) and Cl^- (right) as a function of the vertical distance from functionalized pores. Results are shown at infinite dilution (0.025 M, top panels), and at 0.25 M (bottom) NaCl concentration. Pores functionalized with COO^- (red), NH_3^+ (black), and OH groups (green) of diameters 10.0, 11.0, and 7.5 Å respectively are considered. Lines are guides to the eye.

When the pores are functionalized, we observe that the coordination number varies as a function of ion-pore distance and ionic concentration. The results are shown in Fig. 6.22 for Na^+ (left) and Cl^- (right) ions. The results for Na^+ ions show that the hydration number does not change substantially as the ions approach the pores, although we found that when the ion is at the center of the pore functionalized with COO^- groups it can be surrounded by ~7 water molecules (due to the overlap of the hydration shells of the Na^+ ion at the center and that of the accumulated Na^+ ions near the pore). The results for Cl^-

ions (right panels) show more pronounced changes as a function of the type of functional group. The Cl^- ion is surrounded by fewer water molecules as it enters the COO^- functionalized pore (~ 5.0 on an average at the center of the pore). However, this result holds at moderate NaCl concentration (bottom right panel), but not at low NaCl concentration (top right panel). This is because at moderate concentration, we observed that some Na^+ accumulate near the pore functionalized with COO^- groups as shown in Fig. 6.12. This suggests that ion-ion correlations near the pore center are responsible for the lower coordination number of Cl^- ion at the pore center at moderate NaCl concentration, rather than steric effects between the ion and the pore. When Cl^- ions approach the pore functionalized with NH_3^+ groups, the coordination number does not change substantially. Even though Cl^- ions accumulate near this pore, they are far away from the center of the pore. So they do not affect the coordination number of Cl^- ion at the center. When we consider the pores functionalized with OH groups, our results show a pronounced decrease in the coordination number as the ion approaches the pore center, with only ~ 5.0 water molecules hydrating the ion when it is at the pore center. This is because of the smaller size of the OH pore (7.5 Å). It is likely that this pronounced dehydration, which occurs to similar extents both at low and moderate NaCl concentration, is responsible for the effectiveness of pores functionalized with OH groups at repelling Cl^- ions.

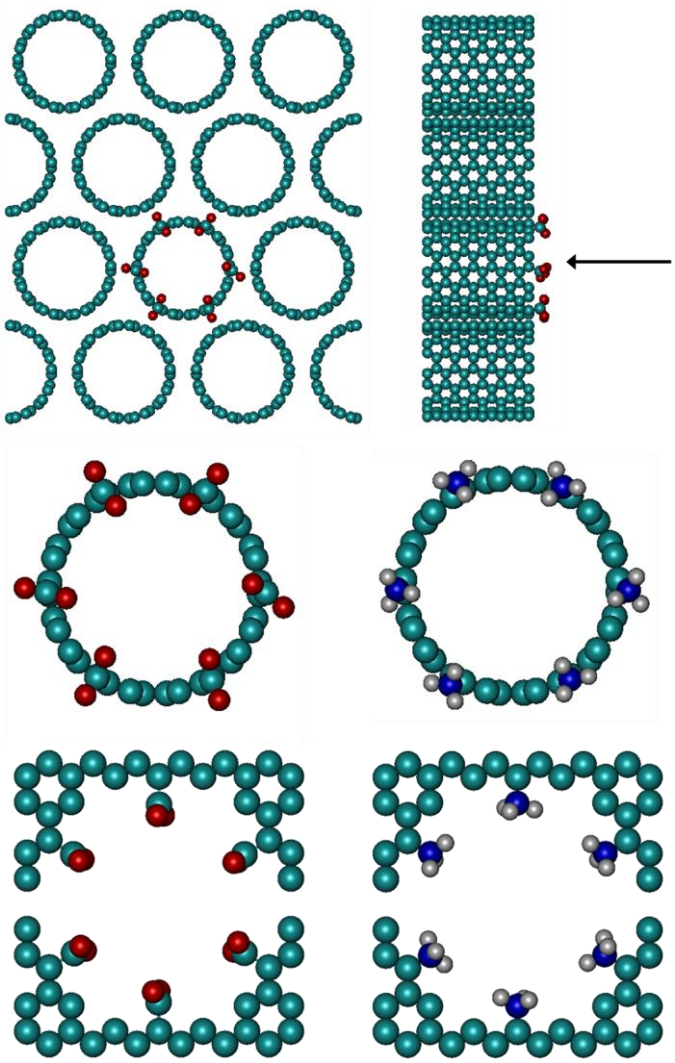

Figure 6-23 Top panel: top (left) and lateral (right) views of the nanotube membrane comprised of 12 nanotubes. One of the nanotube ends is functionalized with 6 COO^- groups. Middle panel: top view of the nanotube pores functionalized with 6 COO^- (Ø = 10.5 Å) (left) and 6 NH_3^+ (Ø = 11.5 Å) (right). Bottom panel: top view of the GS pores functionalized with 6 COO^- (Ø = 10.0 Å) (left) and 6 NH_3^+ (Ø = 11.0 Å) (right). The color code is the same as that used in Figure 6.1.

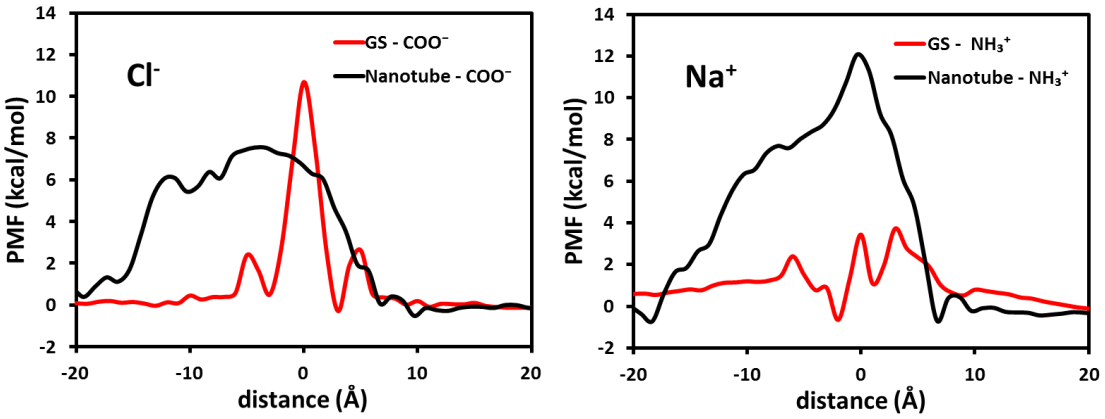

Figure 6-24 One-dimensional PMF for ion translocation through carbon nanotube (black) and GS (red) pores. Results are shown for Na^+ (left) and Cl^- (right) ions passage through pores functionalized with COO^- and NH_3^+ groups. The ions are pulled from the bulk (right) across the membrane (left). The GS pore is centered at z = 0 Å. The nanotube stretches from z = 0 to z = -13 Å. The functional groups are grafted at z = 0 Å on the nanotube.

We compared the results presented here to those obtained for CNT,[163] functionalized with the same type of group. We modeled functionalized CNT implementing the model proposed by Zhu and Schulten.[277] We considered 12 armchair type nanotubes, each 12.2 Å in diameter (measured between carbon centers) and 13 Å long. These tubes were packed hexagonally to yield a 2-D membrane. In Fig. 6.23 we show a schematic representation of the nanotube membrane used in this study. Periodic boundary conditions were employed and the membrane was solvated by ~ 20 Å of aqueous 0.25 M NaCl solution on either side. The entrance of one nanotube was functionalized with six COO^- and NH_3^+ groups, evenly distributed along the pore rim. We then calculated the PMF for both Na^+ and Cl^- ions, following the procedures described in the Methods section. In Fig. 6.24 we report the PMF results for Na^+ (left) and Cl^- (right) ions across functionalized GS and CNT pores. In the case of CNT the functional groups are grafted at the pore entrance located at z = 0 Å (the nanotubes extend along the z direction, from

z = 0 to z = -13 Å). The comparison suggests that when the pores are functionalized with NH_3^+ groups CNT provide a steeper PMF barrier to Na^+ diffusion than GS membranes do. On the contrary, when the pores are functionalized with COO^- groups, GS membranes provide higher PMF barriers to Cl^- passage than CNT do. These results suggest that not only pore size and functional groups are important, but also the geometry by which the functional groups are exposed to the aqueous solution.

6.4 Conclusions

In this study, the free energy barrier experienced by water and NaCl ions as they diffuse through pores carved out of a graphene sheet has been quantified by means of molecular dynamics simulations. For the case of pristine, non-functionalized pores, we observed that the diameter of the pore has the largest impact on determining the free energy profiles (in general, the narrower the pores, the higher the free energy barrier, although deviations from this general rule have been observed). When the narrow pores were functionalized with charged groups ($-COO^-$ or NH_3^+), the co-ions (Cl^- and Na^+, respectively) encountered large free energy barriers, because of electrostatic but also of steric effects. However, as the bulk ion concentration increases from 0.025 to 0.25 M, screening effects reduce the free energy barriers. Our results suggest that functionalizing the pores with –OH groups might be a promising strategy, as these pores yield rather strong free energy barriers for Cl^- at both low and moderate ionic strengths. Detailed analysis of the simulation results suggests that a combination of electrostatic, steric, and hydration effects determines the performance of membranes for water

desalination. Better understanding and controlling such effects may lead to technological advancements.

7 Recent Trends in Graphene Research

This section has a discussion on the recent trends in the field of graphene related to my research.

Graphene-based Nanocomposites

Several studies have been conducted in the past year to estimate the thermal conductivity of nanocomposites using graphene as a filler material. For instance Liu et al.[278] investigated the thermal boundary conductance of graphene-octane interface in the direction parallel and perpendicular to the graphene using non-equilibrium MD simulations. For a single-layer graphene immersed in liquid octane, they found that the thermal boundary conductance in the direction parallel to the graphene is 150 MW/m^2K, while in the direction perpendicular to the graphene is 5 MW/m^2K. Similarly for multilayer graphene/epoxy nanocomposites, Li et al.[237] observed that the ratio of effective thermal conductivity of the nanocomposite to the thermal conductivity of epoxy in the direction parallel to the graphene sheets (166.7) is greater than that in the direction perpendicular to the graphene sheets (37.52). These results are consistent with our results of thermal conductivity in graphene-octane nanocomposite where the ratio of effective thermal conductivity of the nanocomposite to the thermal conductivity of octane in the direction parallel to the graphene (400) is greater than that in the direction perpendicular to the graphene (1.0). Ding et al.[279] conducted experiments to calculate the thermal conductivity of polyamide-6 (PA6)/graphene nanocomposites when the graphene sheets are functionalized with PA6 and found that as the length of the PA6 chains grafted to graphene increases the thermal conductivity of the PA6/graphene

nanocomposite decreases. This result is in good agreement with a previous simulation study by Alghemandi et al.[253] which demonstrates that shorter PA6 chains are more effective in reducing the interfacial thermal resistance and improving the thermal conductivity of PA6/graphene nanocomposites.

The effective thermal conductivities of various graphene-based nanocomposites are summarized in Table 7-1. From the Table, it is evident that the addition of graphene enhances the thermal conductivity of the matrix material tremendously. For example, Choi et al.[280] prepared adhesive nanocomposites using graphene-encapsulated poly (methyl methacrylate) micro particles and found that the thermal conductivity of the resulting nanocomposites is 200% higher than that of simple blend of poly (methyl methacrylate) and graphene. Pu et al.[236] measured the thermal conductivity of silica-coated graphene (S-graphene)/epoxy nanocomposites and found that the addition of 8.0 wt% S-graphene enhances the thermal conductivity by 78% compared to that of neat epoxy. Tsai et al.[281] demonstrated that the addition of 1.0 wt% of glycidyl methacrylate-grafted graphene (g-TrG) and 50% functionalized boron nitride (f-BN) to polyimide (PI) increased the thermal conductivity of the resulting PI/f-BN-50/g-TrG-1 nanocomposite as high as 16 times compared to that of pure polyimide. Inuwa et al.[282] demonstrated that addition of 5.98 wt% of graphite nanoplatelets (GNP) to polyethylene terephthalate (PET)/polypropylene (PP) blend resulted in 80% increase in thermal conductivity of the reinforced PET/PP/GNP nanocomposites. Overall these results will be helpful for the preparation of strong, lightweight nanocomposites for thermal management applications.

Table 7-1. Effective Thermal Conductivity of Graphene-based Nanocomposites

Filler – Matrix	Method	Composition of Filler	K_{eff}/K_m	Authors
Silica coated functionalized graphene – epoxy	Modified Transient Plane Source	8.0 wt%	1.72	Pu et al.[236]
Multilayer graphene (MLG) – epoxy	DRL-III Thermal Conductivity Tester	11.8 wt%	Parallel – 166.70 Perpendicular – 37.52	Li et al.[237]
Graphene oxide (GO)/functionalized boron nitride – polyimide	CL-TIM Thermal Conductivity Tester	1.0 wt%	16.00	Tsai et al.[281]
Ionic liquid modified graphene – polyurethane	Transient Plane Source	0.6 wt%	1.34	Ma et al.[239]
Graphene – stearic acid	Hot Disk Thermal Analyzer	5.0 wt%	2.07	Li et al.[251]
Thermally reduced GO – n-eicosane/silica	Hot-wire	1.0 wt%	2.93	Wang et al.[252]
MLG – paraffin	Transient Plane Source	20.0 vol%	28.00	Warzoha et al.[247]

Graphene-based Desalination Membranes

In the last one year, several studies have been performed on the possible use of graphene as separation membranes. For example, a review article by Huang et al.[283] discusses various applications of GO membranes in gas separation, ion-selectivity and small molecules sieving. Choi et al.[284] demonstrated that the resistance to fouling and chlorine-induced degradation of polyamide (PA) thin-film composite (TFC) membranes can be improved by coating the surface of PA-TFC membranes with oppositely charged

graphene oxide (GO) nanosheets via layer-by-layer deposition. They also found that the coated GO layer acts as a chlorine barrier for the underlying PA structure, thus enhancing the salt rejection. Cohen-Tanugi et al.[285] have shown that the water permeability of nanoporous graphene membranes is high even at low pressures (< 100 bars) using MD simulations. The water flux through these membranes is found to be 6.0 l/h-bar per pore assuming a nanopore density of 1.7×10^{13} cm^{-2}. Gahlot et al.[286] prepared nanocomposite ion-exchange membranes comprising of graphene oxide (GO) and sulfonated polyethersulfone (SPES) and evaluated the desalination performance of the membranes by calculating ionic flux, power consumption and current efficiency during salt removal. They found that the addition of 10% GO to the nanocomposite membranes enhances the ionic flux and current efficiency by 19% and 12% compared to SPES membrane, while the power consumption decreases by 20%. Gai et al.[287] used MD simulations to study the transport properties across functionalized single layer graphene nanopores as forward osmosis membranes. The graphene pores considered in this work were fluorinated porous graphene (GF) and nitriding porous graphene (GN). They found that the pore size affects the water-flux and salt rejection through these membranes i.e, when the pore diameters of the GF and GN membranes were less than 11.7 Å and 13.3 Å, no salt ions passed through these membranes. Using the GF membrane with a pore diameter of 11.7 Å, Gai et al.[287] observed that the water flux is 28.1 L/cm^2-h, which is about 1.8×10^4 times higher than that of the commercial CTA membrane. Liu et al.[288] studied the influence of size, shape and density of the nanopore on the mechanical properties of nanoporous graphene membrane. The results indicate that the strength of the nanopore decreases as the size and porosity of the nanopore

increases. However the nanopore with a blunt tip perpendicular to the load direction has the highest strength. Nicolai et al.[289] studied the water desalination performance of graphene oxide framework (GOF) membranes using MD simulations. They have shown that GOF membranes offer 100% salt rejection and the water permeability is two orders of magnitude higher than exiting reverse osmosis membranes under the same conditions of applied pressure ($\Delta P \sim 10$ MPa) and thickness of membrane (~ 100 nm). O'Hern et al.[290] reported selective ion transport through nanoporous single-layer graphene membranes obtained through ion bombardment and subsequent oxidative etching into graphene pores. Transport measurements through these pores indicated that the pores were cation-selective at short oxidation times due to electrostatic repulsion from the negatively charged functional groups grafted to the pore edges. Overall these results suggest that highly selective nanopores can be prepared from graphene making use of its high mechanical strength, high aspect ratio, and its ability to be functionalized.

8 Conclusions and Future Work

Graphene sheets belong to an interesting class of new materials that could be used to enhance the properties of polymer nanocomposites. Recent technological advances are promising towards the production of large quantities of graphene sheets. Our simulation results, in some cases supported by experimental observations, suggest that the agglomeration of graphene sheets within organic matrixes can possibly be prevented by appropriately functionalizing the graphene sheets. This functionalization may be useful in abating the barriers typically encountered by heat when it flows from one inclusion to the surrounding organic matrix. We have also studied the Kapitza resistance between GS in vacuum and in octane and estimate that the GS-GS Kapitza resistance is ~ 6.5×10^{-8} Km^2W^{-1} when three GS are in octane and ~ 7.7×10^{-8} Km^2W^{-1} when the GS are in vacuum. These results suggest significantly lower Kapitza resistances for the GS-GS interface than those reported at the CNT-CNT interface. Thus, based on our calculations, it is possible that, by inducing the appearance of nematic phases within graphene sheets – based nanocomposites, materials with anisotropic properties such as thermal conductivity are obtained.

For desalination application the potential barrier for water and ions to pass through the GS membranes is studied by means of molecular dynamics simulations. The results indicate that effective ion exclusion can only be achieved using non-functionalized (pristine) pores of diameter ~ 7.5 Å, while the ions can easily penetrate pristine pores of diameter ~ 10.5 and 14.5 Å. Carboxyl functional groups can enhance ion exclusion for all pores considered, but the effect becomes less pronounced as both the ion

concentration and the pore diameter increase. When compared to a carbon nanotube (CNT) of similar pore diameter, our results suggest that GS pores functionalized with COO^- groups are more effective in excluding Cl^- ions from passing through the membrane. Our results suggest that narrow graphene pores functionalized with hydroxyl groups remain effective at excluding Cl^- ions even at moderate solution ionic strength.

Graphene is currently not used in any commercial applications. For graphene to become commercially viable, it is important to assess the impacts of GS-based materials on human health and environment. A review article by Arvidsson et al.[238] discusses the potential environmental and health risks of graphene. The results from this study indicate that graphene is toxic to human cells. So emissions of graphene should be studied for its application in nanocomposites. Also, graphene research should be focused on developing greener ways to produce GS-based composites such as ceramic reinforced composites that are highly stable and recyclable.

9 References

1. Novoselov, K. S.; Geim, A. K.; Morozov, S. V.; Jiang, D.; Zhang, Y.; Dubonos, S. V.; Grigorieva, I. V.; Firsov, A. A., Electric Field Effect in Atomically Thin Carbon Films. *Science* **2004,** *306* (5696), 666-669.

2. Dresselhaus, M. S.; Dresselhaus, G., Intercalation compounds of graphite. *Advances in Physics* **2002,** *51* (1), 1-186.

3. Hirata, M.; Gotou, T.; Horiuchi, S.; Fujiwara, M.; Ohba, M., Thin-film particles of graphite oxide 1:: High-yield synthesis and flexibility of the particles. *Carbon* **2004,** *42* (14), 2929-2937.

4. Kotov, N. A., Materials science: Carbon sheet solutions. *Nature* **2006,** *442* (7100), 254-255.

5. Geim, A. K.; Novoselov, K. S., The rise of graphene. *Nat Mater* **2007,** *6* (3), 183-191.

6. Heyrovska, R., Atomic Structures of Graphene, Benzene and Methane with Bond Lengths as Sums of the Single, Double and Resonance Bond Radii of Carbon. *arXiv:0804.4086 [physics.gen-ph]* **2008**.

7. Park, S.; Ruoff, R. S., Chemical methods for the production of graphenes. *Nat Nano* **2009,** *4* (4), 217-224.

8. Pan, D.; Wang, S.; Zhao, B.; Wu, M.; Zhang, H.; Wang, Y.; Jiao, Z., Li Storage Properties of Disordered Graphene Nanosheets. *Chemistry of Materials* **2009,** *21* (14), 3136-3142.

9. Guo, H.-L.; Wang, X.-F.; Qian, Q.-Y.; Wang, F.-B.; Xia, X.-H., A Green Approach to the Synthesis of Graphene Nanosheets. *ACS Nano* **2009,** *3* (9), 2653-2659.

10. Kim, K. S.; Zhao, Y.; Jang, H.; Lee, S. Y.; Kim, J. M.; Kim, K. S.; Ahn, J.-H.; Kim, P.; Choi, J.-Y.; Hong, B. H., Large-scale pattern growth of graphene films for stretchable transparent electrodes. *Nature* **2009,** *457* (7230), 706-710.

11. Sutter, P. W.; Flege, J.-I.; Sutter, E. A., Epitaxial graphene on ruthenium. *Nat Mater* **2008,** *7* (5), 406-411.

12. Li, X.; Cai, W.; An, J.; Kim, S.; Nah, J.; Yang, D.; Piner, R.; Velamakanni, A.; Jung, I.; Tutuc, E.; Banerjee, S. K.; Colombo, L.; Ruoff, R. S., Large-Area Synthesis of High-Quality and Uniform Graphene Films on Copper Foils. *Science* **2009,** *324* (5932), 1312-1314.

13. Eizenberg, M.; Blakely, J. M., Carbon monolayer phase condensation on Ni(111). *Surface Science* **1979,** *82* (1), 228-236.

14. Reina, A.; Jia, X.; Ho, J.; Nezich, D.; Son, H.; Bulovic, V.; Dresselhaus, M. S.; Kong, J., Large Area, Few-Layer Graphene Films on Arbitrary Substrates by Chemical Vapor Deposition. *Nano Letters* **2008,** *9* (1), 30-35.

15. Dato, A.; Radmilovic, V.; Lee, Z.; Phillips, J.; Frenklach, M., Substrate-Free Gas-Phase Synthesis of Graphene Sheets. *Nano Letters* **2008,** *8* (7), 2012-2016.

16. Takatoshi, Y.; Jaeho, K.; Masatou, I.; Masataka, H., Low-temperature graphene synthesis using microwave plasma CVD. *Journal of Physics D: Applied Physics* **2013,** *46* (6), 063001.

17. Aizawa, T.; Souda, R.; Otani, S.; Ishizawa, Y.; Oshima, C., Anomalous bond of monolayer graphite on transition-metal carbide surfaces. *Physical Review Letters* **1990,** *64* (7), 768-771.

18. Li, X.; Zhu, Y.; Cai, W.; Borysiak, M.; Han, B.; Chen, D.; Piner, R. D.; Colombo, L.; Ruoff, R. S., Transfer of Large-Area Graphene Films for High-Performance Transparent Conductive Electrodes. *Nano Letters* **2009,** *9* (12), 4359-4363.

19. Campos-Delgado, J.; Romo-Herrera, J. M.; Jia, X.; Cullen, D. A.; Muramatsu, H.; Kim, Y. A.; Hayashi, T.; Ren, Z.; Smith, D. J.; Okuno, Y.; Ohba, T.; Kanoh, H.; Kaneko, K.; Endo, M.; Terrones, H.; Dresselhaus, M. S.; Terrones, M., Bulk Production of a New Form of sp2 Carbon: Crystalline Graphene Nanoribbons. *Nano Letters* **2008,** *8* (9), 2773-2778.

20. Lu, T.; Zhang, Y.; Li, H.; Pan, L.; Li, Y.; Sun, Z., Electrochemical behaviors of graphene–ZnO and graphene–SnO2 composite films for supercapacitors. *Electrochimica Acta* **2010,** *55* (13), 4170-4173.

21. Tung, V. C.; Allen, M. J.; Yang, Y.; Kaner, R. B., High-throughput solution processing of large-scale graphene. *Nat Nano* **2009,** *4* (1), 25-29.

22. Rao, C. N. R.; Sood, A. K.; Subrahmanyam, K. S.; Govindaraj, A., Graphene: The New Two-Dimensional Nanomaterial. *Angewandte Chemie International Edition* **2009,** *48* (42), 7752-7777.

23. Wang, G.; Yang, J.; Park, J.; Gou, X.; Wang, B.; Liu, H.; Yao, J., Facile Synthesis and Characterization of Graphene Nanosheets. *The Journal of Physical Chemistry C* **2008,** *112* (22), 8192-8195.

24. Yang, X.; Dou, X.; Rouhanipour, A.; Zhi, L.; Räder, H. J.; Müllen, K., Two-Dimensional Graphene Nanoribbons. *Journal of the American Chemical Society* **2008,** *130* (13), 4216-4217.

25. Stankovich, S.; Dikin, D. A.; Piner, R. D.; Kohlhaas, K. A.; Kleinhammes, A.; Jia, Y.; Wu, Y.; Nguyen, S. T.; Ruoff, R. S., Synthesis of graphene-based nanosheets via chemical reduction of exfoliated graphite oxide. *Carbon* **2007,** *45* (7), 1558-1565.

26. Liang, Y.; Wu, D.; Feng, X.; Müllen, K., Dispersion of Graphene Sheets in Organic Solvent Supported by Ionic Interactions. *Advanced Materials* **2009,** *21* (17), 1679-1683.

27. Worsley, K. A.; Ramesh, P.; Mandal, S. K.; Niyogi, S.; Itkis, M. E.; Haddon, R. C., Soluble graphene derived from graphite fluoride. *Chemical Physics Letters* **2007,** *445* (1–3), 51-56.

28. Carissan, Y.; Klopper, W., Growing Graphene Sheets from Reactions with Methyl Radicals: A Quantum Chemical Study. *ChemPhysChem* **2006,** *7* (8), 1770-1778.

29. Zhi, L.; Mullen, K., A bottom-up approach from molecular nanographenes to unconventional carbon materials. *Journal of Materials Chemistry* **2008,** *18* (13), 1472-1484.

30. Li, N.; Wang, Z.; Zhao, K.; Shi, Z.; Gu, Z.; Xu, S., Large scale synthesis of N-doped multi-layered graphene sheets by simple arc-discharge method. *Carbon* **2010,** *48* (1), 255-259.

31. Soumen, K.; Naveen, V. K.; Ashok, B. N.; Niranjan, P. L.; Ratikant, M.; Sathe, V. G.; Bhoraskar, S. V.; Das, A. K., A novel approach towards selective bulk synthesis of few-layer graphenes in an electric arc. *Journal of Physics D: Applied Physics* **2009,** *42* (11), 115201.

32. Subrahmanyam, K. S.; Panchakarla, L. S.; Govindaraj, A.; Rao, C. N. R., Simple Method of Preparing Graphene Flakes by an Arc-Discharge Method. *The Journal of Physical Chemistry C* **2009,** *113* (11), 4257-4259.

33. Wu, Z.-S.; Ren, W.; Gao, L.; Zhao, J.; Chen, Z.; Liu, B.; Tang, D.; Yu, B.; Jiang, C.; Cheng, H.-M., Synthesis of Graphene Sheets with High Electrical Conductivity and Good Thermal Stability by Hydrogen Arc Discharge Exfoliation. *ACS Nano* **2009,** *3* (2), 411-417.

34. Volotskova, O.; Levchenko, I.; Shashurin, A.; Raitses, Y.; Ostrikov, K.; Keidar, M., Single-step synthesis and magnetic separation of graphene and carbon nanotubes in arc discharge plasmas. *Nanoscale* **2010,** *2* (10), 2281-2285.

35. Singh, V.; Joung, D.; Zhai, L.; Das, S.; Khondaker, S. I.; Seal, S., Graphene based materials: Past, present and future. *Progress in Materials Science* **2011,** *56* (8), 1178-1271.

36. Jiao, L.; Zhang, L.; Wang, X.; Diankov, G.; Dai, H., Narrow graphene nanoribbons from carbon nanotubes. *Nature* **2009,** *458* (7240), 877-880.

37. Choucair, M.; Thordarson, P.; Stride, J. A., Gram-scale production of graphene based on solvothermal synthesis and sonication. *Nat Nano* **2009,** *4* (1), 30-33.

38. Murugan, A. V.; Muraliganth, T.; Manthiram, A., Rapid, Facile Microwave-Solvothermal Synthesis of Graphene Nanosheets and Their Polyaniline Nanocomposites for Energy Strorage. *Chemistry of Materials* **2009,** *21* (21), 5004-5006.

39. Wang, P.; Jiang, T.; Zhu, C.; Zhai, Y.; Wang, D.; Dong, S., One-step, solvothermal synthesis of graphene-CdS and graphene-ZnS quantum dot nanocomposites and their interesting photovoltaic properties. *Nano Res.* **2010,** *3* (11), 794-799.

40. Li, S.-J.; Deng, D.-H.; Shi, Q.; Liu, S.-R., Electrochemical synthesis of a graphene sheet and gold nanoparticle-based nanocomposite, and its application to amperometric sensing of dopamine. *Microchim Acta* **2012,** *177* (3-4), 325-331.

41. Yang, J.; Deng, S.; Lei, J.; Ju, H.; Gunasekaran, S., Electrochemical synthesis of reduced graphene sheet–AuPd alloy nanoparticle composites for enzymatic biosensing. *Biosensors and Bioelectronics* **2011,** *29* (1), 159-166.

42. Liu, N.; Luo, F.; Wu, H.; Liu, Y.; Zhang, C.; Chen, J., One-Step Ionic-Liquid-Assisted Electrochemical Synthesis of Ionic-Liquid-Functionalized Graphene Sheets Directly from Graphite. *Advanced Functional Materials* **2008,** *18* (10), 1518-1525.

43. Kim, H.; Abdala, A. A.; Macosko, C. W., Graphene/Polymer Nanocomposites. *Macromolecules* **2010,** *43* (16), 6515-6530.

44. Potts, J. R.; Dreyer, D. R.; Bielawski, C. W.; Ruoff, R. S., Graphene-based polymer nanocomposites. *Polymer* **2011,** *52* (1), 5-25.

45. Berger, C.; Song, Z.; Li, X.; Wu, X.; Brown, N.; Naud, C.; Mayou, D.; Li, T.; Hass, J.; Marchenkov, A. N.; Conrad, E. H.; First, P. N.; de Heer, W. A., Electronic Confinement and Coherence in Patterned Epitaxial Graphene. *Science* **2006,** *312* (5777), 1191-1196.

46. de Heer, W. A.; Berger, C.; Wu, X.; First, P. N.; Conrad, E. H.; Li, X.; Li, T.; Sprinkle, M.; Hass, J.; Sadowski, M. L.; Potemski, M.; Martinez, G., Epitaxial graphene. *Solid State Communications* **2007,** *143* (1–2), 92-100.

47. Rollings, E.; Gweon, G. H.; Zhou, S. Y.; Mun, B. S.; McChesney, J. L.; Hussain, B. S.; Fedorov, A. V.; First, P. N.; de Heer, W. A.; Lanzara, A., Synthesis and characterization of atomically thin graphite films on a silicon carbide substrate. *Journal of Physics and Chemistry of Solids* **2006,** *67* (9–10), 2172-2177.

48. Ni, Z. H.; Chen, W.; Fan, X. F.; Kuo, J. L.; Yu, T.; Wee, A. T. S.; Shen, Z. X., Raman spectroscopy of epitaxial graphene on a SiC substrate. *Physical Review B* **2008,** *77* (11), 115416.

49. Seyller, T.; Bostwick, A.; Emtsev, K. V.; Horn, K.; Ley, L.; McChesney, J. L.; Ohta, T.; Riley, J. D.; Rotenberg, E.; Speck, F., Epitaxial graphene: a new material. *physica status solidi (b)* **2008,** *245* (7), 1436-1446.

50. Chen, L.; Hernandez, Y.; Feng, X.; Müllen, K., From Nanographene and Graphene Nanoribbons to Graphene Sheets: Chemical Synthesis. *Angewandte Chemie International Edition* **2012,** *51* (31), 7640-7654.

51. Mattausch, A.; Pankratov, O., Density functional study of graphene overlayers on SiC. *physica status solidi (b)* **2008,** *245* (7), 1425-1435.

52. Fogel, Y.; Zhi, L.; Rouhanipour, A.; Andrienko, D.; Räder, H. J.; Müllen, K., Graphitic Nanoribbons with Dibenzo[e,l]pyrene Repeat Units: Synthesis and Self-Assembly. *Macromolecules* **2009,** *42* (18), 6878-6884.

53. Dössel, L.; Gherghel, L.; Feng, X.; Müllen, K., Graphene Nanoribbons by Chemists: Nanometer-Sized, Soluble, and Defect-Free. *Angewandte Chemie International Edition* **2011,** *50* (11), 2540-2543.

54. Kuldeep, S.; Anil, O.; Dhawan, S. K., Polymer-Graphene Nanocomposites: Preparation, Characterization, Properties, and Applications. 2012.

55. Kim, C.-D.; Min, B.-K.; Jung, W.-S., Preparation of graphene sheets by the reduction of carbon monoxide. *Carbon* **2009,** *47* (6), 1610-1612.

56. Kosynkin, D. V.; Higginbotham, A. L.; Sinitskii, A.; Lomeda, J. R.; Dimiev, A.; Price, B. K.; Tour, J. M., Longitudinal unzipping of carbon nanotubes to form graphene nanoribbons. *Nature* **2009,** *458* (7240), 872-876.

57. Hirsch, A., Unzipping Carbon Nanotubes: A Peeling Method for the Formation of Graphene Nanoribbons. *Angewandte Chemie International Edition* **2009,** *48* (36), 6594-6596.

58. Janowska, I.; Ersen, O.; Jacob, T.; Vennégues, P.; Bégin, D.; Ledoux, M.-J.; Pham-Huu, C., Catalytic unzipping of carbon nanotubes to few-layer graphene sheets under microwaves irradiation. *Applied Catalysis A: General* **2009,** *371* (1–2), 22-30.

59. Mohammadi, S.; Kolahdouz, Z.; Darbari, S.; Mohajerzadeh, S.; Masoumi, N., Graphene formation by unzipping carbon nanotubes using a sequential plasma assisted processing. *Carbon* **2013,** *52* (0), 451-463.

60. Barnard, A. S.; Snook, I. K., Thermal stability of graphene edge structure and graphene nanoflakes. *The Journal of Chemical Physics* **2008,** *128* (9), 094707-7.

61. Lee, C.; Wei, X.; Kysar, J. W.; Hone, J., Measurement of the Elastic Properties and Intrinsic Strength of Monolayer Graphene. *Science* **2008,** *321* (5887), 385-388.

62. Balandin, A. A.; Ghosh, S.; Bao, W.; Calizo, I.; Teweldebrhan, D.; Miao, F.; Lau, C. N., Superior Thermal Conductivity of Single-Layer Graphene. *Nano Letters* **2008,** *8* (3), 902-907.

63. Hu, J.; Ruan, X.; Chen, Y. P., Thermal Conductivity and Thermal Rectification in Graphene Nanoribbons: A Molecular Dynamics Study. *Nano Letters* **2009,** *9* (7), 2730-2735.

64. Cai, W.; Moore, A. L.; Zhu, Y.; Li, X.; Chen, S.; Shi, L.; Ruoff, R. S., Thermal Transport in Suspended and Supported Monolayer Graphene Grown by Chemical Vapor Deposition. *Nano Letters* **2010,** *10* (5), 1645-1651.

65. Faugeras, C.; Faugeras, B.; Orlita, M.; Potemski, M.; Nair, R. R.; Geim, A. K., Thermal Conductivity of Graphene in Corbino Membrane Geometry. *ACS Nano* **2010,** *4* (4), 1889-1892.

66. Wang, X.; Li, X.; Zhang, L.; Yoon, Y.; Weber, P. K.; Wang, H.; Guo, J.; Dai, H., N-Doping of Graphene Through Electrothermal Reactions with Ammonia. *Science* **2009,** *324* (5928), 768-771.

67. Lin, Y.-M.; Valdes-Garcia, A.; Han, S.-J.; Farmer, D. B.; Meric, I.; Sun, Y.; Wu, Y.; Dimitrakopoulos, C.; Grill, A.; Avouris, P.; Jenkins, K. A., Wafer-Scale Graphene Integrated Circuit. *Science* **2011,** *332* (6035), 1294-1297.

68. Brey, L.; Fertig, H. A., Electronic states of graphene nanoribbons studied with the Dirac equation. *Physical Review B* **2006,** *73* (23), 235411.

69. Son, Y.-W.; Cohen, M. L.; Louie, S. G., Energy Gaps in Graphene Nanoribbons. *Physical Review Letters* **2006,** *97* (21), 216803.

70. Wang, X.; Zhi, L.; Mullen, K., Transparent, Conductive Graphene Electrodes for Dye-Sensitized Solar Cells. *Nano Letters* **2007,** *8* (1), 323-327.

71. Eda, G.; Fanchini, G.; Chhowalla, M., Large-area ultrathin films of reduced graphene oxide as a transparent and flexible electronic material. *Nat Nano* **2008,** *3* (5), 270-274.

72. Wang, Y.; Chen, X.; Zhong, Y.; Zhu, F.; Loh, K. P., Large area, continuous, few-layered graphene as anodes in organic photovoltaic devices. *Applied Physics Letters* **2009,** *95* (6), 063302-3.

73. Wu, J.; Agrawal, M.; Becerril, H. A.; Bao, Z.; Liu, Z.; Chen, Y.; Peumans, P., Organic Light-Emitting Diodes on Solution-Processed Graphene Transparent Electrodes. *ACS Nano* **2009,** *4* (1), 43-48.

74. Mohanty, N.; Moore, D.; Xu, Z.; Sreeprasad, T. S.; Nagaraja, A.; Rodriguez, A. A.; Berry, V., Nanotomy-based production of transferable and dispersible graphene nanostructures of controlled shape and size. *Nat Commun* **2012,** *3*, 844.

75. Cai, J.; Ruffieux, P.; Jaafar, R.; Bieri, M.; Braun, T.; Blankenburg, S.; Muoth, M.; Seitsonen, A. P.; Saleh, M.; Feng, X.; Mullen, K.; Fasel, R., Atomically precise bottom-up fabrication of graphene nanoribbons. *Nature* **2010,** *466* (7305), 470-473.

76. Liu, M.; Yin, X.; Ulin-Avila, E.; Geng, B.; Zentgraf, T.; Ju, L.; Wang, F.; Zhang, X., A graphene-based broadband optical modulator. *Nature* **2011,** *474* (7349), 64-67.

77. Liang, Q.; Yao, X.; Wang, W.; Liu, Y.; Wong, C. P., A Three-Dimensional Vertically Aligned Functionalized Multilayer Graphene Architecture: An Approach for Graphene-Based Thermal Interfacial Materials. *ACS Nano* **2011,** *5* (3), 2392-2401.

78. Stoller, M. D.; Park, S.; Zhu, Y.; An, J.; Ruoff, R. S., Graphene-Based Ultracapacitors. *Nano Letters* **2008,** *8* (10), 3498-3502.

79. Schedin, F.; Geim, A. K.; Morozov, S. V.; Hill, E. W.; Blake, P.; Katsnelson, M. I.; Novoselov, K. S., Detection of individual gas molecules adsorbed on graphene. *Nat Mater* **2007,** *6* (9), 652-655.

80. Bunch, J. S.; van der Zande, A. M.; Verbridge, S. S.; Frank, I. W.; Tanenbaum, D. M.; Parpia, J. M.; Craighead, H. G.; McEuen, P. L., Electromechanical Resonators from Graphene Sheets. *Science* **2007,** *315* (5811), 490-493.

81. Shen, H.; Zhang, L.; Liu, M.; Zhang, Z., Biomedical Applications of Graphene. *Theranostics* **2012,** *2* (3), 283-294.

82. Li, D.; Muller, M. B.; Gilje, S.; Kaner, R. B.; Wallace, G. G., Processable aqueous dispersions of graphene nanosheets. *Nat Nano* **2008,** *3* (2), 101-105.

83. Rittigstein, P.; Priestley, R. D.; Broadbelt, L. J.; Torkelson, J. M., Model polymer nanocomposites provide an understanding of confinement effects in real nanocomposites. *Nat Mater* **2007,** *6* (4), 278-282.

84. Liff, S. M.; Kumar, N.; McKinley, G. H., High-performance elastomeric nanocomposites via solvent-exchange processing. *Nat Mater* **2007,** *6* (1), 76-83.

85. Sen, S.; Thomin, J. D.; Kumar, S. K.; Keblinski, P., Molecular Underpinnings of the Mechanical Reinforcement in Polymer Nanocomposites. *Macromolecules* **2007,** *40* (11), 4059-4067.

86. Krishnamoorti, R., Strategies for Dispersing Nanoparticles in Polymers. *MRS Bulletin* **2007,** *32* (04), 341-347.

87. Ajayan, P. M.; Schadler, L. S.; Giannaris, C.; Rubio, A., Single-Walled Carbon Nanotube–Polymer Composites: Strength and Weakness. *Advanced Materials* **2000,** *12* (10), 750-753.

88. Wakabayashi, K.; Pierre, C.; Dikin, D. A.; Ruoff, R. S.; Ramanathan, T.; Brinson, L. C.; Torkelson, J. M., Polymer−Graphite Nanocomposites: Effective Dispersion and Major Property Enhancement via Solid-State Shear Pulverization. *Macromolecules* **2008,** *41* (6), 1905-1908.

89. Sumita, M.; Tsukihi, H.; Miyasaka, K.; Ishikawa, K., Dynamic mechanical properties of polypropylene composites filled with ultrafine particles. *Journal of Applied Polymer Science* **1984,** *29* (5), 1523-1530.

90. Ash, B. J.; Stone, J.; Rogers, D. F.; Schadler, L. S.; Siegel, R. W.; Benicewicz, B. C.; Apple, T., Investigation into the Thermal and Mechanical Behavior of PMMA/Alumina Nanocomposites. *MRS Online Proceedings Library* **2000,** *661*, null-null.

91. Becker, C.; Krug, H.; Schmidt, H., Tailoring of Thermomechanical Properties of Thermoplastic Nanocomposites by Surface Modification of Nanoscale Silica Particles. *MRS Online Proceedings Library* **1996,** *435*, null-null.

92. Ramanathan, T.; Liu, H.; Brinson, L. C., Functionalized SWNT/polymer nanocomposites for dramatic property improvement. *Journal of Polymer Science Part B: Polymer Physics* **2005,** *43* (17), 2269-2279.

93. LeBaron, P. C.; Wang, Z.; Pinnavaia, T. J., Polymer-layered silicate nanocomposites: an overview. *Applied Clay Science* **1999,** *15* (1–2), 11-29.

94. Zheng, W.; Lu, X.; Wong, S.-C., Electrical and mechanical properties of expanded graphite-reinforced high-density polyethylene. *Journal of Applied Polymer Science* **2004,** *91* (5), 2781-2788.

95. Pan, Y.-X.; Yu, Z.-Z.; Ou, Y.-C.; Hu, G.-H., A new process of fabricating electrically conducting nylon 6/graphite nanocomposites via intercalation polymerization. *Journal of Polymer Science Part B: Polymer Physics* **2000,** *38* (12), 1626-1633.

96. Chen, G.; Weng, W.; Wu, D.; Wu, C., PMMA/graphite nanosheets composite and its conducting properties. *European Polymer Journal* **2003,** *39* (12), 2329-2335.

97. Ramanathan, T.; Stankovich, S.; Dikin, D. A.; Liu, H.; Shen, H.; Nguyen, S. T.; Brinson, L. C., Graphitic nanofillers in PMMA nanocomposites—An investigation of particle size and dispersion and their influence on nanocomposite properties. *Journal of Polymer Science Part B: Polymer Physics* **2007,** *45* (15), 2097-2112.

98. Kim, P.; Shi, L.; Majumdar, A.; McEuen, P. L., Thermal Transport Measurements of Individual Multiwalled Nanotubes. *Physical Review Letters* **2001,** *87* (21), 215502.

99. Berber, S.; Kwon, Y.-K.; Tománek, D., Unusually High Thermal Conductivity of Carbon Nanotubes. *Physical Review Letters* **2000,** *84* (20), 4613-4616.

100. Biercuk, M. J.; Llaguno, M. C.; Radosavljevic, M.; Hyun, J. K.; Johnson, A. T.; Fischer, J. E., Carbon nanotube composites for thermal management. *Applied Physics Letters* **2002,** *80* (15), 2767-2769.

101. Choi, S. U. S.; Zhang, Z. G.; Yu, W.; Lockwood, F. E.; Grulke, E. A., Anomalous thermal conductivity enhancement in nanotube suspensions. *Applied Physics Letters* **2001,** *79* (14), 2252-2254.

102. Shenogin, S.; Xue, L.; Ozisik, R.; Keblinski, P.; Cahill, D. G., Role of thermal boundary resistance on the heat flow in carbon-nanotube composites. *Journal of Applied Physics* **2004,** *95* (12), 8136-8144.

103. Huxtable, S. T.; Cahill, D. G.; Shenogin, S.; Xue, L.; Ozisik, R.; Barone, P.; Usrey, M.; Strano, M. S.; Siddons, G.; Shim, M.; Keblinski, P., Interfacial heat flow in carbon nanotube suspensions. *Nat Mater* **2003,** *2* (11), 731-734.

104. Shenogina, N.; Godawat, R.; Keblinski, P.; Garde, S., How Wetting and Adhesion Affect Thermal Conductance of a Range of Hydrophobic to Hydrophilic Aqueous Interfaces. *Physical Review Letters* **2009,** *102* (15), 156101.

105. Kapitza, P. L., *J. Exp. Theor. Phys.* **1941,** *11* (1), 1.

106. Swartz, E. T.; Pohl, R. O., Thermal boundary resistance. *Reviews of Modern Physics* **1989,** *61* (3), 605-668.

107. Cote, L. J.; Kim, F.; Huang, J., Langmuir−Blodgett Assembly of Graphite Oxide Single Layers. *Journal of the American Chemical Society* **2008,** *131* (3), 1043-1049.

108. Schniepp, H. C.; Li, J.-L.; McAllister, M. J.; Sai, H.; Herrera-Alonso, M.; Adamson, D. H.; Prud'homme, R. K.; Car, R.; Saville, D. A.; Aksay, I. A., Functionalized Single Graphene Sheets Derived from Splitting Graphite Oxide. *The Journal of Physical Chemistry B* **2006,** *110* (17), 8535-8539.

109. Gusynin, V. P.; Sharapov, S. G., Unconventional Integer Quantum Hall Effect in Graphene. *Physical Review Letters* **2005,** *95* (14), 146801.

110. Zhang, Y.; Tan, Y.-W.; Stormer, H. L.; Kim, P., Experimental observation of the quantum Hall effect and Berry's phase in graphene. *Nature* **2005,** *438* (7065), 201-204.

111. Novoselov, K. S.; Jiang, Z.; Zhang, Y.; Morozov, S. V.; Stormer, H. L.; Zeitler, U.; Maan, J. C.; Boebinger, G. S.; Kim, P.; Geim, A. K., Room-Temperature Quantum Hall Effect in Graphene. *Science* **2007,** *315* (5817), 1379-1379.

112. Novoselov, K. S.; Morozov, S. V.; Mohinddin, T. M. G.; Ponomarenko, L. A.; Elias, D. C.; Yang, R.; Barbolina, I. I.; Blake, P.; Booth, T. J.; Jiang, D.; Giesbers, J.; Hill, E. W.; Geim, A. K., Electronic properties of graphene. *physica status solidi (b)* **2007,** *244* (11), 4106-4111.

113. Yu, M.-F.; Lourie, O.; Dyer, M. J.; Moloni, K.; Kelly, T. F.; Ruoff, R. S., Strength and Breaking Mechanism of Multiwalled Carbon Nanotubes Under Tensile Load. *Science* **2000,** *287* (5453), 637-640.

114. Stankovich, S.; Piner, R. D.; Chen, X.; Wu, N.; Nguyen, S. T.; Ruoff, R. S., Stable aqueous dispersions of graphitic nanoplatelets via the reduction of exfoliated graphite oxide in the presence of poly(sodium 4-styrenesulfonate). *Journal of Materials Chemistry* **2006,** *16* (2), 155-158.

115. Li, X.; Wang, X.; Zhang, L.; Lee, S.; Dai, H., Chemically Derived, Ultrasmooth Graphene Nanoribbon Semiconductors. *Science* **2008,** *319* (5867), 1229-1232.

116. Wu, J.; Pisula, W.; Müllen, K., Graphenes as Potential Material for Electronics. *Chemical Reviews* **2007,** *107* (3), 718-747.

117. Yan, X.; Cui, X.; Li, B.; Li, L.-s., Large, Solution-Processable Graphene Quantum Dots as Light Absorbers for Photovoltaics. *Nano Letters* **2010,** *10* (5), 1869-1873.

118. Yan, X.; Cui, X.; Li, L.-s., Synthesis of Large, Stable Colloidal Graphene Quantum Dots with Tunable Size. *Journal of the American Chemical Society* **2010,** *132* (17), 5944-5945.

119. Novoselov, K. S.; Geim, A. K.; Morozov, S. V.; Jiang, D.; Katsnelson, M. I.; Grigorieva, I. V.; Dubonos, S. V.; Firsov, A. A., Two-dimensional gas of massless Dirac fermions in graphene. *Nature* **2005,** *438* (7065), 197-200.

120. Stankovich, S.; Dikin, D. A.; Dommett, G. H. B.; Kohlhaas, K. M.; Zimney, E. J.; Stach, E. A.; Piner, R. D.; Nguyen, S. T.; Ruoff, R. S., Graphene-based composite materials. *Nature* **2006,** *442* (7100), 282-286.

121. Shen, J.; Hu, Y.; Shi, M.; Lu, X.; Qin, C.; Li, C.; Ye, M., Fast and Facile Preparation of Graphene Oxide and Reduced Graphene Oxide Nanoplatelets. *Chemistry of Materials* **2009,** *21* (15), 3514-3520.

122. Fang, M.; Wang, K.; Lu, H.; Yang, Y.; Nutt, S., Single-layer graphene nanosheets with controlled grafting of polymer chains. *Journal of Materials Chemistry* **2010,** *20* (10), 1982-1992.

123. Reddy, C. D.; Rajendran, S.; Liew, K. M., Equilibrium configuration and continuum elastic properties of finite sized graphene. *Nanotechnology* **2006,** *17* (3), 864.

124. Radovic, L. R.; Bockrath, B., On the Chemical Nature of Graphene Edges: Origin of Stability and Potential for Magnetism in Carbon Materials. *Journal of the American Chemical Society* **2005,** *127* (16), 5917-5927.

125. Niyogi, S.; Bekyarova, E.; Itkis, M. E.; McWilliams, J. L.; Hamon, M. A.; Haddon, R. C., Solution Properties of Graphite and Graphene. *Journal of the American Chemical Society* **2006,** *128* (24), 7720-7721.

126. Kotov, N. A.; Dékány, I.; Fendler, J. H., Ultrathin graphite oxide–polyelectrolyte composites prepared by self-assembly: Transition between conductive and non-conductive states. *Advanced Materials* **1996,** *8* (8), 637-641.

127. Kovtyukhova, N. I.; Ollivier, P. J.; Martin, B. R.; Mallouk, T. E.; Chizhik, S. A.; Buzaneva, E. V.; Gorchinskiy, A. D., Layer-by-Layer Assembly of Ultrathin Composite Films from Micron-Sized Graphite Oxide Sheets and Polycations. *Chemistry of Materials* **1999,** *11* (3), 771-778.

128. Baldwin, J. E., Reactions on the Femtosecond Time Scale. In *Reactive Intermediate Chemistry*, John Wiley & Sons, Inc.: 2005; pp 899-924.

129. Wenk, H. H.; Winkler, M.; Sander, W., One Century of Aryne Chemistry. *Angewandte Chemie International Edition* **2003,** *42* (5), 502-528.

130. Moss, R. A.; Platz, M. S.; Jones, J. M., *Reactive Intermediate Chemistry*. Wiley-Interscience: New York, 2004.

131. RamanathanT; Abdala, A. A.; StankovichS; Dikin, D. A.; Herrera Alonso, M.; Piner, R. D.; Adamson, D. H.; Schniepp, H. C.; ChenX; Ruoff, R. S.; Nguyen, S. T.; Aksay, I. A.; Prud'Homme, R. K.; Brinson, L. C., Functionalized graphene sheets for polymer nanocomposites. *Nat Nano* **2008,** *3* (6), 327-331.

132. Yu, A.; Ramesh, P.; Itkis, M. E.; Bekyarova, E.; Haddon, R. C., Graphite Nanoplatelet−Epoxy Composite Thermal Interface Materials. *The Journal of Physical Chemistry C* **2007,** *111* (21), 7565-7569.

133. Xu, Y.; Bai, H.; Lu, G.; Li, C.; Shi, G., Flexible Graphene Films via the Filtration of Water-Soluble Noncovalent Functionalized Graphene Sheets. *Journal of the American Chemical Society* **2008,** *130* (18), 5856-5857.

134. Striolo, A., Colloidal brushes in complex solutions: Existence of a weak midrange attraction due to excluded-volume effects. *Physical Review E* **2006,** *74* (4), 041401.

135. Striolo, A., Controlled Assembly of Spherical Nanoparticles: Nanowires and Spherulites. *Small* **2007,** *3* (4), 628-635.

136. Frenkel, D.; Smit, B., Understanding Molecular Simulations: From Algorithms to Applications. *Academic Press: San Diego, CA* **1996,** *1*.

137. Allen, M. P. T., D. J., *Computer simulation of liquids*. Oxford University Press: Oxford: 2004.

138. Phillpot, S.; Schelling, P.; Keblinski, P., Interfacial thermal conductivity: Insights from atomic level simulation. *J Mater Sci* **2005,** *40* (12), 3143-3148.

139. Cola, B. A.; Xu, J.; Fisher, T. S., Contact mechanics and thermal conductance of carbon nanotube array interfaces. *International Journal of Heat and Mass Transfer* **2009,** *52* (15–16), 3490-3503.

140. Bui, K.; Grady, B. P.; Papavassiliou, D. V., Heat transfer in high volume fraction CNT nanocomposites: Effects of inter-nanotube thermal resistance. *Chemical Physics Letters* **2011,** *508* (4–6), 248-251.

141. Maruyama, S.; Igarashi, Y.; Taniguchi, Y.; Shiomi, J., Anisotropic Heat Transfer of Single-Walled Carbon Nanotubes. *Journal of Thermal Science and Technology* **2006,** *1* (2), 138-148.

142. Varshney, V.; Patnaik, S. S.; Roy, A. K.; Farmer, B. L., Modeling of Thermal Conductance at Transverse CNT−CNT Interfaces. *The Journal of Physical Chemistry C* **2010,** *114* (39), 16223-16228.

143. Zhong, H.; Lukes, J. R., Interfacial thermal resistance between carbon nanotubes: Molecular dynamics simulations and analytical thermal modeling. *Physical Review B* **2006,** *74* (12), 125403.

144. Xu, Z.; Buehler, M. J., Nanoengineering Heat Transfer Performance at Carbon Nanotube Interfaces. *ACS Nano* **2009,** *3* (9), 2767-2775.

145. Keblinski, P.; Phillpot, S. R.; Choi, S. U. S.; Eastman, J. A., Mechanisms of heat flow in suspensions of nano-sized particles (nanofluids). *International Journal of Heat and Mass Transfer* **2002,** *45* (4), 855-863.

146. Xue, Q.-Z., Model for effective thermal conductivity of nanofluids. *Physics Letters A* **2003,** *307* (5–6), 313-317.

147. Clancy, T. C.; Gates, T. S., Modeling of interfacial modification effects on thermal conductivity of carbon nanotube composites. *Polymer* **2006,** *47* (16), 5990-5996.

148. Sirringhaus, H.; Brown, P. J.; Friend, R. H.; Nielsen, M. M.; Bechgaard, K.; Langeveld-Voss, B. M. W.; Spiering, A. J. H.; Janssen, R. A. J.; Meijer, E. W.; Herwig, P.; de Leeuw, D. M., Two-dimensional charge transport in self-organized, high-mobility conjugated polymers. *Nature* **1999,** *401* (6754), 685-688.

149. Molden, D., Water for food, Water for life: A Comprehensive Assessment of Water Management in Agriculture. *Earthscan/IWMI* **2007**.

150. Gleick, P. H., Water in Crisis: A Guide to the World's Freshwater Resources. *Oxford University Press* **1993**, 13.

151. Dickson, A. G.; Goyet, C., Handbook of methods for the analysis of the various parameters of the carbon dioxide system in sea water; version 2. *ORNL/CDIAC-74* **1994**.

152. Fritzmann, C.; Löwenberg, J.; Wintgens, T.; Melin, T., State-of-the-art of reverse osmosis desalination. *Desalination* **2007,** *216* (1–3), 1-76.

153. Davis, T. A., Porter, M.C. , Electrodialysis. *Noyes Publications, New Jersey* **1990**.

154. Pontié, M.; Derauw, J. S.; Plantier, S.; Edouard, L.; Bailly, L., Seawater desalination: nanofiltration—a substitute for reverse osmosis? *Desalination and Water Treatment* **2012,** *51* (1-3), 485-494.

155. Holt, J. K.; Park, H. G.; Wang, Y.; Stadermann, M.; Artyukhin, A. B.; Grigoropoulos, C. P.; Noy, A.; Bakajin, O., Fast Mass Transport Through Sub-2-Nanometer Carbon Nanotubes. *Science* **2006,** *312* (5776), 1034-1037.

156. Hinds, B. J.; Chopra, N.; Rantell, T.; Andrews, R.; Gavalas, V.; Bachas, L. G., Aligned Multiwalled Carbon Nanotube Membranes. *Science* **2004,** *303* (5654), 62-65.

157. Hummer, G.; Rasaiah, J. C.; Noworyta, J. P., Water conduction through the hydrophobic channel of a carbon nanotube. *Nature* **2001,** *414* (6860), 188-190.

158. Kalra, A.; Garde, S.; Hummer, G., Osmotic water transport through carbon nanotube membranes. *Proceedings of the National Academy of Sciences* **2003,** *100* (18), 10175-10180.

159. Striolo, A., The Mechanism of Water Diffusion in Narrow Carbon Nanotubes. *Nano Letters* **2006,** *6* (4), 633-639.

160. Corry, B., Designing Carbon Nanotube Membranes for Efficient Water Desalination. *The Journal of Physical Chemistry B* **2008,** *112* (5), 1427-1434.

161. Nasrabadi, A. T.; Foroutan, M., Ion-separation and water-purification using single-walled carbon nanotube electrodes. *Desalination* **2011,** *277* (1â€“3), 236-243.

162. Hughes, Z. E.; Shearer, C. J.; Shapter, J.; Gale, J. D., Simulation of Water Transport Through Functionalized Single-Walled Carbon Nanotubes (SWCNTs). *The Journal of Physical Chemistry C* **2012,** *116* (47), 24943-24953.

163. Corry, B., Water and ion transport through functionalised carbon nanotubes: implications for desalination technology. *Energy & Environmental Science* **2011,** *4* (3), 751-759.

164. Fornasiero, F.; Park, H. G.; Holt, J. K.; Stadermann, M.; Grigoropoulos, C. P.; Noy, A.; Bakajin, O., Ion exclusion by sub-2-nm carbon nanotube pores. *Proceedings of the National Academy of Sciences* **2008**.

165. Tofighy, M. A.; Shirazi, Y.; Mohammadi, T.; Pak, A., Salty water desalination using carbon nanotubes membrane. *Chemical Engineering Journal* **2011,** *168* (3), 1064-1072.

166. Suk, M. E.; Aluru, N. R., Water Transport through Ultrathin Graphene. *The Journal of Physical Chemistry Letters* **2010,** *1* (10), 1590-1594.

167. Sint, K.; Wang, B.; Král, P., Selective Ion Passage through Functionalized Graphene Nanopores. *Journal of the American Chemical Society* **2008,** *130* (49), 16448-16449.

168. Cohen-Tanugi, D.; Grossman, J. C., Water Desalination across Nanoporous Graphene. *Nano Letters* **2012,** *12* (7), 3602-3608.

169. Lu, W.; Soukiassian, P.; Boeckl, J., Graphene: Fundamentals and functionalities. *MRS Bulletin* **2012,** *37* (12), 1119-1124.

170. Ni, Z. H.; Wang, H. M.; Kasim, J.; Fan, H. M.; Yu, T.; Wu, Y. H.; Feng, Y. P.; Shen, Z. X., Graphene Thickness Determination Using Reflection and Contrast Spectroscopy. *Nano Letters* **2007,** *7* (9), 2758-2763.

171. Bird, R. B.; Stewart, W. E.; Lightfoot, E. N., Transport Phenomena. *John Wiley & sons* **1976**.

172. Merchant, C. A.; Healy, K.; Wanunu, M.; Ray, V.; Peterman, N.; Bartel, J.; Fischbein, M. D.; Venta, K.; Luo, Z.; Johnson, A. T. C.; Drndić, M., DNA Translocation through Graphene Nanopores. *Nano Letters* **2010,** *10* (8), 2915-2921.

173. Garaj, S.; Hubbard, W.; Reina, A.; Kong, J.; Branton, D.; Golovchenko, J. A., Graphene as a subnanometre trans-electrode membrane. *Nature* **2010,** *467* (7312), 190-193.

174. Schneider, G. g. F.; Kowalczyk, S. W.; Calado, V. E.; Pandraud, G. g.; Zandbergen, H. W.; Vandersypen, L. M. K.; Dekker, C., DNA Translocation through Graphene Nanopores. *Nano Letters* **2010,** *10* (8), 3163-3167.

175. Du, D.; Yang, Y.; Lin, Y., Graphene-based materials for biosensing and bioimaging. *MRS Bulletin* **2012,** *37* (12), 1290-1296.

176. Bell, D. C.; Lemme, M. C.; Stern, L. A.; Williams, J. R.; Marcus, C. M., Precision cutting and patterning of graphene with helium ions. *Nanotechnology* **2009,** *20* (45), 455301.

177. Bieri, M.; Treier, M.; Cai, J.; Ait-Mansour, K.; Ruffieux, P.; Groning, O.; Groning, P.; Kastler, M.; Rieger, R.; Feng, X.; Mullen, K.; Fasel, R., Porous graphenes: two-dimensional polymer synthesis with atomic precision. *Chemical Communications* **2009,** *0* (45), 6919-6921.

178. Kim, M.; Safron, N. S.; Han, E.; Arnold, M. S.; Gopalan, P., Fabrication and Characterization of Large-Area, Semiconducting Nanoperforated Graphene Materials. *Nano Letters* **2010,** *10* (4), 1125-1131.

179. O'Hern, S. C.; Stewart, C. A.; Boutilier, M. S. H.; Idrobo, J.-C.; Bhaviripudi, S.; Das, S. K.; Kong, J.; Laoui, T.; Atieh, M.; Karnik, R., Selective Molecular Transport through Intrinsic Defects in a Single Layer of CVD Graphene. *ACS Nano* **2012,** *6* (11), 10130-10138.

180. Konkena, B.; Vasudevan, S., Understanding Aqueous Dispersibility of Graphene Oxide and Reduced Graphene Oxide through pKa Measurements. *The Journal of Physical Chemistry Letters* **2012,** *3* (7), 867-872.

181. Choi, E.-Y.; Han, T. H.; Hong, J.; Kim, J. E.; Lee, S. H.; Kim, H. W.; Kim, S. O., Noncovalent functionalization of graphene with end-functional polymers. *Journal of Materials Chemistry* **2010,** *20* (10), 1907-1912.

182. Mishra, A. K.; Ramaprabhu, S., Functionalized graphene sheets for arsenic removal and desalination of sea water. *Desalination* **2011,** *282* (0), 39-45.

183. Sun, P.; Zhu, M.; Wang, K.; Zhong, M.; Wei, J.; Wu, D.; Xu, Z.; Zhu, H., Selective Ion Penetration of Graphene Oxide Membranes. *ACS Nano* **2012,** *7* (1), 428-437.

184. W.R. Russel; D.A. Saville; Schowalter, W. R., Colloidal Dispersions. *Cambridge University Press: Cambridge, UK* **1989**.

185. Faller, R.; Schmitz, H.; Biermann, O.; Müller-Plathe, F., Automatic parameterization of force fields for liquids by simplex optimization. *Journal of Computational Chemistry* **1999,** *20* (10), 1009-1017.

186. Chandler, D., *Introduction to Modern Statistical Mechanics*. Oxford University Press, New York: 1987.

187. Bratko, D.; Striolo, A.; Wu, J. Z.; Blanch, H. W.; Prausnitz, J. M., Orientation-Averaged Pair Potentials between Dipolar Proteins or Colloids. *The Journal of Physical Chemistry B* **2002,** *106* (10), 2714-2720.

188. Striolo, A.; Tavares, F. W.; Bratko, D.; Blanch, H. W.; Prausnitz, J. M., Analytic calculation of phase diagrams for charged dipolar colloids with orientation-averaged pair potentials. *Physical Chemistry Chemical Physics* **2003,** *5* (21), 4851-4857.

189. Tavares, F. W.; Bratko, D.; Striolo, A.; Blanch, H. W.; Prausnitz, J. M., Phase behavior of aqueous solutions containing dipolar proteins from second-order perturbation theory. *The Journal of Chemical Physics* **2004,** *120* (20), 9859-9869.

190. Striolo, A.; McCabe, C.; Cummings, P. T., Thermodynamic and Transport Properties of Polyhedral Oligomeric Sislesquioxanes in Poly(dimethylsiloxane). *The Journal of Physical Chemistry B* **2005,** *109* (30), 14300-14307.

191. Striolo, A.; McCabe, C.; Cummings, P. T., Effective Interactions between Polyhedral Oligomeric Sislesquioxanes Dissolved in Normal Hexadecane from Molecular Simulation. *Macromolecules* **2005,** *38* (21), 8950-8959.

192. Chan, E. R.; Striolo, A.; McCabe, C.; Cummings, P. T.; Glotzer, S. C., Coarse-grained force field for simulating polymer-tethered silsesquioxane self-assembly in solution. *The Journal of Chemical Physics* **2007,** *127* (11), 114102-15.

193. Plimpton, S., Fast Parallel Algorithms for Short-Range Molecular Dynamics. *Journal of Computational Physics* **1995,** *117* (1), 1-19.

194. http://lammps.sandia.gov.

195. Tersoff, J., New empirical approach for the structure and energy of covalent systems. *Physical Review B* **1988,** *37* (12), 6991-7000.

196. Tersoff, J., Empirical Interatomic Potential for Carbon, with Applications to Amorphous Carbon. *Physical Review Letters* **1988,** *61* (25), 2879-2882.

197. Tersoff, J., Modeling solid-state chemistry: Interatomic potentials for multicomponent systems. *Physical Review B* **1989,** *39* (8), 5566-5568.

198. Nath, S. K.; Escobedo, F. A.; de Pablo, J. J., On the simulation of vapor--liquid equilibria for alkanes. *The Journal of Chemical Physics* **1998,** *108* (23), 9905-9911.

199. Nath, S. K.; Khare, R., New forcefield parameters for branched hydrocarbons. *The Journal of Chemical Physics* **2001,** *115* (23), 10837-10844.

200. Alberto, S., On the solution self-assembly of nanocolloidal brushes: insights from simulations. *Nanotechnology* **2008,** *19* (44), 445606.

201. Striolo, A.; Colina, C. M.; Gubbins, K. E.; Elvassore, N.; Lue, L., The Depletion Attraction between Pairs of Colloid Particles in Polymer Solution. *Molecular Simulation* **2004,** *30* (7), 437-449.

202. Ghosh, S.; Calizo, I.; Teweldebrhan, D.; Pokatilov, E. P.; Nika, D. L.; Balandin, A. A.; Bao, W.; Miao, F.; Lau, C. N., Extremely high thermal conductivity of graphene: Prospects for thermal management applications in nanoelectronic circuits. *Applied Physics Letters* **2008,** *92* (15), 151911-3.

203. Konatham, D.; Striolo, A., Molecular Design of Stable Graphene Nanosheets Dispersions. *Nano Letters* **2008,** *8* (12), 4630-4641.

204. Jorgensen, W. L.; Maxwell, D. S.; Tirado-Rives, J., Development and Testing of the OPLS All-Atom Force Field on Conformational Energetics and Properties of Organic Liquids. *Journal of the American Chemical Society* **1996,** *118* (45), 11225-11236.

205. Shangchao, L.; Markus, J. B., The effect of non-covalent functionalization on the thermal conductance of graphene/organic interfaces. *Nanotechnology* **2013,** *24* (16), 165702.

206. Muller-Plathe, F., A simple nonequilibrium molecular dynamics method for calculating the thermal conductivity. *The Journal of Chemical Physics* **1997,** *106* (14), 6082-6085.

207. Song, S. H.; Park, K. H.; Kim, B. H.; Choi, Y. W.; Jun, G. H.; Lee, D. J.; Kong, B.-S.; Paik, K.-W.; Jeon, S., Enhanced Thermal Conductivity of Epoxy–Graphene Composites by Using Non-Oxidized Graphene Flakes with Non-Covalent Functionalization. *Advanced Materials* **2013,** *25* (5), 732-737.

208. Goyal, V.; Balandin, A. A., Thermal properties of the hybrid graphene-metal nano-micro-composites: Applications in thermal interface materials. *Applied Physics Letters* **2012,** *100* (7), -.

209. Hu, L.; Desai, T.; Keblinski, P., Thermal transport in graphene-based nanocomposite. *Journal of Applied Physics* **2011,** *110* (3), -.

210. Shahil, K. M. F.; Balandin, A. A., Thermal properties of graphene and multilayer graphene: Applications in thermal interface materials. *Solid State Communications* **2012,** *152* (15), 1331-1340.

211. Huang, X.; Zhi, C.; Jiang, P., Toward Effective Synergetic Effects from Graphene Nanoplatelets and Carbon Nanotubes on Thermal Conductivity of Ultrahigh Volume Fraction Nanocarbon Epoxy Composites. *The Journal of Physical Chemistry C* **2012,** *116* (44), 23812-23820.

212. Wang, M.; Galpaya, D.; Lai, Z. B.; Xu, Y.; Yan, C., Thermal transport in graphene-polymer nanocomposites. In *Fourth International Conference on Smart Materials and Nanotechnology in Engineering [Proceedings of SPIE, 8793]*, SPIE - Society of Photo-Optical Instrumentation Engineers: Gold Coast, Qld, 2013; pp 1-6.

213. Hu, L.; Desai, T.; Keblinski, P., Determination of interfacial thermal resistance at the nanoscale. *Physical Review B* **2011,** *83* (19), 195423.

214. Luo, T.; Lloyd, J. R., Enhancement of Thermal Energy Transport Across Graphene/Graphite and Polymer Interfaces: A Molecular Dynamics Study. *Advanced Functional Materials* **2012,** *22* (12), 2495-2502.

215. Mortazavi, B.; Benzerara, O.; Meyer, H.; Bardon, J.; Ahzi, S., Combined molecular dynamics-finite element multiscale modeling of thermal conduction in graphene epoxy nanocomposites. *Carbon* **2013,** *60* (0), 356-365.

216. Hai, M. D.; Dimitrios, V. P.; Kieran, J. M.; Shigeo, M., Computational modeling of the thermal conductivity of single-walled carbon nanotube–polymer composites. *Nanotechnology* **2008,** *19* (6), 065702.

217. Brown, J. T.; Allen, M. P.; Martín del Río, E.; Miguel, E. d., Effects of elongation on the phase behavior of the Gay-Berne fluid. *Physical Review E* **1998,** *57* (6), 6685-6699.

218. Wilson, M. R., Progress in computer simulations of liquid crystals. *International Reviews in Physical Chemistry* **2005,** *24* (3-4), 421-455.

219. Chen, Z.; Jang, W.; Bao, W.; Lau, C. N.; Dames, C., Thermal contact resistance between graphene and silicon dioxide. *Applied Physics Letters* **2009,** *95* (16), 161910-3.

220. Konatham, D.; Striolo, A., Thermal boundary resistance at the graphene-oil interface. *Applied Physics Letters* **2009,** *95* (16), 163105-3.

221. Incropera, F. P.; Dewitt, D. P.; Bergman, T. L.; Lavine, A. S., *Fundamentals of Heat and Mass Transfer*. John Wiley & Sons: 2007.

222. Calado, J. C. G.; Fareleira, J. M. N. A.; Nieto de Castro, C. A.; Wakeham, W. A., Thermal conductivity of five hydrocarbons along the saturation line. *International Journal of Thermophysics* **1983,** *4* (3), 193-208.

223. Wei, Z.; Ni, Z.; Bi, K.; Chen, M.; Chen, Y., Interfacial thermal resistance in multilayer graphene structures. *Physics Letters A* **2011,** *375* (8), 1195-1199.

224. Duong, H. M.; Papavassiliou, D. V.; Lee, L. L.; Mullen, K. J., Random walks in nanotube composites: Improved algorithms and the role of thermal boundary resistance. *Applied Physics Letters* **2005,** *87* (1), 013101-3.

225. Duong, H. M.; Papavassiliou, D. V.; Mullen, K. J.; Wardle, B. L.; Maruyama, S., A numerical study on the effective thermal conductivity of biological fluids containing single-walled carbon nanotubes. *International Journal of Heat and Mass Transfer* **2009,** *52* (23–24), 5591-5597.

226. Duong, H. M.; Papavassiliou, D. V.; Mullen, K. J.; Wardle, B. L.; Maruyama, S., Calculated Thermal Properties of Single-Walled Carbon Nanotube Suspensions. *The Journal of Physical Chemistry C* **2008,** *112* (50), 19860-19865.

227. A., E., On the movement of small particles suspended in stationary liquids required by the molecular-kinetic theory of heat. *Annalen Der Physik* **1905,** *17*, 549-560.

228. Huang, Y.; Wu, J.; Hwang, K. C., Thickness of graphene and single-wall carbon nanotubes. *Physical Review B* **2006,** *74* (24), 245413.

229. Bui, K.; Duong, H. M.; Striolo, A.; Papavassiliou, D. V., Effective Heat Transfer Properties of Graphene Sheet Nanocomposites and Comparison to Carbon Nanotube Nanocomposites. *The Journal of Physical Chemistry C* **2011,** *115* (10), 3872-3880.

230. Duncan, P. D.; Dennison, M.; Masters, A. J.; Wilson, M. R., Theory and computer simulation for the cubatic phase of cut spheres. *Physical Review E* **2009,** *79* (3), 031702.

231. Eppenga, R.; Frenkel, D., Monte Carlo study of the isotropic and nematic phases of infinitely thin hard platelets. *Molecular Physics* **1984,** *52* (6), 1303-1334.

232. Song, P.; Cao, Z.; Cai, Y.; Zhao, L.; Fang, Z.; Fu, S., Fabrication of exfoliated graphene-based polypropylene nanocomposites with enhanced mechanical and thermal properties. *Polymer* **2011,** *52* (18), 4001-4010.

233. Kappagantula, K.; Pantoya, M. L., Experimentally measured thermal transport properties of aluminum–polytetrafluoroethylene nanocomposites with graphene and carbon nanotube additives. *International Journal of Heat and Mass Transfer* **2012,** *55* (4), 817-824.

234. Kim, J.; Yim, B.-s.; Kim, J.-m.; Kim, J., The effects of functionalized graphene nanosheets on the thermal and mechanical properties of epoxy composites for anisotropic conductive adhesives (ACAs). *Microelectronics Reliability* **2012,** *52* (3), 595-602.

235. Shahil, K. M. F.; Balandin, A. A., Graphene–Multilayer Graphene Nanocomposites as Highly Efficient Thermal Interface Materials. *Nano Letters* **2012,** *12* (2), 861-867.

236. Pu, X.; Zhang, H.-B.; Li, X.; Gui, C.; Yu, Z.-Z., Thermally conductive and electrically insulating epoxy nanocomposites with silica-coated graphene. *RSC Advances* **2014,** *4* (29), 15297-15303.

237. Li, Q.; Guo, Y.; Li, W.; Qiu, S.; Zhu, C.; Wei, X.; Chen, M.; Liu, C.; Liao, S.; Gong, Y.; Mishra, A. K.; Liu, L., Ultrahigh Thermal Conductivity of Assembled Aligned Multilayer Graphene/Epoxy Composite. *Chemistry of Materials* **2014,** *26* (15), 4459-4465.

238. Ma, W.-S.; Li, J.; Zhao, X.-S., Improving the thermal and mechanical properties of silicone polymer by incorporating functionalized graphene oxide. *J Mater Sci* **2013,** *48* (15), 5287-5294.

239. Ma, W.-S.; Wu, L.; Yang, F.; Wang, S.-F., Non-covalently modified reduced graphene oxide/polyurethane nanocomposites with good mechanical and thermal properties. *J Mater Sci* **2014,** *49* (2), 562-571.

240. Yavari, F.; Fard, H. R.; Pashayi, K.; Rafiee, M. A.; Zamiri, A.; Yu, Z.; Ozisik, R.; Borca-Tasciuc, T.; Koratkar, N., Enhanced Thermal Conductivity in a Nanostructured Phase Change Composite due to Low Concentration Graphene Additives. *The Journal of Physical Chemistry C* **2011,** *115* (17), 8753-8758.

241. Baby, T. T.; Sundara, R., Synthesis and Transport Properties of Metal Oxide Decorated Graphene Dispersed Nanofluids. *The Journal of Physical Chemistry C* **2011,** *115* (17), 8527-8533.

242. Jinhong, Y.; Xingyi, H.; Chao, W.; Pingkai, J., Permittivity, thermal conductivity and thermal stability of poly(vinylidene fluoride)/graphene nanocomposites. *Dielectrics and Electrical Insulation, IEEE Transactions on* **2011,** *18* (2), 478-484.

243. Jiang, X.; Drzal, L. T., Multifunctional high-density polyethylene nanocomposites produced by incorporation of exfoliated graphene nanoplatelets 2: Crystallization, thermal and electrical properties. *Polymer Composites* **2012,** *33* (4), 636-642.

244. Tseng, I. H.; Chang, J.-C.; Huang, S.-L.; Tsai, M.-H., Enhanced thermal conductivity and dimensional stability of flexible polyimide nanocomposite film by addition of functionalized graphene oxide. *Polymer International* **2013,** *62* (5), 827-835.

245. Koo, M.; Bae, J.-S.; Shim, S.; Kim, D.; Nam, D.-G.; Lee, J.-W.; Lee, G.-W.; Yeum, J.; Oh, W., Thermo-dependent characteristics of polyimide–graphene composites. *Colloid Polym Sci* **2011,** *289* (13), 1503-1509.

246. Fan, L.-W.; Fang, X.; Wang, X.; Zeng, Y.; Xiao, Y.-Q.; Yu, Z.-T.; Xu, X.; Hu, Y.-C.; Cen, K.-F., Effects of various carbon nanofillers on the thermal conductivity and energy storage properties of paraffin-based nanocomposite phase change materials. *Applied Energy* **2013,** *110* (0), 163-172.

247. Warzoha, R. J.; Fleischer, A. S., Effect of Graphene Layer Thickness and Mechanical Compliance on Interfacial Heat Flow and Thermal Conduction in Solid–Liquid Phase Change Materials. *ACS Applied Materials & Interfaces* **2014,** *6* (15), 12868-12876.

248. Abad, B.; Alda, I.; Diaz-Chao, P.; Kawakami, H.; Almarza, A.; Amantia, D.; Gutierrez, D.; Aubouy, L.; Martin-Gonzalez, M., Improved power factor of polyaniline nanocomposites with exfoliated graphene nanoplatelets (GNPs). *Journal of Materials Chemistry A* **2013,** *1* (35), 10450-10457.

249. Xiong, X.; Wang, J.; Jia, H.; Fang, E.; Ding, L., Structure, thermal conductivity, and thermal stability of bromobutyl rubber nanocomposites with ionic liquid modified graphene oxide. *Polymer Degradation and Stability* **2013,** *98* (11), 2208-2214.

250. Heo, C.; Chang, J.-H., Polyimide nanocomposites based on functionalized graphene sheets: Morphologies, thermal properties, and electrical and thermal conductivities. *Solid State Sciences* **2013,** *24* (0), 6-14.

251. Li, T.; Lee, J.-H.; Wang, R.; Kang, Y. T., Heat transfer characteristics of phase change nanocomposite materials for thermal energy storage application. *International Journal of Heat and Mass Transfer* **2014,** *75* (0), 1-11.

252. Wang, W.; Wang, C.; Wang, T.; Li, W.; Chen, L.; Zou, R.; Zheng, J.; Li, X., Enhancing the thermal conductivity of n-eicosane/silica phase change materials by reduced graphene oxide. *Materials Chemistry and Physics* **2014,** *147* (3), 701-706.

253. Alaghemandi, M.; Gharib-Zahedi, M. R.; Spohr, E.; Böhm, M. C., Thermal Conductivity of Polyamide-6,6 in the Vicinity of Charged and Uncharged Graphene Layers: A Molecular Dynamics Analysis. *The Journal of Physical Chemistry C* **2012,** *116* (26), 14115-14122.

254. Eslami, H.; Mohammadzadeh, L.; Mehdipour, N., Anisotropic heat transport in nanoconfined polyamide-6,6 oligomers: Atomistic reverse nonequilibrium molecular dynamics simulation. *The Journal of Chemical Physics* **2012,** *136* (10), -.

255. Cheng, A.; Steele, W. A., Computer simulation of ammonia on graphite. I. Low temperature structure of monolayer and bilayer films. *The Journal of Chemical Physics* **1990,** *92* (6), 3858-3866.

256. Berendsen, H. J. C.; Grigera, J. R.; Straatsma, T. P., The missing term in effective pair potentials. *The Journal of Physical Chemistry* **1987,** *91* (24), 6269-6271.

257. Palmer, B. J.; Pfund, D. M.; Fulton, J. L., Direct Modeling of EXAFS Spectra from Molecular Dynamics Simulations. *The Journal of Physical Chemistry* **1996,** *100* (32), 13393-13398.

258. Wernersson, E.; Jungwirth, P., Effect of Water Polarizability on the Properties of Solutions of Polyvalent Ions: Simulations of Aqueous Sodium Sulfate with Different Force Fields. *Journal of Chemical Theory and Computation* **2010,** *6* (10), 3233-3240.

259. Ho, T. A.; Striolo, A., Polarizability effects in molecular dynamics simulations of the graphene-water interface. *The Journal of Chemical Physics* **2013,** *138* (5), 054117-9.

260. Miyamoto, S.; Kollman, P. A., Settle: An analytical version of the SHAKE and RATTLE algorithm for rigid water models. *Journal of Computational Chemistry* **1992,** *13* (8), 952-962.

261. Lee, S. H.; Rasaiah, J. C., Molecular Dynamics Simulation of Ion Mobility. 2. Alkali Metal and Halide Ions Using the SPC/E Model for Water at 25 Â°Câ€ *The Journal of Physical Chemistry* **1996,** *100* (4), 1420-1425.

262. Jones, J. E., On the Determination of Molecular Fields. II. From the Equation of State of a Gas. *Proceedings of the Royal Society of London. Series A* **1924,** *106* (738), 463-477.

263. Hess, B.; Kutzner, C.; van der Spoel, D.; Lindahl, E., GROMACS 4: Algorithms for Highly Efficient, Load-Balanced, and Scalable Molecular Simulation. *Journal of Chemical Theory and Computation* **2008,** *4* (3), 435-447.

264. Berendsen, H. J. C.; van der Spoel, D.; van Drunen, R., GROMACS: A message-passing parallel molecular dynamics implementation. *Computer Physics Communications* **1995,** *91* (1–3), 43-56.

265. Lindahl, E.; Hess, B.; van der Spoel, D., GROMACS 3.0: a package for molecular simulation and trajectory analysis. *Journal of Molecular Modeling* **2001,** *7* (8), 306-317.

266. Van Der Spoel, D.; Lindahl, E.; Hess, B.; Groenhof, G.; Mark, A. E.; Berendsen, H. J. C., GROMACS: Fast, flexible, and free. *Journal of Computational Chemistry* **2005,** *26* (16), 1701-1718.

267. Roux, B., The calculation of the potential of mean force using computer simulations. *Computer Physics Communications* **1995,** *91* (1–3), 275-282.

268. Souaille, M.; Roux, B. t., Extension to the weighted histogram analysis method: combining umbrella sampling with free energy calculations. *Computer Physics Communications* **2001,** *135* (1), 40-57.

269. Kumar, S.; Rosenberg, J. M.; Bouzida, D.; Swendsen, R. H.; Kollman, P. A., THE weighted histogram analysis method for free-energy calculations on biomolecules. I. The method. *Journal of Computational Chemistry* **1992,** *13* (8), 1011-1021.

270. Kumar, S.; Payne, P. W.; Vásquez, M., Method for free-energy calculations using iterative techniques. *Journal of Computational Chemistry* **1996,** *17* (10), 1269-1275.

271. Dubbeldam, D.; Beerdsen, E.; Vlugt, T. J. H.; Smit, B., Molecular simulation of loading-dependent diffusion in nanoporous materials using extended dynamically corrected transition state theory. *The Journal of Chemical Physics* **2005,** *122* (22), 224712-17.

272. Lv, W., The adsorption of DNA bases on neutral and charged (8, 8) carbon-nanotubes. *Chemical Physics Letters* **2011,** *514* (4–6), 311-316.

273. Patel, A. J.; Varilly, P.; Jamadagni, S. N.; Acharya, H.; Garde, S.; Chandler, D., Extended surfaces modulate hydrophobic interactions of neighboring solutes. *Proceedings of the National Academy of Sciences* **2011,** *108* (43), 17678-17683.

274. Rajamani, S.; Truskett, T. M.; Garde, S., Hydrophobic hydration from small to large lengthscales: Understanding and manipulating the crossover. *Proceedings of the National Academy of Sciences of the United States of America* **2005,** *102* (27), 9475-9480.

275. Lv, W.; Wu, R. a., The interfacial-organized monolayer water film (MWF) induced "two-step" aggregation of nanographene: both in stacking and sliding assembly pathways. *Nanoscale* **2013,** *5* (7), 2765-2775.

276. Smith, D. E.; Dang, L. X., Computer simulations of NaCl association in polarizable water. *The Journal of Chemical Physics* **1994,** *100* (5), 3757-3766.

277. Zhu, F.; Schulten, K., Water and Proton Conduction through Carbon Nanotubes as Models for Biological Channels. *Biophysical Journal* **2003,** *85* (1), 236-244.

278. Liu, Y.; Huang, J.; Yang, B.; Sumpter, B. G.; Qiao, R., Duality of the interfacial thermal conductance in graphene-based nanocomposites. *Carbon* **2014,** *75* (0), 169-177.

279. Ding, P.; Su, S.; Song, N.; Tang, S.; Liu, Y.; Shi, L., Influence on thermal conductivity of polyamide-6 covalently-grafted graphene nanocomposites: varied grafting-structures by controllable macromolecular length. *RSC Advances* **2014,** *4* (36), 18782-18791.

280. Choi, J.-Y.; Kim, S. W.; Cho, K. Y., Improved thermal conductivity of graphene encapsulated poly(methyl methacrylate) nanocomposite adhesives with low loading amount of graphene. *Composites Science and Technology* **2014,** *94* (0), 147-154.

281. Tsai, M.-H.; Tseng, I. H.; Chiang, J.-C.; Li, J.-J., Flexible Polyimide Films Hybrid with Functionalized Boron Nitride and Graphene Oxide Simultaneously To Improve Thermal Conduction and Dimensional Stability. *ACS Applied Materials & Interfaces* **2014,** *6* (11), 8639-8645.

282. Inuwa, I. M.; Hassan, A.; Wang, D.-Y.; Samsudin, S. A.; Mohamad Haafiz, M. K.; Wong, S. L.; Jawaid, M., Influence of exfoliated graphite nanoplatelets on the flammability and thermal properties of polyethylene terephthalate/polypropylene nanocomposites. *Polymer Degradation and Stability* **2014,** *110* (0), 137-148.

283. Huang, H.; Ying, Y.; Peng, X., Graphene oxide nanosheet: an emerging star material for novel separation membranes. *Journal of Materials Chemistry A* **2014,** *2* (34), 13772-13782.

284. Choi, W.; Choi, J.; Bang, J.; Lee, J.-H., Layer-by-Layer Assembly of Graphene Oxide Nanosheets on Polyamide Membranes for Durable Reverse-Osmosis Applications. *ACS Applied Materials & Interfaces* **2013,** *5* (23), 12510-12519.

285. Cohen-Tanugi, D.; Grossman, J. C., Water permeability of nanoporous graphene at realistic pressures for reverse osmosis desalination. *The Journal of Chemical Physics* **2014,** *141* (7), -.

286. Gahlot, S.; Sharma, P. P.; Gupta, H.; Kulshrestha, V.; Jha, P. K., Preparation of graphene oxide nano-composite ion-exchange membranes for desalination application. *RSC Advances* **2014,** *4* (47), 24662-24670.

287. Gai, J.-G.; Gong, X.-L.; Wang, W.-W.; Zhang, X.; Kang, W.-L., An ultrafast water transport forward osmosis membrane: porous graphene. *Journal of Materials Chemistry A* **2014,** *2* (11), 4023-4028.

288. Liu, Y.; Chen, X., Mechanical properties of nanoporous graphene membrane. *Journal of Applied Physics* **2014,** *115* (3), -.

289. Nicolai, A.; Sumpter, B. G.; Meunier, V., Tunable water desalination across graphene oxide framework membranes. *Physical Chemistry Chemical Physics* **2014,** *16* (18), 8646-8654.

290. O'Hern, S. C.; Boutilier, M. S. H.; Idrobo, J.-C.; Song, Y.; Kong, J.; Laoui, T.; Atieh, M.; Karnik, R., Selective Ionic Transport through Tunable Subnanometer Pores in Single-Layer Graphene Membranes. *Nano Letters* **2014,** *14* (3), 1234-1241.

10 Appendix

10.1 Umbrella Sampling Simulations

Umbrella sampling technique uses a constraining potential, usually a harmonic potential, to constrain the system along dimension of interest, especially around the high energy barrier. Constraining potential allows enhanced sampling along the dimension of interest and specifically around the region of high energy barrier. Number of such biased sampling windows is obtained from multiple simulations. In each simulation the molecule of interest (in this study the ion) is constrained at a particular position, and this position is changed from simulation to simulation to sample all phase space. The resulting biased probability density function is solved self-consistently using WHAM analysis method for free energy and unbiased probability density function. The results shown here are calculated from 40 simulations of 4 ns each resulting in total simulation time of 160 ns. In each simulation the ion (Na^+ or Cl^-) has been constrained at different distance from the GS membrane using a harmonic potential. Value of spring constant employed to constrain the ion in different simulations was 3.4 kcal/(mol $Å^2$).

In this method a small biasing potential is added to the total potential energy function.

$$V^*(\bar{r}) = V(\bar{r}) + U^*(\xi) \qquad (7.1)$$

where $V(\bar{r})$ is the total potential energy function and $V^*(\bar{r})$ is the modified potential energy function. $U^*(\xi)$ is constraining potential usually a harmonic potential. ξ is the dimension along which we are interested in finding the free energy profile.

$$U^*(\xi) = \frac{1}{2}k(\xi - \xi_i) \tag{7.2}$$

where *k* is the force constant, and ξ_i is changed in every simulation to cover the region of phase space we are interested in.

With the biasing potential the biased probability distribution is given by

$$\rho^*(\xi) = \frac{\exp(-\beta V^*)}{\int \exp(-\beta V^*) d\bar{r}^N} \tag{7.3}$$

and the unbiased probability distribution is given by

$$\rho(\xi) = \frac{\exp(-\beta V)}{\int \exp(-\beta V) d\bar{r}^N} \tag{7.4}$$

We can extract unbiased distribution from the biased probability distribution using

$$\rho(\xi) = \rho^*(\xi)\exp(\beta U)\frac{1}{\langle \exp(\beta U)\rangle^*} \tag{7.5}$$

However, the ensemble average appearing in the denominator is not easy to obtain.

The free energies and the unbiased probability distribution functions can be extracted from the simulations using the WHAM method. WHAM method involves solving the

equations for unbiased distribution functions and free energies consistently. The equations are described below.

$$\rho(\xi) = \frac{\sum_{i}^{N_{Sim}} n_i}{\sum_{i}^{N_{Sim}} n \exp\left[-\beta\left(F_i - U_i^*(\xi)\right)\right]} \tag{7.6}$$

$$F_i = -kT\left\{\sum_{bins} \rho(\xi)\exp\left[-\beta U_i^*(\xi)\right]\right\} \tag{7.7}$$

where n_i is the number of occurrences in that particular region in the i^{th} simulation, n is the total number of bins in each histogram. Solving the above two equations iteratively gives the free energy profile and unbiased probability distribution function for the system.

10.2 Additional Simulation Details

10.2.1 Selection of Timestep

In MD simulations, the timestep used should be smaller than the fastest vibrational frequency of the system. Since the typical frequencies of molecular vibrations range from less than 10^{12} to approximately 10^{14} Hz, timesteps in the order of 1 femtosecond (fs) are typically chosen in MD simulations. For equilibrium MD simulations in Chapters 2 and 5, a timestep of 1 fs was used. A timestep of 0.005 fs was used in NEMD simulations reported in Chapters 3 and 4.

10.2.2 Selection of Number of Processors

To optimize the number of processors used to run each simulation, a test simulation run was initially performed using variable number of processors ranging from 4 to 100 for 10,000 timesteps. Then by looking at the time required to complete 10,000 timesteps as a function of number of processors used, the optimum number of processors is chosen. An example of one such simulation from Chapter 6 is provided below.

System description: The system consists of a graphene membrane surrounded by 20 Å of SPC/E water on both sides with Na^+ and Cl^- randomly placed only on one side to both neutralize the system and yield a net concentration of 0.25M. The modeled graphene has a chemically modified pore in its center with an effective diameter of ~10 Å. The carbon atoms of the graphene were modeled as LJ spheres and are kept rigid during the simulation. The rim of the pore is functionalized with 6 amine (NH_3^+) cations using the OPLS all atom force field.

Simulation details: The simulation was carried out at 300K in the NVT ensemble with a timestep of 1 fs. The system consists of 15000 atoms.

Performance Analysis: In the graph below we report the GFLOPS (Giga Floating-point Operations Per Second) to complete 10,000 timesteps as a function of number of processing cores. From the figure, we can see that 32 cores provides the optimal performance.

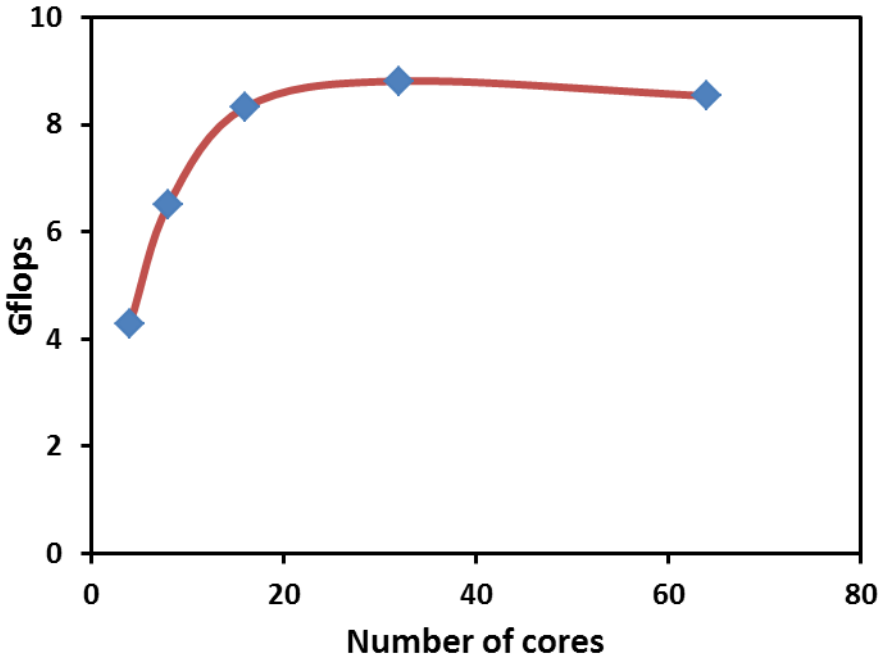
10
8
6
4
2
0
Gflops
0
20
40
60
80
Number of cores